

AD-A047 504

GENERAL ELECTRIC CORPORATE RESEARCH AND DEVELOPMENT --ETC F/G 11/2
INVESTIGATION OF CERAMICS FOR HIGH TEMPERATURE TURBINE COMPONENT--ETC(U)
JUN 77 C A JOHNSON, S PROCHAZKA N62269-76-C-0243

UNCLASSIFIED

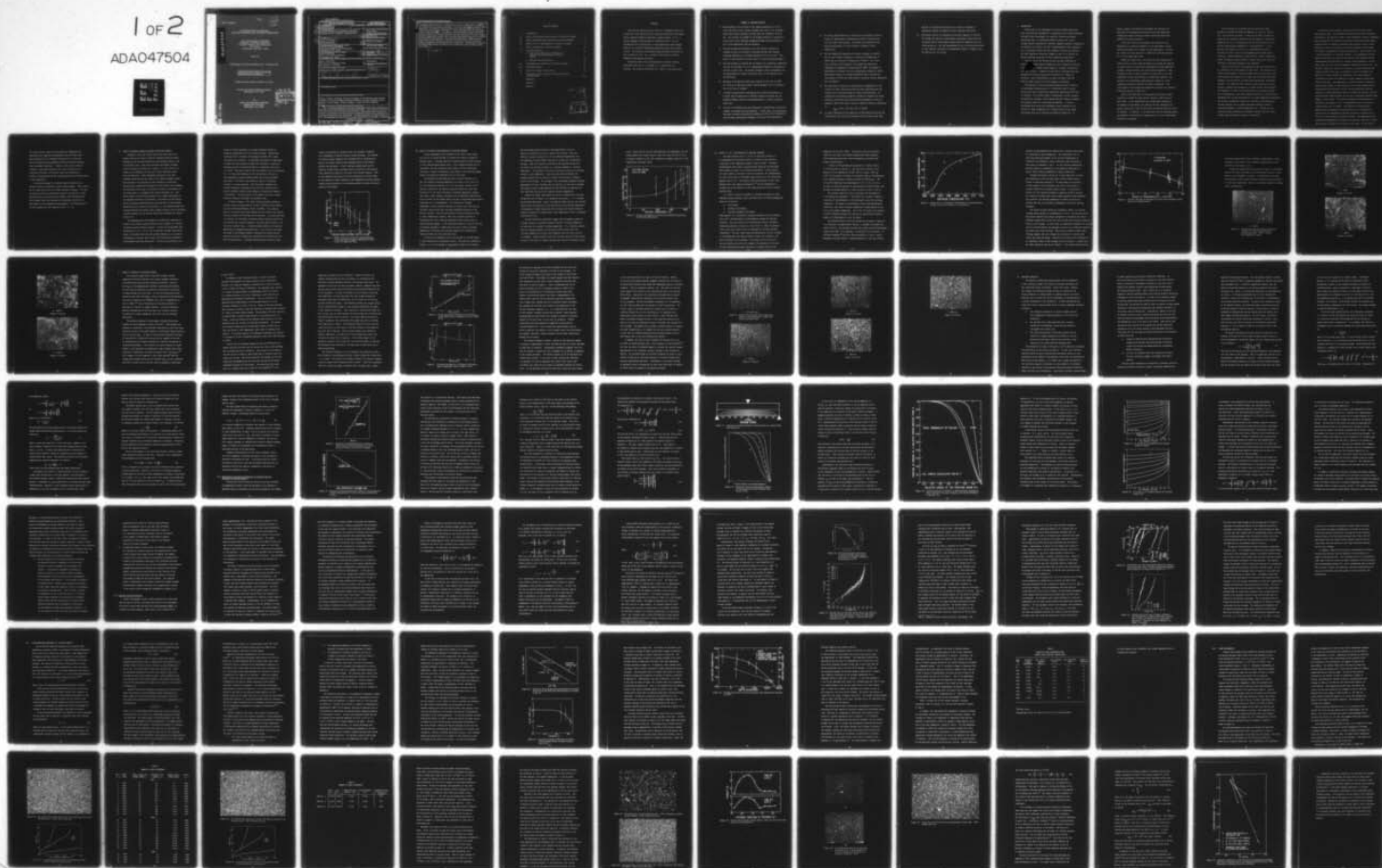
SRD-77-145

NADC-75228-30

NL

1 OF 2

ADAO47504



NADC-75228-30

AD A047504

INVESTIGATION OF CERAMICS
FOR HIGH TEMPERATURE TURBINE COMPONENTS

C. A. Johnson and S. Prochazka
GENERAL ELECTRIC COMPANY
Corporate Research and Development
P.O. Box 8
Schenectady, New York 12301

June 1977

Final Report for Period 25 March 1976 - 25 March 1977

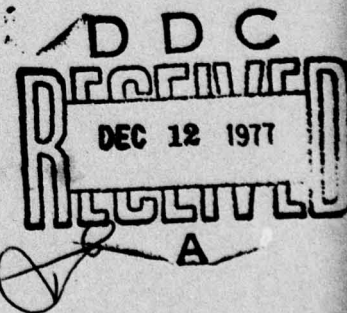
APPROVED FOR PUBLIC RELEASE
DISTRIBUTION UNLIMITED

Prepared under Contract N62269-76-C-0243

NAVAL AIR DEVELOPMENT CENTER
Warminster, PA 18974

for

NAVAL AIR SYSTEMS COMMAND
Department of the Navy
Washington, DC 20361



AD NO. _____
DDC FILE COPY

SRD-77-145

UNCLASSIFIED

SECURITY CLASSIFICATION OF THIS PAGE (When Data Entered)

19 REPORT DOCUMENTATION PAGE		READ INSTRUCTIONS BEFORE COMPLETING FORM
1. REPORT NUMBER NADC-75228-30	2. GOVT ACCESSION NO.	3. RECIPIENT'S CATALOG NUMBER
4. TITLE (and Subtitle) INVESTIGATION OF CERAMICS FOR HIGH TEMPERATURE TURBINE COMPONENTS		5. TYPE OF REPORT & PERIOD COVERED Final Report - 76 Mar 25 to 77 Mar 25
7. AUTHOR(s) Curtis A./Johnson Svante/Prochazka		6. PERFORMING ORG. REPORT NUMBER SRD-77-145
9. PERFORMING ORGANIZATION NAME AND ADDRESS General Electric Company Corporate Research and Development Schenectady, NY 12301		8. CONTRACT OR GRANT NUMBER(s) N62269-76-C-0243
11. CONTROLLING OFFICE NAME AND ADDRESS Dept. of the Navy Naval Air Systems Command Washington, DC 20361		10. PROGRAM ELEMENT, PROJECT, TASK AREA & WORK UNIT NUMBERS A03V3200/001B/6F54592201
14. MONITORING AGENCY NAME & ADDRESS (if different from Controlling Office) Dept. of the Navy Naval Air Development Center Warminster, PA 18974		12. REPORT DATE June 1977
		13. NUMBER OF PAGES F54592
		15. SECURITY CLASS. (of this report) Unclassified 62761N
		15a. DECLASSIFICATION/DOWNGRADING SCHEDULE
16. DISTRIBUTION STATEMENT (of this Report) Approved for Public Release; Distribution Unlimited 9 Final rept. 25 Mar 76 - 25 Mar 77		
17. DISTRIBUTION STATEMENT (of the abstract entered in Block 20, if different from Report) 12 126p. 12 WF54592201		
18. SUPPLEMENTARY NOTES		
19. KEY WORDS (Continue on reverse side if necessary and identify by block number) silicon carbide, sintering, fracture strength, crack blunting, grain growth, oxidation, fracture statistics, Weibull statistics, fracture origins, stress rupture, statis fatigue, dynamic fatigue, creep, fracture toughness		
20. ABSTRACT (Continue on reverse side if necessary and identify by block number) The mechanical properties of boron-doped sintered SiC were studied as a function of several fabrication and testing variables. The reduction in severity of surface defects due to the dissociation of SiC at high temperatures was characterized as a function of furnace pressure during sintering and as a function of refiring temperature after machining. The β to α polytype transformation and the accompanying grain growth were found to decrease the strength a maximum (Continued on back) ALPHA		

of approximately 25 percent. Oxidation for times to 2000 hours at 1500°C in air resulted in no net loss of strength. The time-temperature-strength interdependence was studied at temperatures from 1200 to 2100°C and times to failure from one second to five hours. The creep behavior was also studied in the vicinity of 2100°C. A method was demonstrated to derive statistical quantities such as the Weibull modulus from the positions of fracture origins, and two examples of fracture data were discussed which illustrate the effects of bimodal flaw distributions. Hot pressing experiments suggest that the large cavities often observed in sintered microstructures are caused by bridging of agglomerates during powder compaction. Preliminary studies of increasing K_{IO} through the addition of second phase particles has not been successful.

K 508 1C

TABLE OF CONTENTS

I	Introduction	1
II	Effect of Sintering Furnace Pressure on Fracture Strength. . . .	6
III	Effect of Refiring after Machining on Fracture Strength.	9
IV	Effect of β to α Transformation on Fracture Strength	12
V	Effect of Oxidation on Fracture Strength	20
VI	Fracture Statistics.	29
	A. Derivation of Statistical Parameters of Fracture from the Locations of Fracture Origins	35
	B. Multiple Flaw Distribution	48
VII	Time-Temperature Dependence of Fracture Strength	61
VIII	Creep Measurements	73
IX	Origin of Strength Limiting Flaws.	88
X	Increasing Fracture Toughness Through the Addition of Second Phases	100
	References	
	Appendix A	
	Appendix B	

ACCESSION No.	
NTIS	Whole Section <input checked="" type="checkbox"/>
DOC	Full Section <input type="checkbox"/>
UNCLASSIFIED	<input type="checkbox"/>
IDENTIFICATION	
BY	
DISTRIBUTION/AVAILABILITY CODES	
Dist.	AVAIL. and/or SPECIAL
A	

FOREWORD

This work was sponsored by the Naval Air Development Center and carried out in the General Electric Corporate Research and Development Center, Physical Chemistry Laboratory, Ceramics Branch - Dr. R. J. Charles, Manager, under Contract No. N62269-76-C-0243. It is a continuation of an investigation in high temperature, high strength ceramics for structural engineering application which was initiated in 1971. This portion was performed during the period from March 25, 1976 to March 25, 1977. Mr. I. Machlin of the Naval Air Systems Command was the program consultant.

The authors would like to acknowledge the valuable technical discussions with Drs. R. A. Giddings, R. J. Charles and G. G. Trantina. The technical assistance of C. Bobik is also appreciated.

SUMMARY OF IMPORTANT RESULTS

- 1) Bend specimens of SiC sintered at low furnace pressures (0.3 to 0.4 torr) were found to have average strengths which were 25 to 30 percent higher than similar specimens sintered under one atmosphere of inert gas. The increase in strength at low furnace pressures is believed to result from a crack "blunting" mechanism through the dissociation of SiC at high temperatures and low pressures.
- 2) Sintered and machined specimens of SiC were found to increase in strength as much as 20 percent by refiring them near the original sintering temperature at a furnace pressure of 0.3 to 0.4 torr. This effect is also believed to be the result of a crack blunting mechanism.
- 3) The bend strength of sintered SiC was found to be a relatively insensitive function of the degree of β to α transformation despite an accompanying increase in grain size. The average strength of fully transformed α -SiC was approximately 25 percent lower than that of a fine-grained β -SiC microstructure.
- 4) Specimens of sintered SiC which were oxidized in still air at 1500°C for times up to 2000 hours showed a nearly parabolic rate of oxidation and no net loss of strength.
- 5) A method of quantitatively determining the statistical parameters of fracture from the positions of fracture origins was derived for two-parameter Weibull statistics and demonstrated on a series of abraded glass rods.
- 6) Two sets of literature data were reanalyzed to quantitatively illustrate examples of multiple flaw distributions. In both cases, the observations were more accurately described by assuming two active flaw distributions than the more conventional assumption of only one flaw distribution.

- 7) The stress rupture behavior of sintered SiC was studied in biaxial tension at temperatures of approximately 2100°C by pressurizing slip cast tubes with nitrogen. The results were correlated with previous measurements of stress rupture in bending at lower temperatures.
- 8) The time-temperature dependence of fracture strength in sintered SiC was also studied in bending as a function of temperature to 1600°C and as a function of loading rate at 1600°C. At a total time to failure of five minutes, the strength was found to be independent of temperature to approximately 1200°C and dropped to approximately 85 percent of the room temperature strength by 1600°C. Quantitative analysis of strength degradation due to subcritical crack growth at 1600°C was complicated by concurrent surface degradation due to oxidation.
- 9) The creep rate of sintered SiC was measured at temperatures in the vicinity of 2100°C using the pressurized tubes mentioned above and resulted in an activation energy for creep of 246 Kcal/mole. By assuming that the primary mechanism of material transport was volume diffusion, these data along with previous measurements of creep in bending at 1600°C were used to derive an apparent diffusion coefficient of:
- $$D_{app} = 3.25 \times 10^{10} \exp [-(225 \pm 29)/RT]$$
- 10) A careful comparison of the properties of boron-doped hot-pressed and sintered SiC's has led to the conclusion that the large voids often

observed in sintered microstructures are caused by bridging of agglomerates during the compaction step of specimen fabrication.

- 11) Preliminary studies of increasing the fracture toughness of sintered SiC through the addition of particulate second phase dispersions have identified several second phase systems which are compatible with the sintering process. The only measurements of K_{IC} on two phased materials to date, however, revealed no distinguishable change in toughness with the addition of 5 w/o of B_4C .

I. INTRODUCTION

Major steps in the improvement of the gas turbine engine have been associated with advancements in superalloys and cooling technology. Although further improvements are expected, definite performance limitations exist in traditional metallic systems, and a breakthrough requires substantially increased component operating temperatures. The potential of ceramics for such a breakthrough has been recognized and a considerable effort has been launched to develop and evaluate new high temperature structural ceramics as well as to develop the design technology necessary for their engineering application.

Silicon carbide and silicon nitride have been identified as promising candidates based on properties such as oxidation stability, creep resistance, thermal shock properties, strength, availability and other criteria. A number of consolidation techniques have been developed for SiC and Si_3N_4 and have resulted in a variety of materials. Such diversification is highly desirable since one material cannot satisfy all of the emerging requirements.

The objective of this continuing program has been to develop the performance characteristics of a fabricable form of silicon carbide such that an operational temperature approaching 3000°F may be realized. The critical aspects of performance include strength, variability of strength, stress rupture behavior, fracture toughness and chemical stability in oxidizing environments. It must be anticipated that the precise performance levels required of the material in these categories are a strong function of the design innovations that can be achieved for nonductile materials. In

general, however, the materials development must maintain the objectives of developing and maintaining very high temperature strength and surface integrity without sacrificing fabrication capability or creep resistance.

In the first year of this program, the system SiC-B was identified as a promising candidate for the development of good oxidation resistance and strength at high temperatures. The work was carried out under Contract No. N00019-71-C-0290 and discussed in detail in report SRD-72-035.

During the second year it was shown that the elimination of either silicon or silica from hot-pressed SiC through the addition of carbon resulted in significant improvements of high temperature strength, creep resistance, and stress rupture properties. Bend strengths of about 75 kpsi at 1550°C and creep rates at the same temperature of less than 10^{-9} /sec at 25 kpsi were achieved. The potential of a boron-doped single phase SiC ceramic as a high temperature structural material was firmly established. This second period of the program was supported by Contract No. N00019-72-C-0129 and reported in SRD-72-171.

Work in the third year of the program was carried out under Contract No. N62269-73-C-0356 and was reported in SRD-74-040 of April 1974. It was demonstrated that conventional sintering of SiC powders to high density was possible and that mechanical properties identical to those of the earlier hot-pressed materials could be obtained. In addition, it was shown that the new sintering process was amenable to fabrication of complex parts by several conventional fabrication techniques.

The work during the following year was carried out under Contract No. N62269-74-C-0255 and summarized in report No. SRD-74-123. The objectives included: a study of the effect of additives, impurities and sintering conditions; the development of fabrication capability of SiC on a laboratory scale; and the evaluation of the physical and mechanical properties of the improved SiC. A more detailed investigation of the β to α transformation in SiC was necessary to obtain control over exaggerated grain growth during sintering. Thermal expansion, elastic modulus, thermal conductivity, modulus of rupture, Weibull modulus, fracture energy and creep were evaluated on specimens prepared in the laboratory.

During the fifth year, the program was supported under Contract No. N62269-75-C-0122 and reported in SRD-75-126. Work carried out included the development of improved powder processing techniques where the SiC powder was dispersed in a liquid such as benzene and passed through a very fine screen to remove large agglomerates and foreign material. The liquid was then removed by spray freezing and freeze drying to minimize the segregation of soluble binders and lubricants. The dependence of density and microstructure on sintering variables such as temperature, time, green density, particle size and sintering atmosphere were studied quantitatively in a high temperature dilatometer. The fracture strength was studied as a function of fabrication and testing variables such as powder processing technique, density, sintering atmosphere, testing temperature, etc. Testing was also carried out under conditions of thermally induced stresses to study thermal shock and thermal fatigue of sintered SiC.

During the present contract, efforts have been directed toward three general areas: the continued characterization of those properties necessary for the effective design of high temperature structural components from sintered SiC; the evaluation and control of microstructural inhomogeneities which are commonly associated with fracture; and the initial feasibility study of increasing the fracture toughness of SiC through the addition of appropriate second phase particles. Since sintered SiC is being developed as a structural material, it is appropriate that all three of these areas of study are concerned with the characterization, understanding and optimization of strength related properties. Of the three areas, the first has been emphasized during the previous year. The fracture strength was studied as a function of several fabrication and testing variables which must be optimized to assure the highest probability of success and must be sufficiently well characterized to satisfactorily predict the behavior of a given component design under service conditions. The improvement in strength caused by blunting of surface flaws through the dissociation of SiC at high temperatures was characterized both during the initial sintering operation where the severity of surface fabrication defects is reduced and during a refiring operation after machining where the severity of machining induced surface damage is also reduced. The fracture strength was characterized as a function of the degree of β to α transformation and as a function of exposure time in air at 1500°C. The statistics of fracture were approached by developing and verifying the tools to satisfactorily describe the size dependence of fracture strength in sintered SiC as well as in other potential structural ceramics. The temperature-time-strength interdependence was studied in sintered SiC from 1200 to 2100°C and at times to failure of one second to five hours. In the area of

the evaluation and control of microstructural inhomogeneities, experiments have supported the hypothesis that the large voids which commonly serve as strength limiting flaws are caused by massive bridging of weak agglomerates during the powder pressing step of specimen fabrication. Finally, in the area of fracture toughness, second phase particles have been incorporated into sinterable SiC powder, the mixtures have been hot-pressed or sintered to high density and the resulting materials have been tested at room temperature.

A concurrent program is oriented toward the synthesis and characterization of sinterable silicon carbide powders. These results are not reported here but will become available elsewhere. In order to maintain continuity with previous reports, the majority of work reported below was carried out with powders from Pittsburgh Plate Glass Company which were prepared by a proprietary process from chlorinated silicon compounds and hydrocarbons. The characteristics of these powders have been reported in Ref. 1, p. 62.

II. EFFECT OF SINTERING FURNACE PRESSURE ON FRACTURE STRENGTH

Included in last year's final report² were the results of a limited study of the effect of furnace atmosphere pressure during sintering on the fracture strength of bend specimens tested in the "as-sintered" state. These data indicated that higher strengths could be obtained by sintering in vacuum (.2-.4 torr) than by sintering in one atmosphere of inert gas, despite equivalent grain sizes and densities. Other experiments described in the same reference indicated that the origin of the higher strength of specimens sintered at low pressure was the "blunting" of cracks and pressing flaws through the dissociation of SiC from all free surfaces. The resulting silicon vapor is believed to travel to cooler parts of the furnace where it recombines with carbon insulation, etc. The carbon remains on the original surface and is readily observable on all specimens sintered at low pressure. The kinetics of the dissociation are strongly influenced by the total pressure of inert gaseous species above the surface of the reaction. At low furnace pressure the reaction proceeds more rapidly than at higher pressure, thus dissociating a greater quantity of SiC and more effectively "blunting" any surface cracks, etc.

This phenomenon has been judged to be sufficiently important to warrant a more careful characterization of the strength as a function of furnace pressure during sintering. A series of 150 specimens were die-pressed in a 0.2 x 2.0 in. die at four kpsi (28 MPa) using boron-doped, β -SiC powder which had been screened through an 8 μ m screen as a dispersion in benzene, spray frozen, and freeze dried according to the procedures described previously². The bars were sintered in ten

groups of fifteen specimens in a carbon resistance furnace at pressures ranging from 0.35 to 760 torr of helium. Pressure was controlled with a cartesian diver pressure control with a small, continuous flow of helium. All specimens were heated to temperature at 1000°C per hour and held at 2085°C for 30 minutes, resulting in densities from 94 to 95 percent based on a theoretical density of 3.21 g/cm³. They were tested in the "as-sintered" state (no machining, etc.) in three-point bending on a one and one-half inch span at room temperature using the sphere-loaded test fixture described previously.² The results are plotted on Figure 1 as fracture strength vs. furnace pressure. Each data point represents the average strength of one group and the error bars include the 95 percent confidence limits on the average as calculated by Student's t-distribution. The data points of the highest and lowest furnace pressures represent two groups (30 specimens) each.

As shown in Figure 1, the lowest furnace pressures yielded an average strength of approximately 105 kpsi (720 MPa) and the highest pressure yielded approximately 80 kpsi (550 MPa). The sigmoidal shape of the dashed curve drawn through the data reflects the expected limiting strengths at both high and low pressures. As furnace pressure is decreased, the "blunting" of surface flaws by material removal can only increase the fracture strength to the point where failure is controlled by internal flaws. (Internal defects should not be affected appreciably by changing furnace pressure. Very little silicon vapor can escape to the specimen surface, therefore the internal partial pressure of silicon is always near equilibrium with effectively zero rate of dissociation). At furnace pressures below that point where

failure is controlled by internal flaws, the strength is expected to be independent of furnace pressure during sintering. The location of fracture origins supports this statement with an increasing proportion of failures observed from subsurface flaws as the furnace pressure was decreased. A lower limiting strength might also be expected at high furnace pressures where the kinetics of the dissociation reaction are reduced to the point of no material removal. This is also supported qualitatively by the observation of no free carbon on the surfaces of bodies sintered in one atmosphere of helium, whereas similar firing conditions at low pressure produce an obvious coating of carbon on all surfaces.

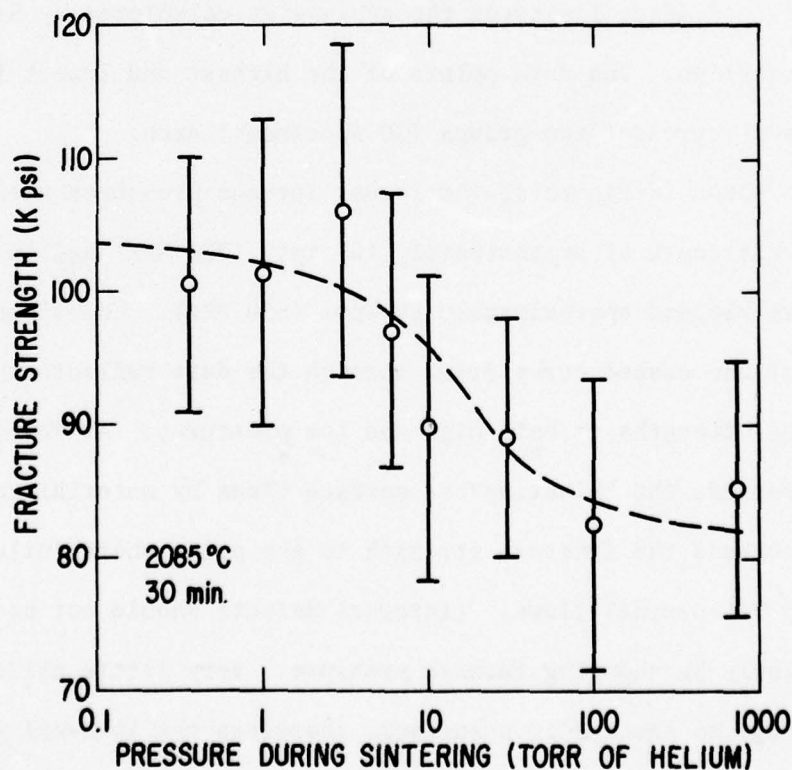


Figure 1. Effect of Furnace Pressure During Sintering on the Fracture Strength of Specimens Tested in the "As-Sintered" State

III. EFFECT OF REFIRING AFTER MACHINING ON FRACTURE STRENGTH

Another phenomenon first described in last year's final report was the use of vacuum refiring to increase the fracture strength of machined bodies. Specimens which are diamond ground are often observed to fail from machining-induced flaws. Since diamond grinding will be unavoidable for many structures which require critical dimensional tolerances, a means of repairing a large degree of the machining damage without disturbing the dimensions will be very useful.

The procedure as described previously involved refiring at or near the original sintering temperature in vacuum (0.2-0.4 torr) for 20 to 30 minutes and resulted in a 30 to 40 percent increase in the fracture strength for the machined specimens reported at that time. Refiring at or very near the original sintering temperature, however, risks both a small change in dimensions due to additional densification and an increase in the largest grain size due to exaggerated grain growth during any β to α transformation. The mechanism of strength improvement by this refiring technique is believed to be the same dissociation reaction and crack "blunting" mechanism discussed in the previous section. Since the dissociation of SiC proceeds more slowly at lower temperatures, however, there was an obvious interest in determining the lowest refiring temperature which could be used to repair machining damage. It was therefore decided to study the refiring of machined specimens at temperatures below the original sintering temperature in the hope that machining damage can be substantially repaired without the risks mentioned above.

A series of 98 specimens of SiC were prepared in the same manner as those described in the previous section. They were all sintered in vacuum (.3-.4 torr of helium) at approximately 2080°C for 20 minutes

and were diamond ground (220 grit) from approximately 0.165 in. square cross section to 0.150 in. square cross section. They were refired in vacuum in groups of 12 at six different temperatures with the remaining 26 tested without refiring to estimate the "as-machined" strength. They were tested as described in the previous section and the results are plotted on Figure 2 as fracture strength vs. refiring temperature. The specimens receiving no refiring are plotted as specimens refired at room temperature. Again each data point represents the average strength and the error bar includes the 95 percent confidence limits on the average. The strength of the as-machined specimens averaged approximately 81 kpsi (560 MPa) and, as expected, was the lowest strength. The highest average of approximately 96 kpsi (660 MPa) was measured for those specimens refired at the original sintering temperature.

Despite the rather large degree of scatter, a dashed curve was drawn through the data of Figure 2 as a suggested relationship between strength and refiring temperature. Again, the sigmoidal shape reflects the limiting effects which are expected at very high and very low refiring temperatures. At progressively higher temperatures the strength will become limited by internal flaws while at progressively lower temperatures there is negligible dissociation of SiC.

The data from these experiments suggest that the greatest degree of strength recovery in machined specimens requires a refiring temperature no lower than the original sintering temperature. It is expected, however, that the increased benefits of refiring at 100°C or more below the sintering temperature will more than compensate for the small sacrifice in strength. Another variable which may be useful but has not been characterized is the effect of longer refiring times than the 20 minutes of this

study. Based upon the present understanding of the phenomenon, one can safely predict that longer refiring times will shift the entire curve of Figure 2 slightly to the left (comparable strengths achieved at lower temperatures and longer times).

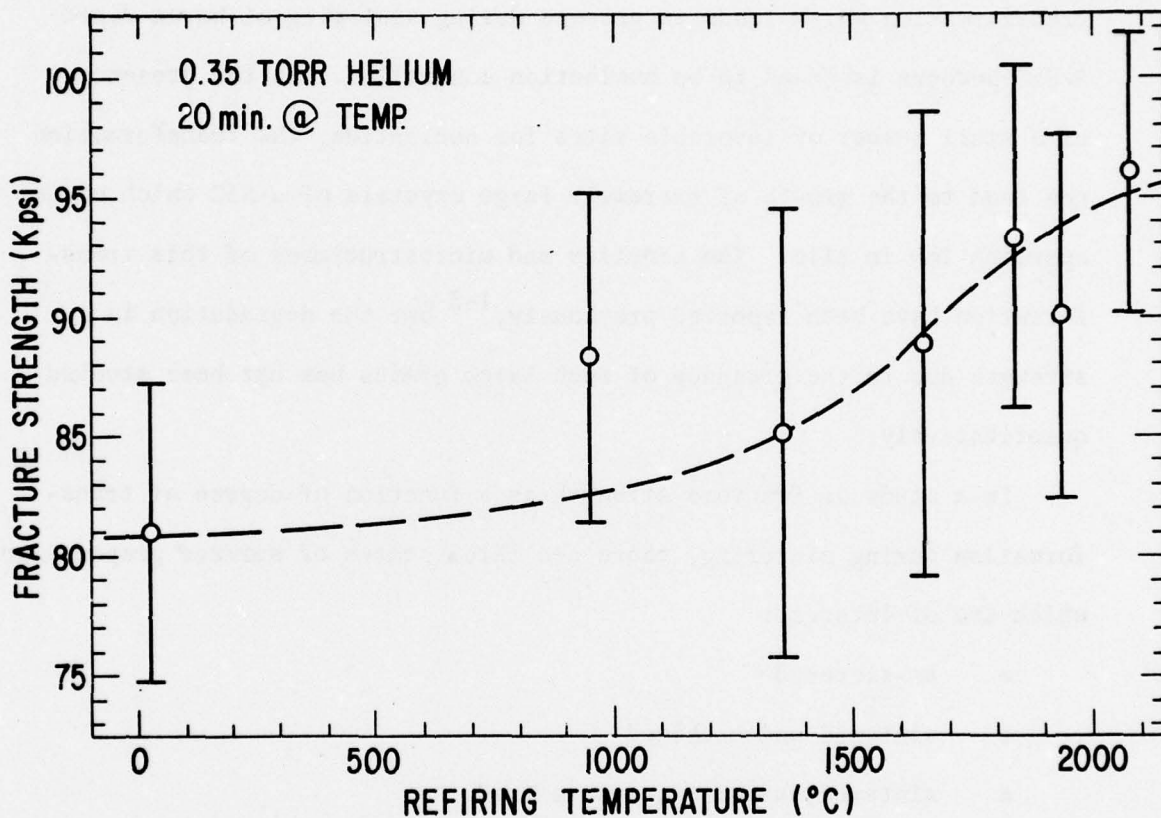


Figure 2. Fracture Strength as a Function of Refiring Temperature for Machined Specimens

IV. EFFECT OF β TO α TRANSFORMATION ON FRACTURE STRENGTH

The cubic polytype of SiC, β or 3C, is generally observed to be thermodynamically unstable relative to several of the non-cubic α polytypes in the temperature regime of 1800 to 2200°C. The phase transformation which tends to proceed during sintering of boron-doped β -SiC powders is found to be nucleation controlled. In the presence of a small number of favorable sites for nucleation, the transformation can lead to the growth of extremely large crystals of α -SiC which often approach 1mm in size. The kinetics and microstructures of this transformation have been reported previously,¹⁻³ but the degradation in strength due to the presence of such large grains has not been studied quantitatively.

In a study of fracture strength as a function of degree of transformation during sintering, there are three states of surface preparation which are of interest:

- as-sintered
- sintered and machined
- sintered, machined, and refired.

Unfortunately, it is difficult to prepare specimens in the as-sintered state with a uniform degree of transformation through the specimen thickness. The cross section of a sintered body which is partially transformed generally consists of a thin "skin" ($\sim .5\text{mm}$) of primarily β -SiC on all free surfaces with the remainder of the body uniformly transformed.² The most viable means of measuring the fracture strength is in bending where the highest tensile stresses are located at and near the surface of the specimen. The results of bend testing in the as-sintered state would not represent the properties of the bulk of such transformed specimens but would be strongly biased by the

properties of the β -SiC "skin". The present study was therefore limited to the latter two surfaces preparations where specimens with uniform microstructures could be prepared by grinding from larger sintered bodies.

A series of 100 specimens were prepared in a manner similar to that described in Section II. The bars were sintered in five groups of 20 at temperatures of 2055, 2075 (2 groups), 2095 and 2115°C for 30 minutes to produce an acceptable range of transformation with a minimum variation in density (95-96% of theoretical). The as-sintered dimensions were approximately 0.165 x 0.165 x 1.65 in. In order to avoid the gradient in microstructure described above, each specimen was diamond ground to a cross section of 0.100 x 0.100 in.

The relative amounts of β and α polytypes were determined by X-ray diffraction techniques.⁴ The results are included in Figure 3 as percent of transformation to α -SiC polytypes versus the sintering temperature. The amount of transformation varied from approximately 5 percent at the lowest sintering temperature to approximately 95 percent at the highest temperature. Two of the five groups were sintered at 2075°C (separate firings) but resulted in significantly different amounts of transformation as seen in Figure 3.

The microstructures of the five firings are included in Figures 4a-e as relatively low magnification optical micrographs of polished and etched sections. The polished sections were etched with boiling Murakami's reagent (60 g KOH + 60 g $K_3Fe(CN)_6$ + 120 ml H_2O) for five minutes. As described elsewhere,³ this etch reveals primarily α - β and α - α grain boundaries and only reveals β - β grain boundaries as very low contrast

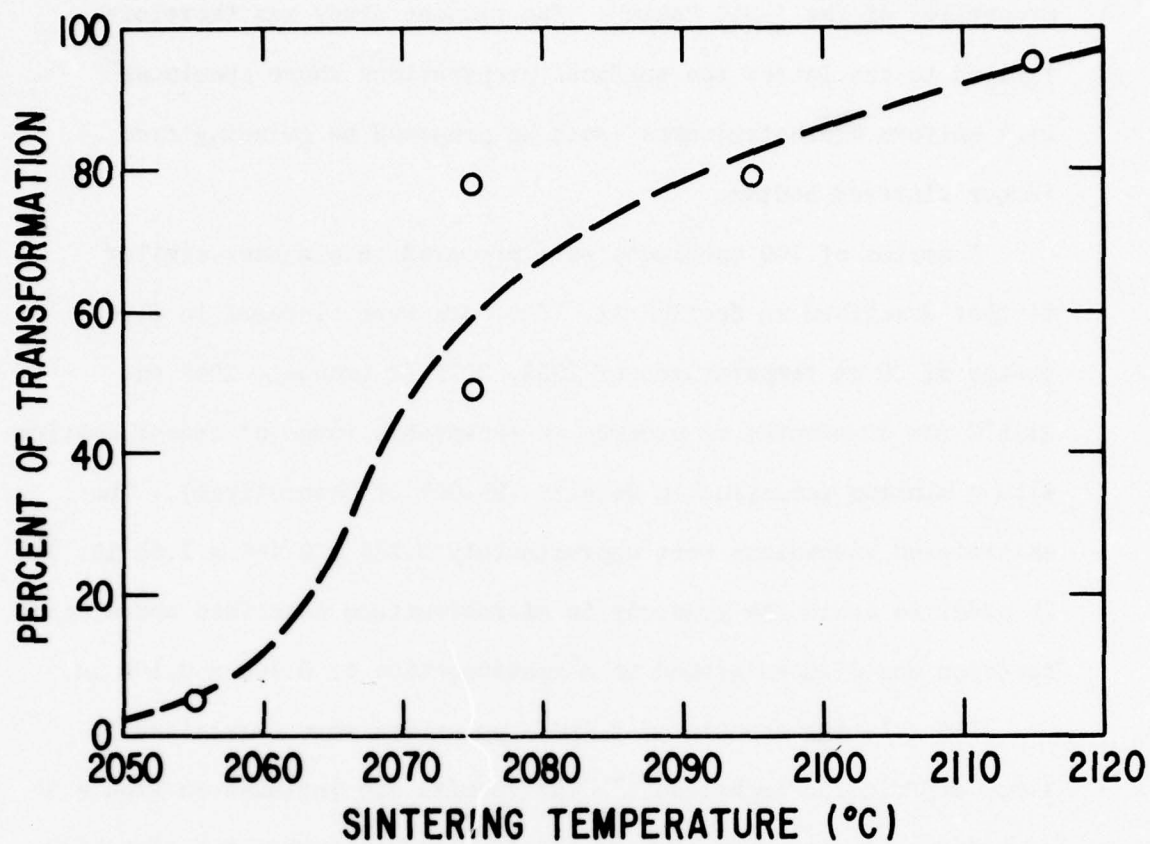


Figure 3. Degree of β to α Polytype Transformation Versus Sintering Temperature for 30 Minutes at Temperature

features at high magnification (molten KOH is generally more useful for revealing β - β grain boundaries). The transformed α -SiC in these microstructures appears in two distinct morphologies of "platelets" and "feathers", both of which have been described in some detail in References 1 and 3. At low sintering temperatures, platelets appear to predominate as the preferred morphology of α growth, while feathers predominate at higher temperatures.

Strength testing was carried out at room temperature in three-point bending on a one inch span using a sphere-loaded testing fixture as described previously.² Of each group of 20 specimens, 10 were tested in the as-machined state and 10 were refired in vacuum at 1960°C for 40 minutes before testing. As discussed in Section III this refiring treatment is generally found to decrease the severity of surface flaws such as those produced during machining. The relatively low refiring temperature of 1960°C was chosen to minimize the risk of any further transformation during the refiring treatment.

The results of bend testing are included on Figure 5 as fracture strength versus percent of transformation to α -SiC. The open and closed data points represent the average strengths of as-machined and refired specimens respectively and the error bars include the 95 percent confidence limits on the averages. In this study, no significant difference in strength could be resolved between the specimens tested in the as-machined condition and those tested after refiring. This lack of strength increase after refiring suggests that the strength was controlled by internal flaws rather than machining damage. Based on the conclusion that refiring has no significant effect on the strength of these specimens, a single curve was drawn through all the data of Figure 5. The strength decreased with

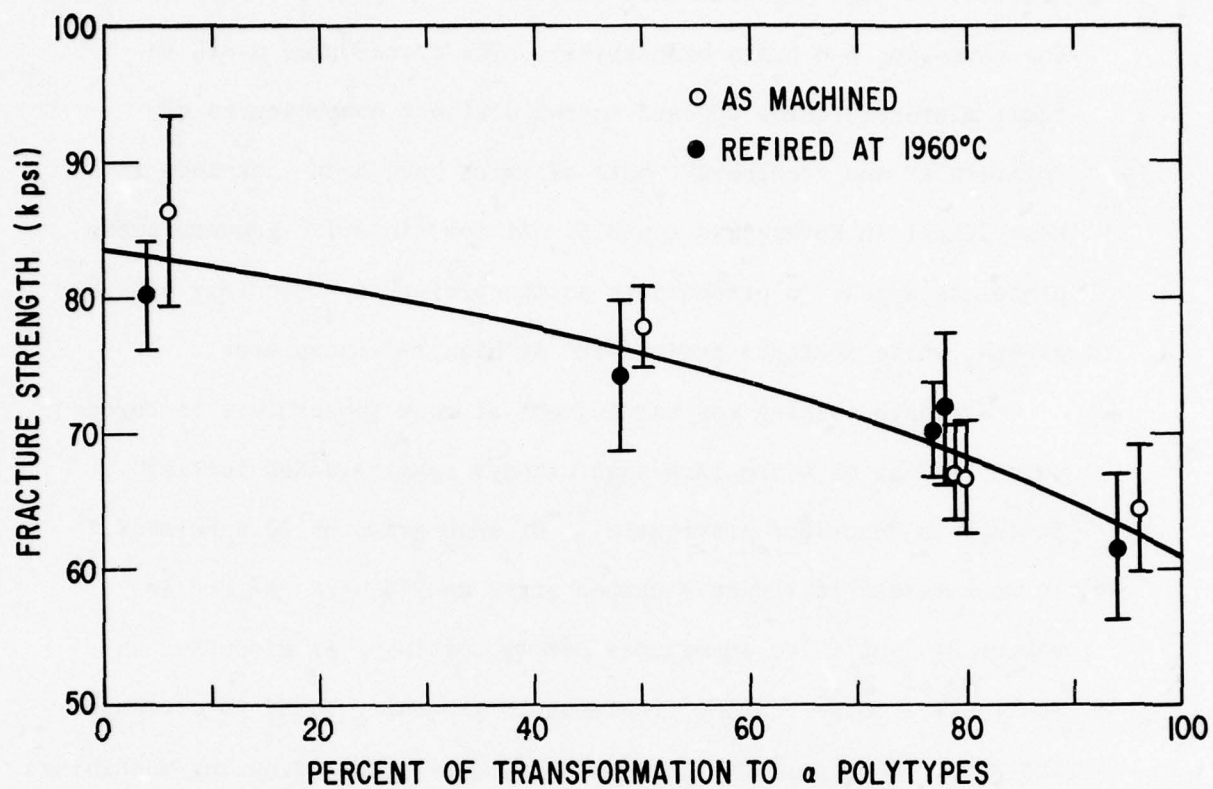
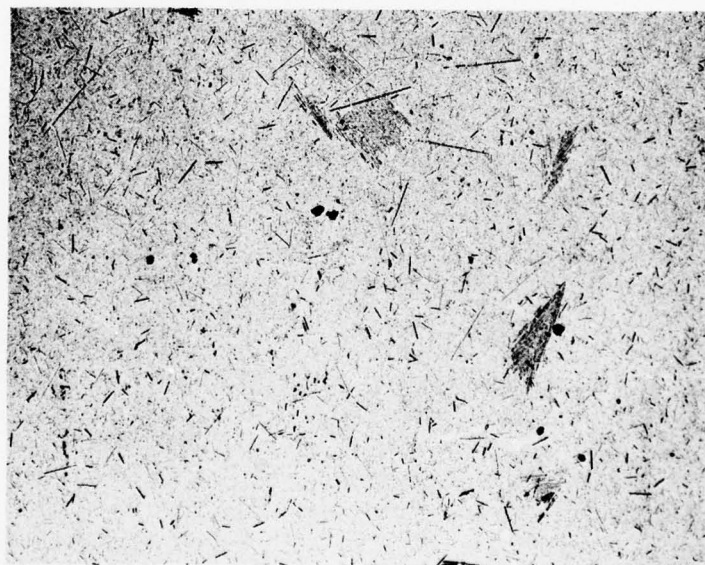


Figure 5. Fracture Strength as Measured in Three-Point Bending Versus Degree of Transformation

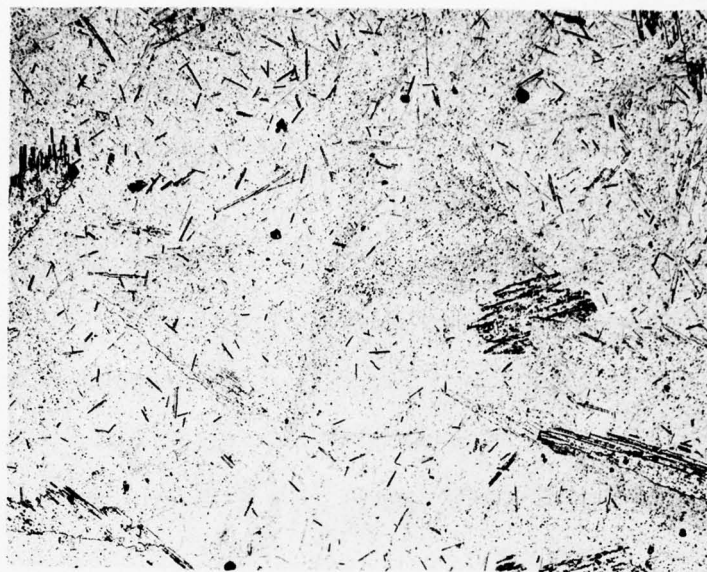
increasing transformation from a maximum of approximately 85 kpsi (580 MPa) at 100 percent β to a minimum of approximately 60 kpsi (420 MPa) at 100 percent α -SiC.

It should be emphasized that the data of Figure 5 is meaningful only for SiC which transforms into microstructures similar to those shown in the micrographs of Figure 4. Transformation into other microstructures such as small platelets or uniform, equiaxed grains of α -SiC would undoubtedly result in a different behavior of strength versus transformation.



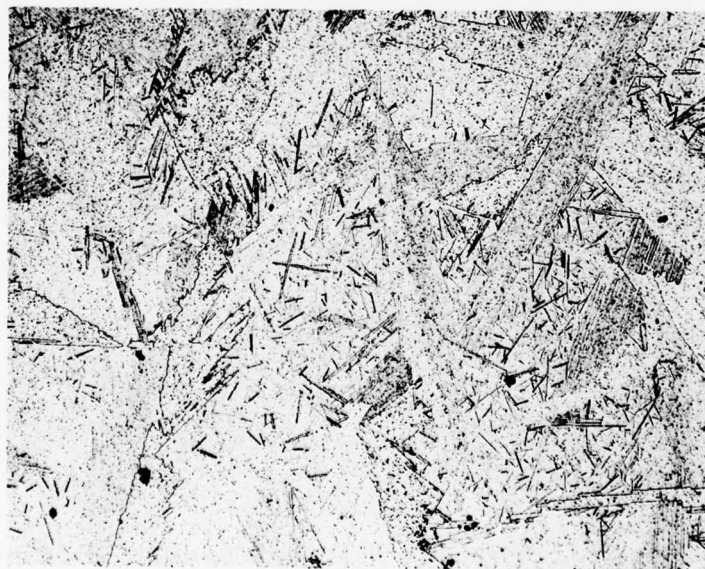
a. 2055°C

Figure 4. Polished and Etched Sections Illustrating the Effect of Sintering Temperature on Microstructure. 100X. Etched with Murakami reagent.



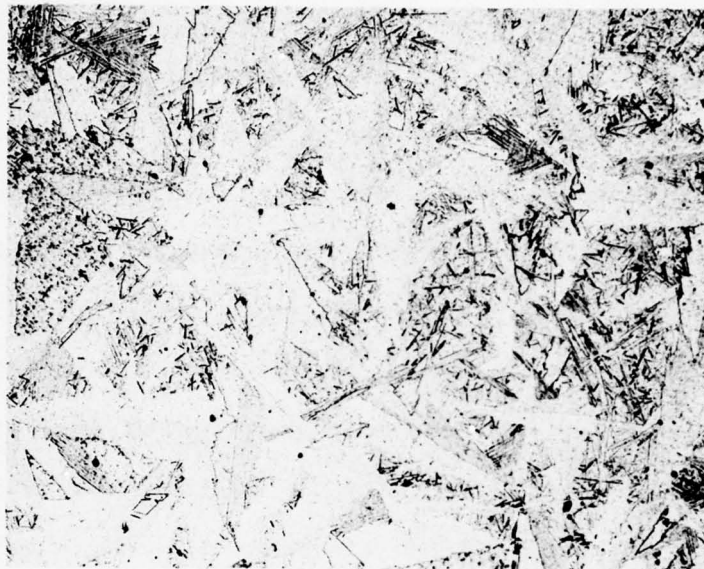
b. 2075°

Figure 4. (Cont'd)



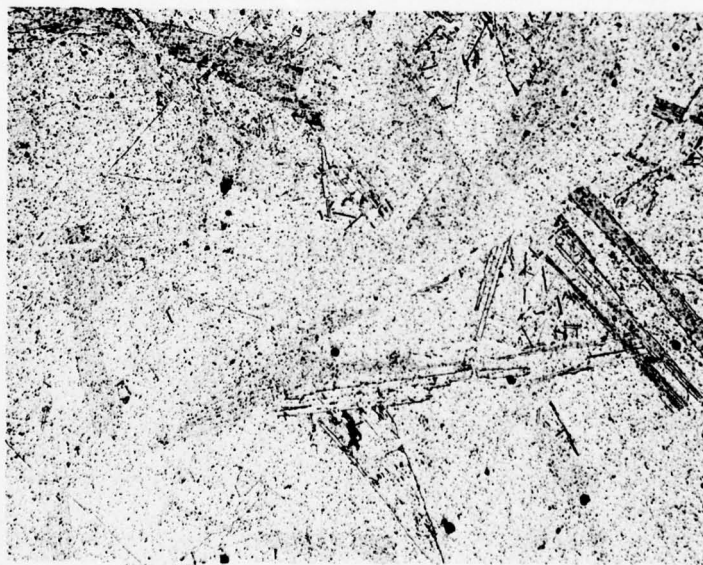
c. 2075°

Figure 4. (Cont'd)



d. 2095°C

Figure 4. (Cont'd)



e. 2115°C

Figure 4. (Cont'd)

V. EFFECT OF OXIDATION ON FRACTURE STRENGTH

The successful application of non-oxide ceramics as high temperature structural materials will require adequate resistance to oxidation and corrosion under operating conditions. Both SiC and Si_3N_4 are thermodynamically unstable in oxidizing environments, but the rates of oxidation are generally controlled by the mobility of oxygen through the oxide layer. In cases of theoretically dense, chemically pure SiC's and Si_3N_4 's (such as those made by CVD processes) the rates of oxidation are remarkably slow, even at temperatures of 1550 to 1600°C,^{1,5} thus illustrating the excellent potential of pure SiO_2 as a barrier to oxygen diffusion. Spalling, cracking or chemical contamination of the SiO_2 layer will obviously increase the mobility of oxygen through the oxide layer and are therefore undesirable.

The oxidation behavior of boron-doped, sintered SiC has been reported at rates comparable to that of CVD SiC.¹ Such behavior can probably be attributed to the relatively high purity of the oxide layer, especially if the 1/2 w/o boron addition is continually removed from the SiO_2 as volatile B_2O_3 . In light of the excellent oxidation resistance of sintered SiC, a relatively low priority was assigned to the task of characterizing the fracture strength as a function of exposure to oxidizing environments. This priority was raised, however, by recent reports in the literature of unexpectedly large strength losses after oxidation in commercially available hot-pressed SiC's and Si_3N_4 's.^{6,7} An example, Ford has reported in their ARPA contract⁶ that the average bend strength of Norton's hot-pressed Si_3N_4 , NC 132, decreased from 110 to 35 kpsi (760 to 240 MPa) after an exposure of 1000 hours

at only 1370°C.

In response to this increased concern, a series of 60 bend specimens were prepared in a manner similar to that described in Section II to study the response of sintered SiC to static oxidation in air at 1500°C for times to 2000 hours. The specimens were sintered in a carbon resistance furnace at approximately 2055°C for 30 min. at a furnace pressure of 0.4 torr, resulting in final densities of approximately 94 percent of theoretical. Prior to oxidation, the specimens were ground parallel to the specimen length to a cross sectional dimension of 0.150 x 0.150 in. Twenty of the bend specimens were reserved as controls, while the remaining 40 specimens were oxidized in a MoSi₂ resistance heated furnace. The specimens were held vertically by placing them in shallow holes drilled in a hot-pressed billet of ZrSiO₄. Zircon was chosen for the specimen holder because of its compatibility with SiC and SiO₂ in oxidizing environments. The furnace was initially loaded with all 40 specimens, heated to 1500°C for 10 hours and cooled to room temperature, after which 10 specimens were removed. In a similar fashion, the remaining 30 specimens were removed in 3 groups of 10 after integrated exposures of 200, 1000, and 2000 hours at 1500°C.

Four of the ten specimens exposed for the full 2000 hours were weighed initially and each time the furnace was cooled, thus providing data on weight gain due to oxidation. These results are included as the open circles on Figure 6 where weight gain is plotted versus the square root of time. The circles represent the averages of the four weight gain measurements and the error bars include the 95 percent confidence intervals on the averages. The data points fall quite well on a straight line with a slope of 0.054 mg/cm²/hr^{1/2}, thus

suggesting a parabolic rate of oxidation. Parabolic kinetics are commonly observed when the rate of oxidation is controlled by the diffusion of oxygen through a coherent, non-spalling oxide layer. The appearance of the oxide on these specimens, however, suggested that some spalling began between 200 and 1000 hours and continued through the end of the experiment. In order to estimate the total amount of spalling after 2000 hours, the four specimens that were weighed through the experiment were placed in hydrofluoric acid to remove all of the SiO_2 and were weighed once again. The difference between this weight and the initial (pre-oxidation) weight of each specimen represented the amount of SiC removed by oxidation. Since each mole of oxidized SiC formed one mole of SiO_2 , one can easily predict the total weight gain including that SiO_2 which spalled from the surface. The single square data point on Figure 6 represents this calculated total weight gain due to oxidation after 2000 hours at 1500°C . The difference between the circle and the square data points at 2000 hours is the best estimate of the weight of SiO_2 lost due to spalling. The non-linear dashed curve included on Figure 6 represents an estimate of the total weight gain versus time corrected for errors due to spalling. It was drawn tangent to the parabolic oxidation line at times less than 200 hours where no spalling was observed and was connected to the data point at 2000 hours with a smooth relationship.

The fracture strengths of all 60 specimens were measured in three-point bending at room temperature using a sphere-loaded test fixture with a 1.5 in. span. The results are included on Figure 7 as fracture strength versus the square root of exposure time at 1500°C . (This was a convenient time axis to plot the range of exposure times including zero.) Again,

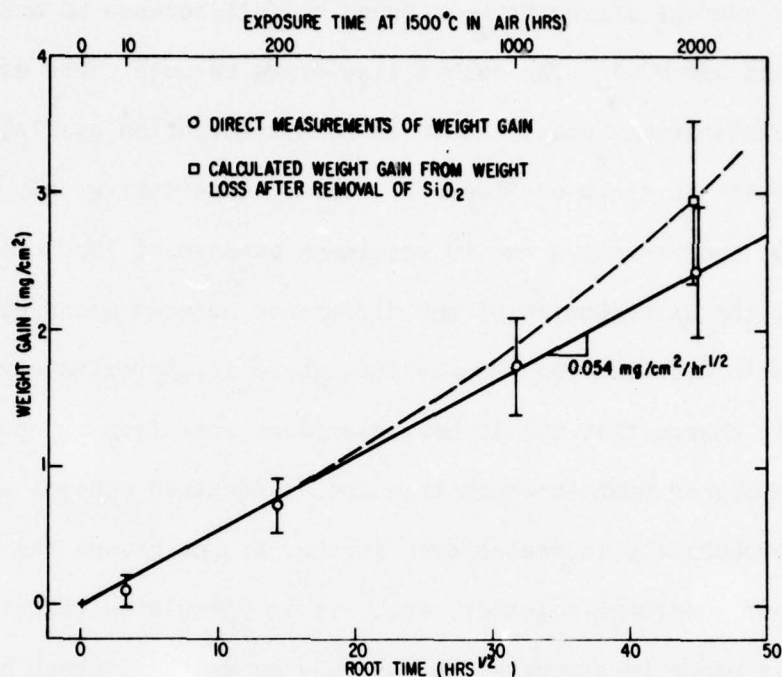


Figure 6. Weight Gain Due to Oxidation as a Function of the Square Root of Exposure Time at 1500°C in air

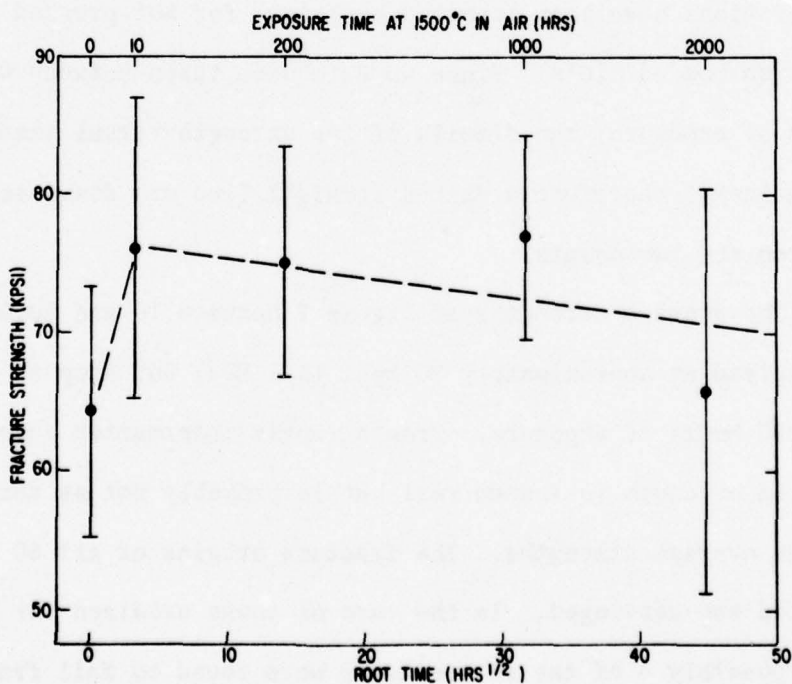


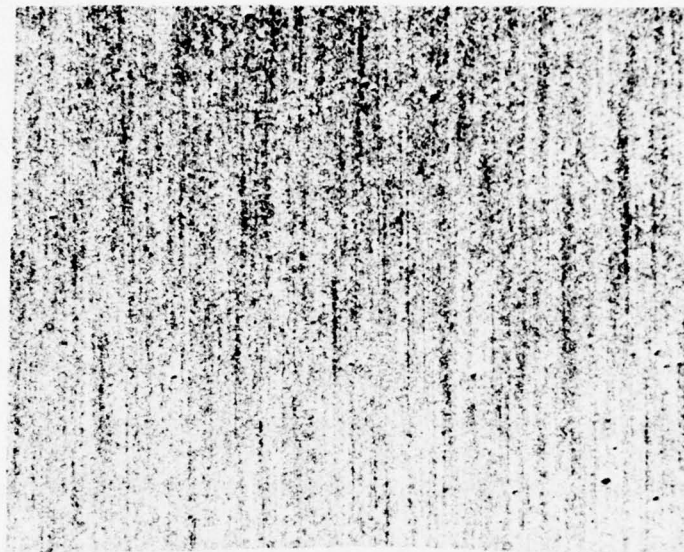
Figure 7. Fracture Strength as a Function of the Square Root of Exposure Time at 1500°C in Air

the data points represent the average strengths and the error bars include the 95 percent confidence intervals on the averages. All of the average strengths were found to fall between 60 and 80 kpsi (440 and 530 MPa). The dashed line drawn through these data requires some explanation because there is more information available than that which is shown on Figure 7. First, considering only the 20 control specimens and the 10 specimens exposed at 1500°C for 10 hours, the distribution of the difference between means using Student's distribution reveals that there is approximately a 90 percent chance that the 10 hour specimens come from a population with a higher mean strength than the as-machined control specimens. This probability increases even further as one groups the 10 and 200 hour specimens together, etc. It is speculated that the cause of this probable strength increase may be another "crack blunting" mechanism where surface defects are reduced in severity by material removal at the crack tips, in this case, by oxidation. Similar observations have been reported by Lange⁸ for hot-pressed and reaction-bonded SiC's. Since no data were taken between 0 and 10 hours of exposure, the details of the strength versus time relationship are unknown, therefore a dashed straight line was drawn schematically between the two points.

The average strengths of Figure 7 between 10 and 1000 hours appear to plateau at approximately 76 kpsi (525 MPa) but drop to 65 kpsi (450 MPa) by 2000 hours of exposure. Fractographic information suggests that this drop in strength is indeed real but is probably not as abrupt as suggested by the average strengths. The fracture origins of all 60 specimens were located and cataloged. In the case of those oxidized for 1000 hours, 3 or possibly 4 of the 10 specimens were found to fail from a type of surface "pit" which was not evident in specimens oxidized for shorter times. In the specimens oxidized for 2000 hours, these pits were larger

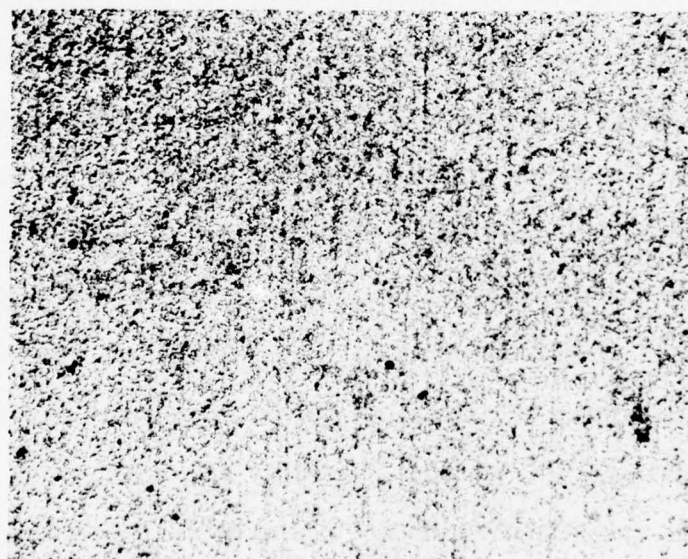
in size and accounted for at least 6 of the 10 failures. Removal of the SiO_2 from several specimen fragments revealed that the surfaces contained many localized areas which were undergoing greatly accelerated oxidation. (Due to orientation effects, etc., the areas of localized attack appear to be related to the cold pressing step of the specimen fabrication). Figures 8a-e are relatively low magnification optical micrographs (using oblique lighting) of the oxidized surfaces with all SiO_2 removed. The five micrographs correspond to 0 (as-machined), 10, 200, 1000 and 2000 hours of exposure at 1500°C respectively. The initial stages of localized attack are evident even at 10 hours of oxidation (Figure 8b), but the resulting pits are apparently not sufficiently severe defects to cause failure. After 1000 and 2000 hours of oxidation (Figures 8d and e), the larger pits measure 50 to $100\mu\text{m}$ in size and are sufficiently severe to decrease the average fracture strength. The dashed curve on Figure 7 beyond 10 hours of exposure was drawn schematically as a straight line and was included primarily to show that the strength decreased with increasing exposure time in some fashion that is not yet satisfactorily defined.

In summary, the rate of static oxidation of sintered SiC in air at 1500°C is nearly parabolic with a rate constant of $0.054 \text{ mg/cm}^2/\text{hr}^{1/2}$. The first few hours of oxidation appear to increase the average strength approximately 10 to 15 percent, possibly through a crack blunting mechanism. An accelerated mode of localized oxidation was found to cause surface pitting and an associated decrease in fracture strength after exposures approaching 2000 hours. Nevertheless, the average strength of specimens tested in bending was no lower after 2000 hours of exposure at 1500°C than the strength of as-machined specimens.



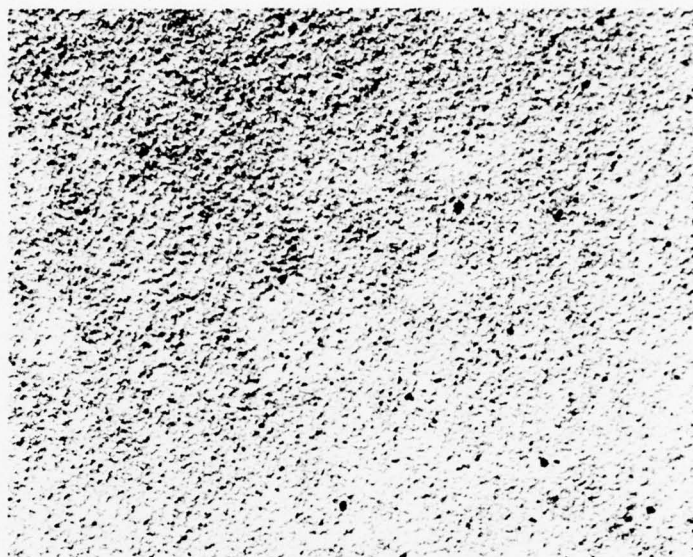
a. As-Machined

Figure 8. Optical Micrographs (50X) of Specimen Surfaces After Oxidation at 1500°C and Removal of SiO₂ in HF



b. 10 hrs

Figure 8. (Cont'd)



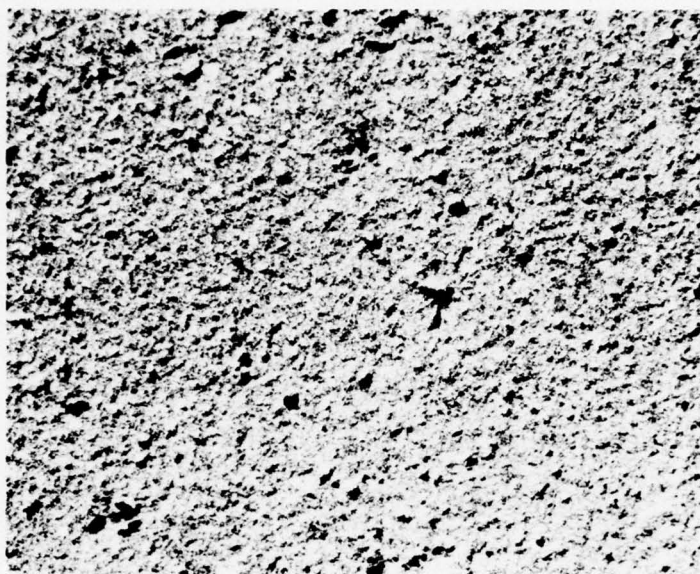
c. 200 hrs

Figure 8. (Cont'd)



d. 1000 hrs

Figure 8. (Cont'd)



e. 2000 hrs

Figure 8. (Cont'd)

VI. FRACTURE STATISTICS

The ability to effectively design highly stressed components of any structural ceramic will require an accurate description of the statistical nature of fracture. Unlike most metals, ceramics will require this additional design criteria to account for the large variability in strength which is commonly observed in brittle materials and to account for the size dependence of strength which is a natural consequence of the variability. A proper description must relate the stress at which failure occurs to several dependent variables including:

- the cumulative probability of failure--higher stresses can be supported if higher probabilities of failure are acceptable;
- the specimen size--larger specimens have a greater probability of containing a large flaw and therefore can support less stress; and
- the stress distribution--a body under uniform tensile stress has a higher probability of failing at its most deleterious flaw than a similar body with only a small fraction of its volume under the maximum stress.

The probabilistic nature of fracture in brittle materials originates from variability in the severity of defects. In turn, the statistical functions which are used to describe the macroscopic effects of such variability can be reduced to descriptions of the flaw size distribution. When viewed in this manner, it is evident that a proper description of the statistical aspects of fracture in a given material is extremely sensitive to any factors in the material fabrication process which may affect that flaw size distribution. Such factors certainly include changes

in powder processing and material fabrication techniques. As will be described in more detail in Section IX, the large internal voids in sintered SiC (originally discussed in last year's final report²) are probably caused by weak agglomerates formed during the powder processing steps. Work is under way in a concurrent program to identify modified powder processing and material fabrication techniques to avoid such defects. In light of this potential change in both the powder processing technique and the resulting flaw size distribution, the decision was made to delay the massive testing program necessary to satisfactorily characterize the fracture statistics of the present form of sintered SiC. Nevertheless, efforts in the area of fracture statistics have continued during the last year but were directed toward the development and verification of both experimental and mathematical tools to be used in the future. Some initial spin testing has been carried out on sintered SiC and the statistical parameters of all the various groups of bend specimens have been calculated, but the two areas of fracture statistics to be discussed in detail here are:

- A means of quantitatively determining the statistical parameters of fracture from the positions of fracture origins was derived and demonstrated for two-parameter Weibull statistics.
- Two sets of literature data were reanalyzed to quantitatively illustrate examples of multiple flaw distributions.

The most useful mathematical descriptions of fracture statistics presently available are based on weakest link models combined with

empirical distribution functions. One very popular example is Weibull fracture statistics⁹ which is generally reported to describe experimental data reasonably well. It should be emphasized, however, that the Weibull distribution function is not derived completely from first principles but, rather, is an empirical description of the probability of failure. In fitting experimental data to such a mathematical function, a great deal of caution must be exercised in extrapolating the function beyond the data base. In spite of the weaknesses caused by its empirical nature, the relatively simple distribution function of Weibull fracture statistics provides a useful model to illustrate mathematical manipulations that may require numerical methods for a more complex distribution function. For this reason, the Weibull distribution was used in both of the discussions to follow. Since both sections will refer to specifics of the Weibull distribution function, it will be useful to begin by reviewing the form of the distribution function.

The Weibull distribution function relates the cumulative probability of failure (P) to the volume (V) under tensile stress (σ) with two parameters--the Weibull modulus (m) and a normalizing constant (σ_0) as follows:

$$P = 1 - \exp \left[- \int_0^V \left(\frac{\sigma}{\sigma_0} \right)^m dV \right] \quad (1)$$

This form of the function has two adjustable parameters and integrates over the volume of the specimen. Thus it is generally referred to as two-parameter, volume Weibull statistics. Other variations of the Weibull distribution function can include a third adjustable parameter and may integrate over the surface of the body rather than the volume

(if all flaws are expected to be surface flaws). The Weibull modulus, m , is a measure of the scatter or dispersion of the distribution (similar to the standard deviation of a normal distribution) where a small m represents a large degree of scatter. Most ceramics are reported to have m 's in the range of four to ten, whereas metals are estimated to have m 's in the range of 50 to 100. The normalizing constant σ_0 , is an indirect measure of the average strength. For instance, if the Weibull modulus, the specimen size and the loading configuration are held constant, the average strength is directly proportional to σ_0 .

For bodies under uniform tension, the integration of Equation 1 is trivial, but for the general case where the stress in a body is a function of position, the integration must be carried out either analytically or numerically. As an example, the stress in a rectangular beam in three-point bending can be described analytically as:

$$\sigma = \frac{6 P x y}{w h^3} \quad (2)$$

where P is the center point load, x is the distance from the nearest outer load point, y is the distance from the neutral axis, w is the specimen width and h is the specimen height. Substituting this into Equation 1, expanding the volume integral into a triple integral and rearranging results in:

$$P = 1 - \exp \left[-2 \left(\frac{\sigma_M}{\sigma_0} \frac{4}{hL} \right)^m \int_0^w \int_0^{h/2} \int_0^{L/2} (xy)^m dx dy dz \right] \quad (3)$$

where σ_M is the maximum tensile stress in the beam. Integration of

this expression yields:

$$P = 1 - \exp \left[- \frac{1}{2(m+1)^2} V \left(\frac{\sigma_M}{\sigma_0} \right)^m \right] \quad (4)$$

or

$$P = 1 - \exp \left[-K_V V \left(\frac{\sigma_M}{\sigma_0} \right)^m \right] \quad (5)$$

where K is a "load factor"

$$K_V = \frac{1}{2(m+1)^2} \quad (6)$$

The load factor for the more general case of four-point bending with volume flaws can be derived from Equation 1 in a similar manner and results in:

$$K_V = \frac{\left(\frac{a}{b}\right)^m + 1}{2(m+1)^2} \quad (7)$$

where a is the inner span and b is the outer span. Equation 7 correctly reduces to Equation 6 for three point bending where the inner span, a, is zero. In those cases where failure is controlled by surface flaws, Equation 1 should be integrated over all elements of surface rather than volume. The resulting load factor for four-point bending can be related to Equation 7 as follows:

$$K_A = K_V \left(\frac{mw}{w+h} + 1 \right) \quad (8)$$

where w and h are the specimen width and height respectively.

The product of K_V times V is often referred to as the "effective volume" under tension and, as the term implies, can be pictured as the volume of material which is effectively being tested under uniform tension. Accordingly, K_S times surface area is the effective area under uniform tension. Equation 1 can be integrated either analytically or numerically to the form of Equation 5 for a stressed body of any

geometry and loading configuration. Except for the case of uniform tension, the resulting load factors will always be numerically less than one and will always be a function of m .

The Weibull modulus and σ_0 can be estimated from fracture data by a number of methods, but all of the common ones can be classified into one of two categories. The most popular methods require fracture strength measurements on a number of specimens of identical geometry. The fracture strengths are ordered from weakest to strongest, and each is assigned a probability of failure based on its ranking, n , as follows:

$$P = \frac{n}{N+1} \quad (9)$$

where N is the total number of data points. A regression analysis can then be performed using Equation 5 at constant KV to find the best values for m and σ_0 to describe all N data points (each data point consists of a fracture strength and an associated probability of failure). Variations of this method arise from different possible weighting factors of the data in the regression analysis.

One of these methods is very convenient because it allows a simple linear regression analysis of the data. Equation 5 can be manipulated and rearranged into the following form:

$$\ln \ln \left(\frac{1}{1-P} \right) = m \ln \sigma_M + \ln \left(\frac{KV}{\sigma_0^m} \right) \quad (10)$$

This is an equation of a straight line and is therefore easily subjected to linear regression. Equation 10 also allows a convenient graphical representation of the data as shown schematically in Figure 9 by plotting $\ln \ln \left(\frac{1}{1-P} \right)$ vs $\ln \sigma_M$. The slope of the least squares line through the data is m and the position of the line defines σ_0 . It should be noted that the maximum stress of each specimen is used in all of this discussion

despite the fact that fracture in three-point bend specimens, for example, virtually never originates exactly at the line of maximum tensile stress.

The other common method of estimating the Weibull parameters requires the measurement of fracture strength at a variety of effective volumes. Rearranging Equation 5 again yields:

$$\ln \sigma_M = - \frac{1}{m} \ln KV + \ln \sigma_o + \frac{1}{m} \ln \ln \frac{1}{1-P} \quad (11)$$

At a constant probability of failure, this defines a linear relationship between σ_m and $\ln KV$. Graphical representation of this equation is shown schematically in Figure 10 as $\ln \sigma_M$ versus $\ln KV$ with the slope of the line equal to $-\frac{1}{m}$. The data to be plotted on such a graph should be at constant probability of failure, thus one can plot average strengths or, somewhat more correctly, median strengths. Again, variations of this method arise from different types of regression analysis on the data points.

Graphical representations of data such as Figures 9 and 10 also allow judgements concerning the quality of the distribution function in describing the data. If the data points are clearly non-linear on such plots, then the distribution function does not adequately describe the behavior, regardless of the choice of statistical parameters m and σ_o .

VI-A. Derivation of Statistical Parameters of Fracture from the Locations of Fracture Origins

The previous review of fracture statistics has been included as background on which to base the derivation of yet another independent means of estimating the statistical parameters and judging

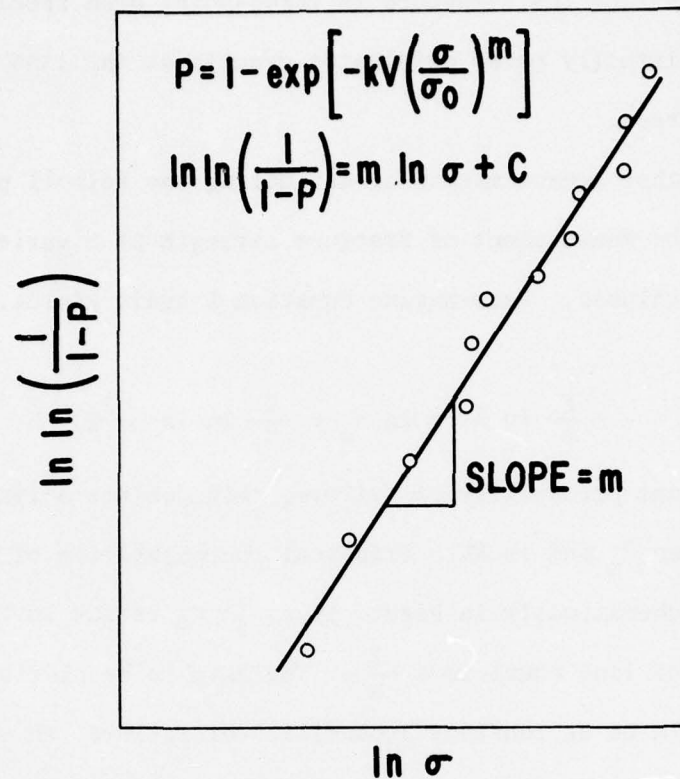


Figure 9. Schematic Drawing Illustrating a Means of Estimating the Weibull Modulus from Probability of Failure and Fracture Strength

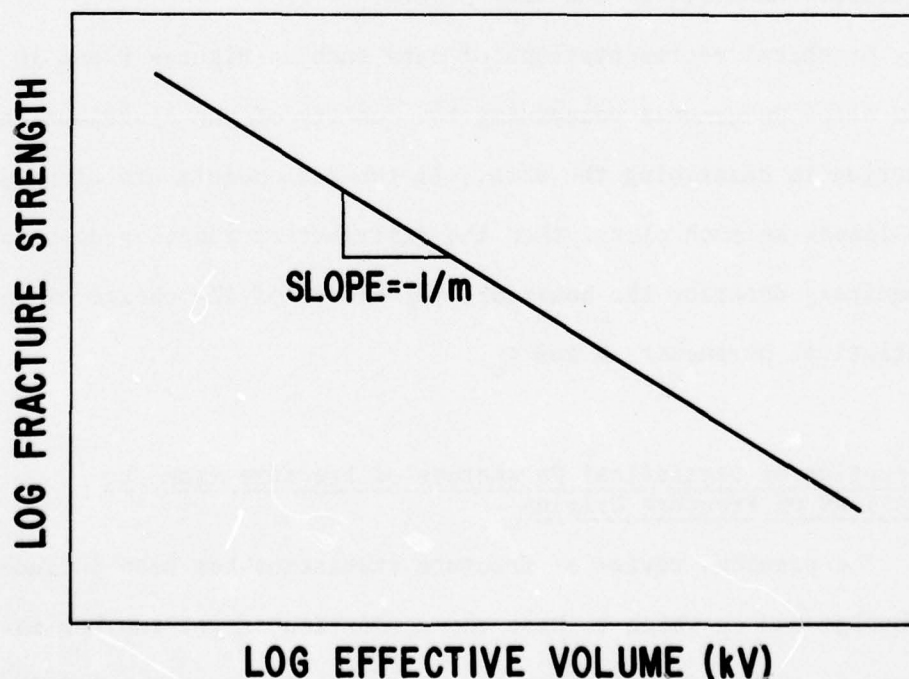


Figure 10. Schematic Drawing Illustrating a Means of Estimating the Weibull Modulus from Fracture Strength and Effective Volume

the validity of a distribution function. This method uses additional information from fracture specimens which is easily measured but not normally compiled. The method is restricted to test specimens which contain stress gradients (such as bend specimens) and the additional measurements necessary for the analysis are the positions of the fracture origins.

The distribution of positions of fracture origins is strongly influenced by the variability in strength as can be demonstrated by first considering the limiting case of a material with no variability in strength (standard deviation = 0; $m = \infty$). In such a hypothetical material, failure will always occur at exactly the same stress, and no element of volume can survive a higher stress. When tested in three-point bending the fracture origins will always be located exactly on the line of maximum tensile stress. If one now considers a material with some variability in strength, the most probable position for failure in bending remains on the line of maximum tensile stress, but not all failures will initiate there. Due to the variability in strength from location to location, failure will often occur at positions where the stress is somewhat lower than the maximum. Accordingly, the fraction of origins located away from the line of maximum tensile stress will increase with increasing variability in fracture strength (or decreasing m), thus providing a means of estimating the variability in strength by measuring only the positions of fracture origins.

Two-parameter volume Weibull statistics and three-point bend specimens have been chosen to illustrate the mathematics of this method, but the underlying logic should be valid for any distribution function of interest and any loading configuration except uniform tension. The position of a fracture origin in a three-point bend

specimen can be related to the ratio of the stress at the fracture origin to the maximum stress in the beam without any knowledge of the actual fracture stress, load, etc. by the following relationship:

$$\frac{\sigma}{\sigma_M} = \frac{4 x y}{hL} \quad (12)$$

where x is the distance from the fracture origin to the nearest outer load point, y is the distance from the origin to the neutral axis, h is the specimen thickness and L is the specimen length. This ratio of stress to maximum stress will be referred to as the relative stress, R . Contours of constant relative stress can be calculated for a beam by rearranging Equation 12 to yield:

$$y = \frac{1}{x} \frac{\sigma}{\sigma_m} \frac{hL}{4} = \frac{R}{x} \frac{hL}{4} \quad (13)$$

For a constant value of relative stress, σ/σ_M , this equation describes a family of hyperbolae with a common origin on the neutral axis at an outer load point. Figure 11 is the side view of a bend specimen showing several contours of constant relative stress.

The total probability of failure of a three-point bend specimen was derived earlier by integrating Equation 3 with appropriate limits of integration to include the entire volume of the specimen under tensile stress. In deriving m from the positions of fracture origins in a material with volume flaws, a similar integration must be carried out except that the limits of integration are chosen to include only that portion of the specimen at a relative stress greater than a given limit. For instance, if the chosen relative stress were 0.8, then the result would be the probability that fracture would originate in the volume of material contained within the 0.8 relative stress contour of Figure 11. To distinguish it from the total probability of failure, P or P_T , the result of this integration will be referred to as P_R

for probability of failure at a relative stress greater than R. The form of this equation for three-point bending with the proper limits of integration is:

$$P_R = 1 - \exp \left[-2 \left(\frac{\sigma_M}{\sigma_0} \frac{4}{hL} \right)^m \int_0^w \int_{\frac{RhL}{4x}}^{h/2} \int_{\frac{RL}{2}}^{L/2} (xy)^m dx dy dz \right] \quad (14)$$

which can be integrated to:

$$P_R = 1 - \exp \left[-CKV \left(\frac{\sigma_M}{\sigma_0} \right)^m \right] \quad (15)$$

where:

$$C = 1 - R^{m+1} \quad (1 - \ln R^{m+1}) \quad (16)$$

For the case of $R=0$, the integration is carried out over the entire volume of the specimen, therefore P_R should equal P_T . Substituting $R=0$ into Equation 16 results in $C=1$, thus Equation 15 correctly reduces to Equation 5. The other simple limiting case is $R=1$. Since there is no volume at a relative stress greater than one, the probability of failure in that volume must be zero. Substituting $R=1$ into Equation 16 results in $C=0$, thus Equation 15 correctly predicts $P_R=0$.

More useful than P_R is the ratio of P_R to P_T . For a given value of relative stress, this is the probability of failure occurring in positions of the specimen within that stress contour divided by the total probability of failure of the entire specimen. This ratio therefore corresponds to the fraction of fracture origins which are located at a relative stress greater than R.

$$\frac{P_R}{P_T} = \frac{1 - \exp \left[-CKV \left(\frac{\sigma_M}{\sigma_0} \right)^m \right]}{1 - \exp \left[-KV \left(\frac{\sigma_M}{\sigma_0} \right)^m \right]} \quad (17)$$

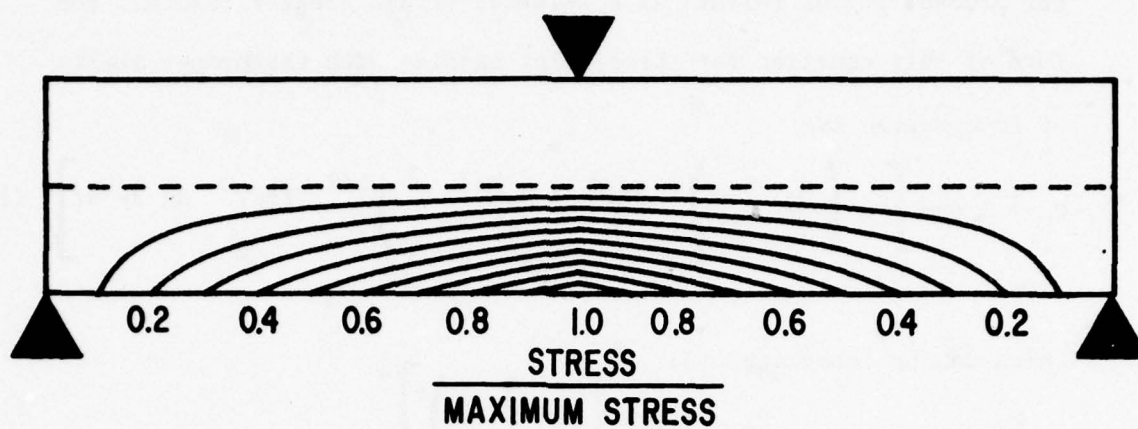


Figure 11. Contours of Constant Relative Tensile Stress in a Three-Point Bend Specimen

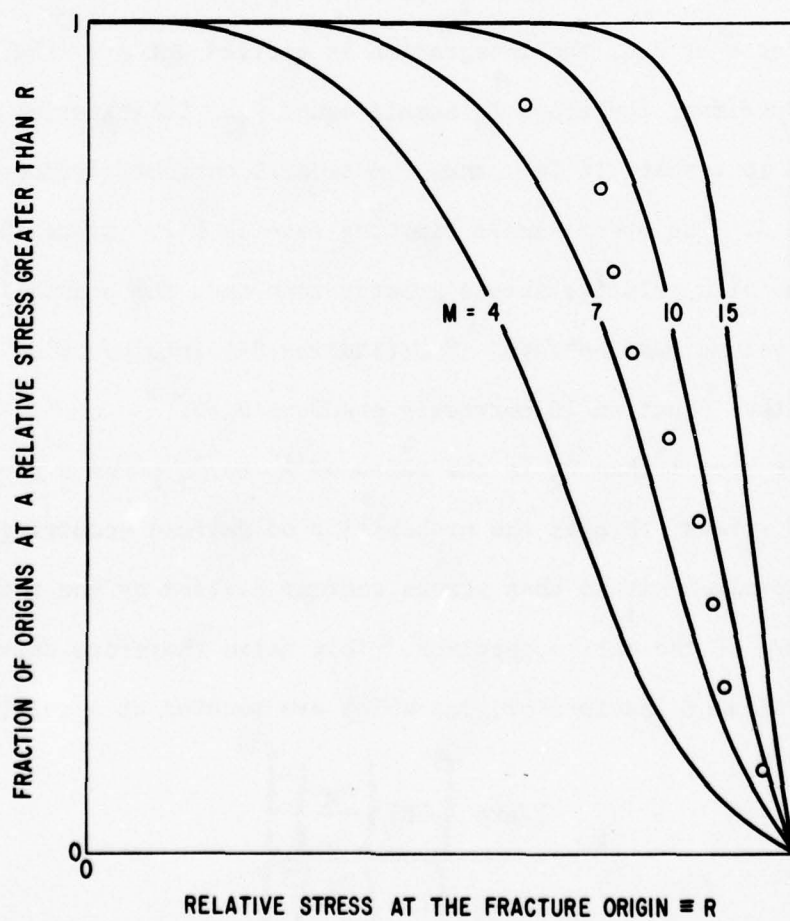


Figure 12. Schematic Drawing Illustrating a Means of Estimating the Weibull Modulus from P_R/P_T and R

If this ratio is independent of the total probability of failure, P_T , then the Weibull modulus, m , can be predicted solely from the positions of fracture origins with absolutely no knowledge of the magnitude or variability of the actual fracture strengths. A graphical approach for such a situation is shown in Figure 12 where P_R/P_T is plotted schematically as a function of R for several values of m . Experimentally the position of the fracture origin in each of several bend specimens would be measured and the values of relative stress calculated by Equation 12. These relative stresses would be ranked in order of decreasing R from 1 to N and the values of P_R/P_T estimated by:

$$P_R/P_T = \frac{n}{N+1} \quad (18)$$

The resulting N data points would then be plotted on Figure 12 (as shown for a hypothetical set of nine data points) and the Weibull modulus estimated from the positions of the data relative to the plotted curves. More accurate estimations could be calculated, of course, by iteratively searching for the value of m with the least scatter of data about the predicted line.

Unfortunately, the relatively simple procedure described in the previous paragraph cannot be used because the ratio of P_R/P_T is not independent of the total probability of failure. Stated another way, the ratio is a function of the maximum stress at the time of failure, σ_M , as seen on the right side of Equation 17. This dependence of P_R/P_T on the total probability of failure is illustrated quantitatively on Figure 13 where P_R/P_T is plotted as a function of R (same axes as Figure 12) for several values of P_T at a constant Weibull

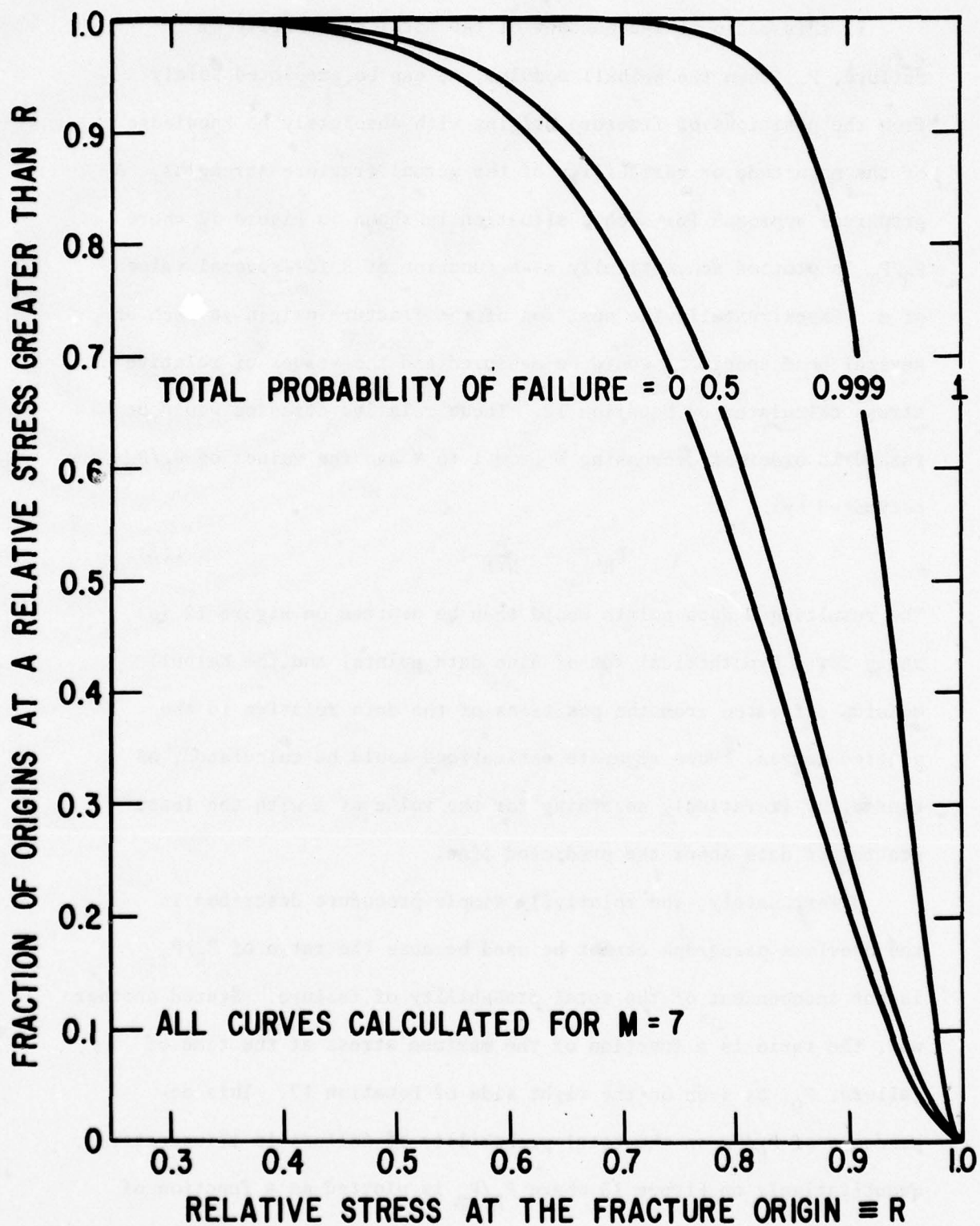


Figure 13. P_R/P_T Versus R at Constant m Illustrating the Dependence of the Position of Fracture Origins on the Total Probability of Failure, P_T

modulus of 7. At low total probabilities of failure, the function is insensitive to P_T , but as the total probability of failure approaches unity there is a distinct tendency for failure to occur closer to the line of maximum stress. In the limit of $P_T = 1$, all failures should occur exactly on the line of maximum tensile stress. Stated in other words, the probability of a specimen failing at a given position is not only a function of the Weibull modulus, but also depends on whether that particular specimen is the strongest or weakest specimen of the batch.

At this point, there are four interrelated variables which are of interest: m , R , P_R/P_T , and P_T . All four variables cannot conveniently be illustrated at the same time in two dimensions, therefore Figures 14 and 15 both plot relative stress at the fracture origin versus total probability of failure. Figure 14 includes a family of curves where P_R/P_T was varied and the Weibull modulus held constant at $m = 7$. Figure 15 includes a similar family of curves where m was varied and P_R/P_T was held constant at 0.5.

The simplified method discussed above (Figure 12) required estimates of R and P_R/P_T for each specimen, after which m could be predicted graphically. The dependence of fracture origin position on total probability of failure as illustrated in Figures 13-15 somewhat complicates this method of predicting m . In addition to R and P_R/P_T , an estimate of P_T is needed for each specimen. Unfortunately, this requires some information concerning the actual fracture strengths which was not needed for the earlier model. The ranking of strengths in increasing order combined with Equation 9 is sufficient

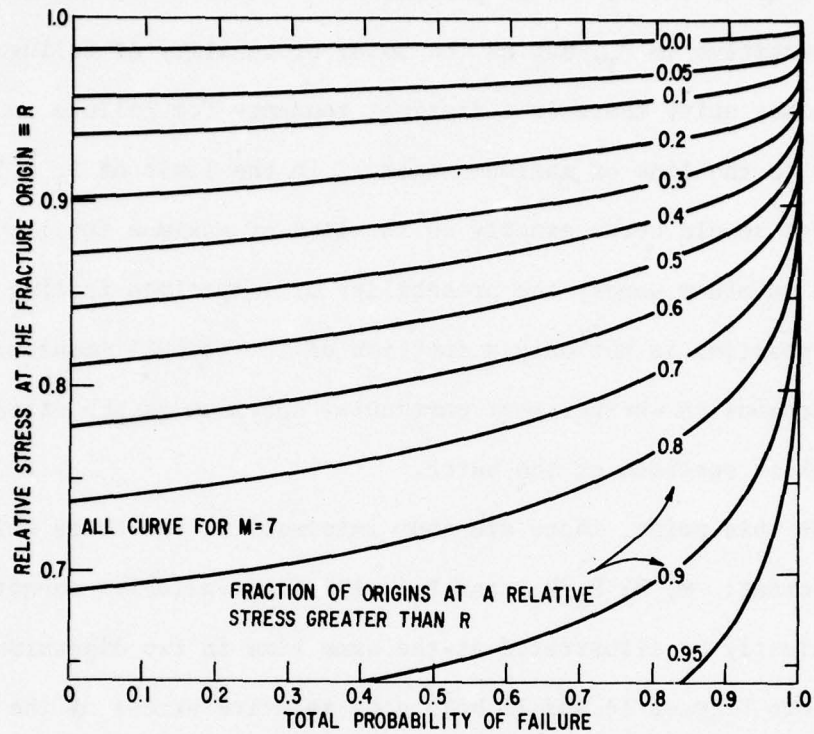


Figure 14. R Versus P_T at Constant m for Various Values of P_R/P_T

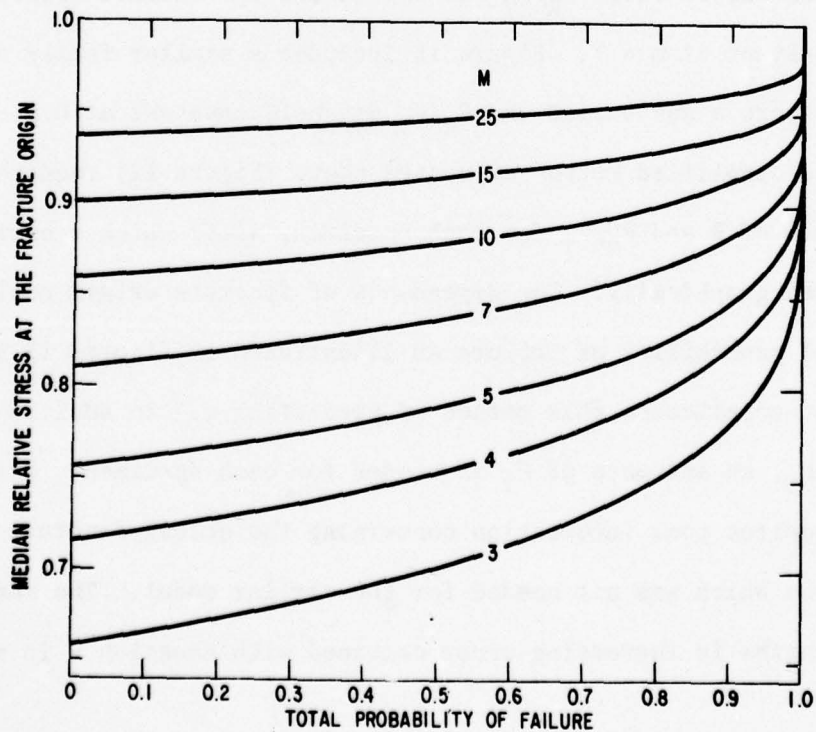


Figure 15. R Versus P_T at Constant P_R/P_T for Various Values of m

to estimate a total probability of failure for each specimen. In order to estimate the Weibull modulus, the resulting data are plotted on a three-dimensional equivalent of Figure 12 (P_T is the third axis). Since three-dimensional graphs are difficult to construct, the most feasible approach is an iterative least squares technique with the aid of a computer.

Experimental verification of this technique required a material with only a single distribution of flaws and with easily identifiable fracture origins. As discussed previously², boron-doped, sintered SiC has been found to contain several different flaw distributions and therefore was not chosen. Instead, cylindrical rods of pyrex glass tested in three-point bending were chosen for this demonstration. A series of 45 specimens of 5 mm diameter rod were cut into three inch lengths. To insure that failure occurred from only one flaw distribution, the specimens were uniformly abraded by tumbling for two hours in a slurry containing 220 grit SiC abrasive powder.

The previous outline for estimating m from fracture origins was discussed in terms of a distribution of volume flaws in a rectangular specimen. The analysis therefore had to be revised for the present case of a distribution of surface flaws in a cylindrical specimen. The resulting relationship describing P_R in terms of R , σ_M , etc. (the equivalent to Equation 14) is a double integral which cannot be completely integrated.

$$P_R = 1 - \exp \left[- \frac{DL}{m+1} \left(\frac{\sigma_M}{\sigma_o} \right)^m \int_0^{\cos^{-1} R} \left(\cos \Theta^m - \frac{R^{m+1}}{\cos \Theta} \right) d\Theta \right] \quad (19)$$

D is the specimen diameter and Θ is the angle from the fracture origin

to the position of maximum tensile stress. The remaining integration can, of course, be performed numerically.

The abraded specimens were tested at room temperature in three-point bending on a two inch span at a loading rate of approximately 50 kpsi/min (340 MPa/min) and resulted in an average strength of 14.1 kpsi (97.2 MPa). All fracture origins were located on the specimen surface. The position of each origin was defined by measuring the distance from the origin to the nearest outer load point and the angle from the origin to the point of maximum tensile stress. These measurements were taken on each half of the specimen and averaged. The relative stresses were ranked and used in Equation 18 to estimate P_R/P_T , and the strengths were ranked and used in Equation 9 to estimate P_T . The resulting 45 sets of R , P_T , and P_R/P_T were entered into a computer program to iteratively find the most suitable value of m in Equation 19 to describe the data. The result was a Weibull modulus of 12.9.

For the sake of comparison, the Weibull modulus was also estimated in a conventional manner from the fracture strengths using the linear regression method illustrated earlier in Figure 9. This resulted in a Weibull modulus of 11.4 which compares quite favorably with the estimate of 12.9.

In summary, a method was outlined to determine the Weibull modulus of a group of specimens using primarily the locations of fracture origins in specimens with stress gradients. The method does not employ the numerical values of fracture stress and is therefore independent of those methods of estimating m which do require fracture stresses. The example illustrated in detail was two-parameter volume Weibull statistics on a three-point bend

specimen, but the approach which was outlined can be applied to different specimen geometries and distribution functions. This method of determining the Weibull modulus is not meant to replace the conventional methods reviewed earlier, but rather is meant to supplement them by more effectively using all of the information concerning the variability of flaw sizes that is available in a group of test specimens. In light of the time, effort and expense associated with the fabrication and testing of fracture specimens, a means of nearly doubling the resulting statistical information per specimen is very attractive. In addition to providing more efficient utilization of available data, the above discussion on the distribution of fracture origin positions has yielded useful information on two related subjects:

- The most popular view of fracture statistics attributes the observed effects to variations in flaw size from location to location combined with the weakest link concept. A less popular explanation attributes the effects to errors in the testing technique including both measurement errors and errors due to misalignments of the specimen and fixtures. If the scatter in strengths is primarily due to testing errors instead of variations in flaw sizes, then there should be little or no dependence of strength on specimen size. Also, if there is indeed no variability in flaw sizes (the true $m = \infty$), fracture should always originate at the location of the highest tensile stress and the only scatter in fracture origin positions should be due to variability in the nature of the parasitic stresses from specimen to specimen. It is very unlikely in this case that the scatter in fracture

strengths and the scatter in fracture origin positions would coincidentally lead to the same value of Weibull modulus. Therefore approximately equivalent values of m as calculated by the two techniques (such as illustrated in the example of abraded glass rods) helps to support variability in flaw sizes as the source of the observed scatter in fracture strengths.

- As mentioned earlier in this section, the fracture strength of a specimen is correctly quoted as the maximum tensile stress in that specimen even though failure in bending, for example, virtually never occurs exactly at the position of maximum stress. A number of investigators reporting in the literature have been concerned with the use of σ_M as the best description of the fracture strength and instead have measured the location of the fracture origin, calculated the stress present at that location at the time of failure and incorrectly used that number to calculate the average strength and the Weibull modulus. This approach leads to significantly low estimates of both the average strength and the Weibull modulus, but both can be quantitatively related to the correct values through the information on Figures 13-15.

VI-B. Multiple Flaw Distributions

Careful fractography of most ceramic materials will reveal more than one type of fracture initiating flaw within a set of specimens. The source of these flaws are many and include machining damage, inclusions of foreign material, large voids or void clusters due to

powder agglomeration, etc. Each type of flaw is present in the material as a distribution of flaw sizes and densities which, in most cases, is totally independent of all other flaw distributions. The consequences of multiple independent flaw distributions was discussed in some detail in last year's final report,² but no data were presented to substantiate the conclusions. The primary material being studied in this contract is boron-doped sintered SiC and, as also discussed in last year's final report, at least four different flaw distributions are active in three-point bend specimens of this material. A very large number of specimens would be necessary to satisfactorily characterize each flaw distribution. Such information will eventually be required but at present is not available for sintered SiC.

The effect of multiple flaw distributions can be illustrated at present, however, by using published data on other ceramic materials which are reasonably well characterized and which do not exhibit such a large number of active flaw distributions. Two examples of such materials have been chosen for the present discussion. In both cases the original authors kindly provided more detailed test results than those available in the literature. The first example is based on a study of CVD SiC fibers tested in uniaxial tension by Kotchick, Hink and Tressler¹⁰ where the strength of a large number of fibers was measured as a function of gage length at a constant fiber diameter. Unfortunately, due to fragmentation after the initial specimen failure, it was not feasible to locate and classify the fracture initiating flaws. The second example to be discussed is based on a study of a commercial 96% Al_2O_3 tested in three and four-point bending by Bansal, Duckworth and Niesz,^{11,12}

where the strengths of a moderate number of specimens were measured as a function of specimen size, loading configuration and environment. In this case the fracture origins of all specimens were identified, thus helping to substantiate the existence of multiple flaw distributions. The authors of both examples concluded that conventional Weibull statistics could not describe the observed behavior. The present re-analysis of their data illustrates that two-parameter Weibull statistics describe the data satisfactorily (exceptionally well in the case of Bansal's data) if the materials are assumed to each contain two independent flaw distributions.

The problem of estimating the applicability of a particular mathematical function in describing the probabilities of failure of specimens of different sizes, geometries and loading configurations quickly reduces to a problem of graphically visualizing both the data and the predicted behavior simultaneously. In the case of a set of specimens of similar size, geometry and loading configuration, this can be done conveniently by plotting the data as $\ln \ln \frac{1}{1-P}$ vs. \ln fracture strength as shown schematically on Figure 9. If two-parameter Weibull statistics are correct, the data should fall on a straight line, but if two such distributions are active, the data will fall on intercepting straight lines as shown schematically in Figures 27 and 28 of last year's final report.² Fracture data derived from specimens of more than one size or tested in more than one loading configuration cannot all be simultaneously plotted in such a manner, therefore one must manipulate the data in order to satisfactorily incorporate all of it onto one two-dimensional plot.

Weibull two-parameter statistics have been chosen again for this discussion because the relatively simple function allows mathematical manipulations which are not possible for more complex statistical functions and because it very nicely describes the data of Kotchick et al. and Bansal et al. As discussed earlier, Equation 5 relates the maximum applied stress and the specimen volume to the probability of failure for a material with a single distribution of volume flaws. The equivalent relationship to Equation 5 for two independent volume distributions is:

$$P = 1 - \exp \left[-V \left(K_V \left(\frac{\sigma_M}{\sigma_{o1}} \right)^{m_1} + K_V \left(\frac{\sigma_M}{\sigma_{o2}} \right)^{m_2} \right) \right] \quad (20)$$

where the subscripts 1 and 2 for m 's and σ_o 's distinguish the parameters for the two distributions. Since the load factors are normally a function of m , the quantity K_V cannot be factored out of the sum in the exponential.

In the case of fracture data from multiple specimen sizes, one must choose a single specimen size, geometry and loading configuration to normalize all other data. Each original piece of fracture data consists of a fracture strength and an estimated probability of failure. Normalizing a data point to a different specimen size can be accomplished in two ways: The strength can be shifted by an appropriate amount with no change in probability of failure; or the probability of failure can be shifted with no change in the strength. The latter of these two methods is the only practical choice for multiple flaw distributions.

For the general case of normalizing data from one arbitrary specimen size, geometry and loading configuration (designated by subscripts α) to another (designated by subscripts β), one can write two equations, each of the form of Equation 20, as follows:

$$P_{\alpha} = 1 - \exp \left[-V_{\alpha} \left(K_{V\alpha} \left(\frac{\sigma_M}{\sigma_{o1}} \right)^{m_1} + K_{V\alpha} \left(\frac{\sigma_M}{\sigma_{o2}} \right)^{m_2} \right) \right] \quad (21)$$

$$P_{\beta} = 1 - \exp \left[-V_{\beta} \left(K_{V\beta} \left(\frac{\sigma_M}{\sigma_{o1}} \right)^{m_1} + K_{V\beta} \left(\frac{\sigma_M}{\sigma_{o2}} \right)^{m_2} \right) \right] \quad (22)$$

where σ_M is the same maximum stress in both specimens and where both distributions are present as volume flaws. For the case of uniform uniaxial tension ($K_V=1$) these equations can be combined, rearranged and simplified to yield:

$$P_{\beta} = 1 - (1 - P_{\alpha})^{\left(\frac{V_{\beta}}{V_{\alpha}} \right)} \quad (23)$$

It is interesting to note that the shift in probability of failure with a shift in volume (at a constant failure stress) is totally independent of the statistical parameters, m and σ_o . In fact, for the case of constant diameter specimens tested in uniaxial tension (such as the data of Kotchick et al.), it can be shown that the shift in probability is only dependent on the assumption that weakest link statistics are applicable. The amount of shift is independent of the specific function (two-parameter, three-parameter Weibull, etc.) and the number of active flaw distributions and is also correct when both volume and area distributions are active simultaneously.

A more general description than Equation 23 is needed for the data of Bansal's where the normalization of the data must accommodate changes in specimen size, changes in loading configuration and active distributions of both area and volume flaws. The equivalent relationship to Equation 23 for this general case is more complex:

$$P_{\beta} = 1 - \left(1 - P_{\alpha} \right)^{\gamma} \quad (24)$$

where,

$$\gamma = \left(\frac{K_{A\beta} A_{\beta} \left(\frac{\sigma_M}{\sigma_{o1}} \right)^{m_1} + K_{V\beta} V_{\beta} \left(\frac{\sigma_M}{\sigma_{o2}} \right)^{m_2}}{K_{A\alpha} A_{\alpha} \left(\frac{\sigma_M}{\sigma_{o1}} \right)^{m_1} + K_{V\alpha} V_{\alpha} \left(\frac{\sigma_M}{\sigma_{o2}} \right)^{m_2}} \right) \quad (25)$$

In this case, m and σ_o must be known or estimated for each distribution before any of the data can be shifted, and the result is subject to any errors in the parameters.

The work on SiC fibers by Kotchick, Hink and Tressler¹⁰ included uniaxial testing of approximately 300 fibers of Avco* CVD SiC with seven different gage lengths from 0.25 to 20 in. The fibers were approximately 0.004 in. diameter with a carbon core of approximately 0.001 in. diameter. Although SiC fibers were also tested in the abraded condition, the 300 fibers of interest in this discussion were tested with virgin surfaces. The average strengths and 95 percent confidence intervals are plotted on Figure 16 as log strength vs. log of fiber length. Two groups of specimens were tested at both the 3 and 10 in. gage lengths. For constant diameter fibers, the volume (and the area) is proportional to the length, therefore the abscissa of Figure 16 is directly proportional to a log volume scale. For a material with a single distribution of flaws obeying two-parameter Weibull statistics, average strengths should fall on

* Avco, Space Systems Division, Lowell, Mass.

a straight line (with a slope of $-1/m$) when plotted in this manner. Instead, the data of Figure 16 appear to fall on two intersecting straight lines as expected for a bimodal distribution of flaws. The parameters for the two straight lines tentatively drawn on Figure 16 are $m_1 = 35$, $m_2 = 4.0$, $\sigma_{o1} = 524$ kpsi, and $\sigma_{o2} = 50.3$ kpsi.

Unfortunately, when average strengths are plotted in the manner of Figure 16, much important information is discarded concerning the scatter of the data about each of the averages. Through the use of Equation 23, every data point can be visualized simultaneously, allowing a better judgement of the applicability of weakest link statistics, two-parameter Weibull, single or multiple flaw distributions, etc. The 300 data points of Kotchick et al. were normalized to a one in. gage length and all plotted on Figure 17 as $\ln \ln \frac{1}{1-P}$ vs. \ln strength. The two data sets at both 3 and 10 in lengths were combined before normalizing. The solid line included in Figure 17 was plotted according to Equation 20 using the same m 's and σ_o 's listed above and derived from Figure 16. In some regions of Figure 17 the data points are so densely packed that individual symbols are difficult to identify, but such a representation is still useful to concisely visualize the trends of the data. For instance, when plotted in this manner, it appears that the distribution with the lower modulus is not adequately described by an m of 4.0 as was estimated from Figure 16. A distribution with an m of approximately 5 would be more suitable.

If the non-linear trend of the data in Figure 17 is due to two active flaw distributions, then fracture origins of specimens failing in one region of the curve should be predominated by one

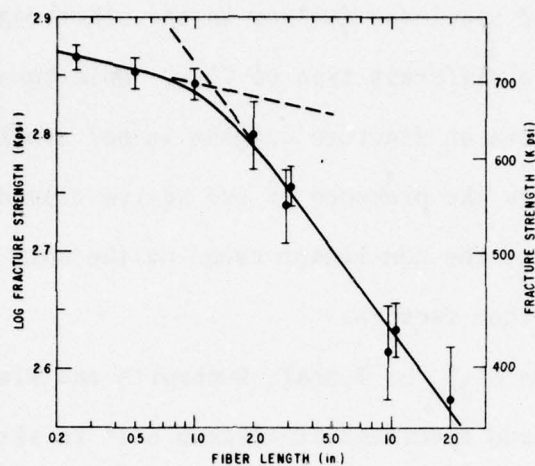


Figure 16. Fracture Strength as Measured in Tension Versus Gage Length for Fibers of CVD SiC as Reported by Kotchick et al. ¹⁰

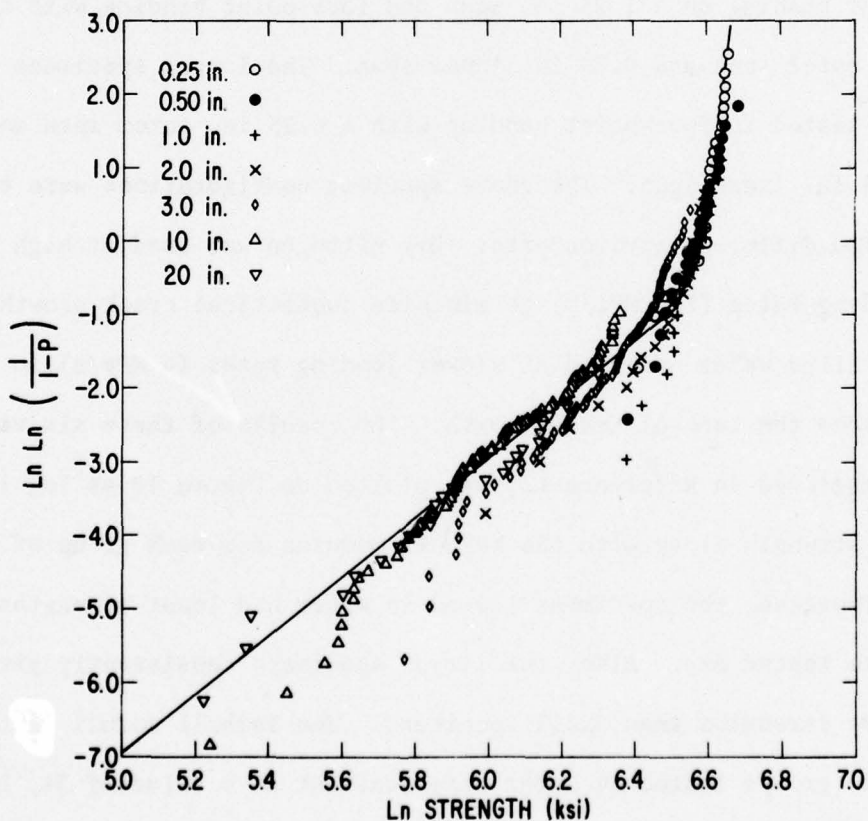


Figure 17. Weibull Plot for CVD SiC Fibers Where All Probabilities Have Been Normalized to That for Specimens with One Inch Gage Lengths. Original Data from Kotchick et al. ¹⁰.

type of flaw and specimens failing in the other region should originate from a different type of flaw. Unfortunately, this complimentary data on fracture origins is not available for the SiC fibers, therefore the presence of two active flaw distributions is not confirmed and the non-linear trend of the data on Figure 17 may be due to other factors.

The work on Al_2O_3 by Bansal, Duckworth and Niesz^{11,12} involved a total of 76 bend specimens of Alsimag 614* in six different variations of specimen size, load configuration and environment. Specimens were prepared in two sizes: 0.1 x 0.2 x 1.5 in. and 0.5 x 1.0 x 7.5 in. The smaller specimens were tested in both three-point bending on a 1.25 in. span and four-point bending with a 1.25 in. outer span and 0.75 in. inner span. The larger specimens were all tested in four-point bending with a 6.25 in. outer span and a 3.75 in. inner span. The above specimen configurations were tested in two different environments. Dry nitrogen was used at high loading rates (100 MPa/s) to minimize subcritical crack growth, and distilled water was used at slower loading rates (4 MPa/s) to enhance the rate of crack growth. The results of these six variations, as included in Reference 12, are plotted on Figure 18 as $\log \log \frac{1}{1-P}$ vs. \log strength along with the Weibull modulus for each group of specimens. As expected, the specimens tested in water had lower strengths than those tested dry. Also, the larger specimens consistently yielded lower strengths than small specimens. The Weibull moduli of the three groups tested in water were constant at a value of 34, but the moduli of the specimens tested dry varied from 34 for the small

* 3M Co., Technical Ceramic Products Division, Chattanooga, Tenn.

three-point specimens to 11 for the large four-point specimens.

Fractography as reported by Bansal et al. revealed that all specimens tested in water failed from flaws extending from the tensile surface. No voids or inclusions were associated with these flaws. Approximately 80 percent of the small specimens tested in dry nitrogen also failed from origins extending from the tensile surface. Approximately 10 percent of the origins were located at large, subsurface pores, and the remaining 10 percent could not be clearly identified. All of the large specimens tested in dry nitrogen failed from large, irregular, subsurface pores. Bansal et al. concluded from the decrease in Weibull modulus and the change in predominating flaw type with increasing effective volume when tested in dry nitrogen that there were two active flaw distributions. No attempts were made to determine if the data were consistent with relationships such as Equation 21.

Through the use of Equation 24, all of the fracture data of Figure 18 were normalized to probabilities of failure for small three-point bend specimens and were re-plotted on Figure 19 as $\ln \ln \frac{1}{1-P}$ vs. \ln fracture strength. Using the hypothesis that both area and volume flaws were active in dry nitrogen, the four Weibull parameters of the bimodal flaw distribution were needed before the data could be normalized. The parameters were varied iteratively to find that combination with the least scatter between the measured and predicted behaviors. For the specimens tested in dry nitrogen, these parameters were $m_1 = 29.1$, $\sigma_{01} = 51.2$ kpsi, $m_2 = 8.2$, and $\sigma_{02} = 35.2$ kpsi. The first two parameters describe the surface or area distribution of flaws, while the second two describe the volume related flaws.

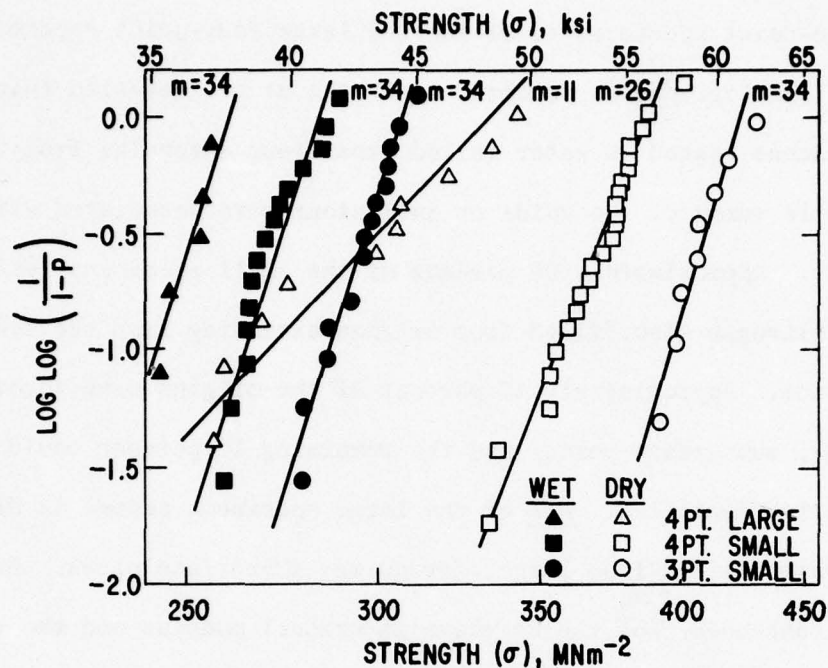


Figure 18. Weibull Plot for Al_2O_3 Showing Six Different Combinations of Specimen Size, Testing Configuration and Testing Environment as Reported by Bansal et al. ^{11, 12}

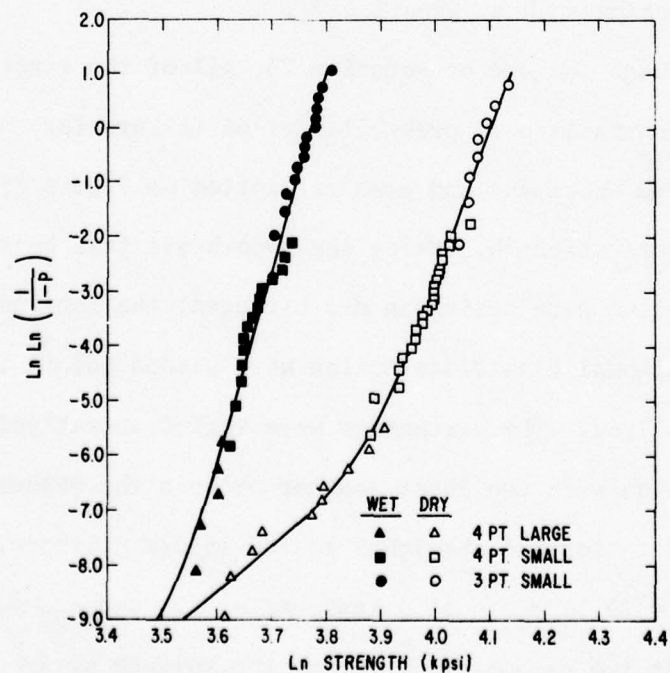


Figure 19. Weibull Plot of the Data of Figure 18 Where All Probabilities of Failure Have Been Normalized to Those of "Small" Three-Point Bend Specimens. Original data from Bansal et al. (Refs. 11 and 12).

The solid curve drawn through the dry nitrogen data of Figure 19 represents the predicted behavior of the combined distribution according to the above parameters. This curve describes the data very well and, when combined with the fractography results, provides a very convincing argument that the material contains two active flaw distributions and that each distribution can be described satisfactorily by two-parameter Weibull statistics.

The same two distributions of flaws are present in specimens tested in water. If a mechanism of subcritical crack growth becomes active due to the environment, however, the effects should be seen only on those flaws on the surface since internal flaws are isolated from the external environment in a dense material. The fracture origins of specimens tested in water were reported to be exclusively surface flaws with no failures observed at internal voids. All of the fracture data of specimens tested in water are consistent with a single distribution of surface flaws. Presumably, these flaws are of the same distribution as the surface flaws observed in dry nitrogen, but in the aqueous environment the flaws were significantly extended by subcritical crack growth prior to failure. The curve drawn through the solid data points of Figure 19 was calculated by assuming that the volume flaws observed in dry nitrogen were also present in the specimens tested in water and that they were not affected by the aqueous environment. The two parameters for the volume distribution were therefore assumed to be identical to those listed above for dry nitrogen. The remaining two parameters for the surface distribution were varied iteratively to find those which best described the data. The resulting four parameters were: $m_1 = 36.3$, $\sigma_{01} = 37.9$ kpsi, $m_2 = 8.2$ and $\sigma_{02} = 35.2$ kpsi. As seen

on Figure 19, the volume distribution of flaws should not become active within the range of probabilities of failure of the data. If more data had been collected on the large four-point specimens tested in water or if even larger specimens were tested, then one would expect that some failures would originate from the type of volume flaws that were observed in the large four-point specimens tested in dry nitrogen.

In summary, a method was described to simultaneously illustrate fracture data from more than one specimen size and geometry on a single two-dimensional plot. This technique proves to be particularly useful when a material contains multiple independent flaw distributions such as boron-doped sintered SiC. Due to insufficient data on sintered SiC at present, however, the method was illustrated quantitatively on two sets of literature data which appear to contain multiple flaw distributions.

VII. TIME-TEMPERATURE DEPENDENCE OF FRACTURE STRENGTH

One of the most important properties of a potential high temperature structural ceramic is the degree of strength degradation which occurs due to subcritical crack growth at high temperatures. All materials undergo subcritical crack growth to some degree at high temperature, thus resulting in a time-dependence of fracture strength. The velocity of subcritical crack growth for a given material is a complex function of temperature, stress and environment (gas phase composition). At constant temperature and environment, the velocity of crack growth, v , is often described empirically as a power function of the stress intensity factor, K ^{13,14}

$$v = A K^n \quad (26)$$

where A and n are experimentally determined material constants.

Crack velocity can be measured directly in tests such as the double cantilever beam and the double torsion tests, however, experimental problems can arise in these direct measurements at very low crack velocities. Indirect methods such as constant stress (stress rupture) and constant loading rate tests can also be used to evaluate the parameters of Equation 26 and are more amenable to testing at very low crack velocities (long times to failure).

It has been shown elsewhere¹⁵ that Equation 26 can be integrated over the total time to failure at a constant stress thus yielding the relationship:

$$\sigma^n \tau = k \quad (27)$$

where σ is the applied stress, τ is the time to failure and k is a constant which includes the critical stress intensity factor, the "quick-time" fracture strength and the constant, A , of Equation 26.

In a similar manner, Equation 26 can be integrated over the total time to failure in a constant loading rate test (conventional mode of bend testing), thus yielding a similar relationship:

$$\sigma^n \tau = k(n+1) \quad (28)$$

According to Equations 27 and 28, stress rupture and constant loading rate data should fall on straight lines when plotted as log fracture stress versus log time to failure as shown schematically on Fig. 20. The linear slope in both cases should equal $-\frac{1}{n}$ and the horizontal separation of the two lines should be $\log(n+1)$. Plotting the data in this manner provides a simple graphical means of predicting the stress rupture behavior from constant stress-rate data, but the relationships in Figure 20 are subject to the validity of Equation 26.

Charles¹⁶ has recently proposed an expression for crack velocity which was derived in a more fundamental manner than Equation 26 from a model of stress-directed vacancy diffusion at crack tips. The crack velocity predicted from this model can be simplified to the following form:

$$v = \frac{A}{x} \exp \beta K \quad (29)$$

where x is the instantaneous crack length and A and β are material constants which can be related to thermodynamic properties through the derivation. The unique aspect of this expression is the crack length in the denominator of the pre-exponential. The model assumes that the rate of crack growth is controlled by diffusion of vacancies from the bulk of the specimen to the crack tip (or conversely, by diffusion of atomic species from the crack tip into the specimen). The crack length in the denominator arises because the average diffusion distance is believed to vary in direct proportion to the crack length.

(If Equation 29 is correct, it is interesting to note that stress intensity versus crack velocity curves which are common in the literature require a third axis of crack length).

Equation 29 has been integrated for the case of constant stress¹⁶. The resulting relationship, when plotted on the axes of Figure 20, is concave downward with an initial slope (short times to failure) that is a function of the thermodynamic properties of the material and a final slope (at very long times to failure) of $-1/4$. The inverse fourth power dependence at long times to failure is predicted to be common to all materials -- metals and ceramics alike. Unlike the case of constant stress, Equation 29 cannot be integrated for the case of linearly increasing stress without resorting to numerical integration. The resulting relationship, when plotted on the axes of Figure 20, is also concave downward and shifted to the right of the constant stress behavior, but the amount of shift is not simply $\log(n+1)$ as it was for the relationships derived from Equation 26. Using data available from the literature, Charles has shown that Equation 29 is remarkably accurate in describing the time-temperature dependences of strength in both metals^{16,17} and ceramics^{17,18}.

Results included in last year's final report² indicated that boron-doped sintered SiC has excellent resistance to high temperature subcritical crack growth when compared with other potential structural ceramics. This area of strength degradation at high temperatures is sufficiently important for the eventual application of sintered SiC, however, that work has been expanded during the previous year. The areas to be discussed in this report include:

- The stress rupture behavior of pressurized tubes at temperatures in the vicinity of 2100°C.

- The temperature dependence of fracture strength as measured in bending from room temperature to 1600°C.
- The dependence of fracture strength on the rate of loading in three-point bending at 1600°C with times to failure ranging from one second to five hours.

In the first of these three areas, slip cast and sintered tubes of SiC were tested at extremely high temperature in biaxial tension by locating the tubes in a graphite resistance furnace and pressurizing them with nitrogen. The resulting stress rupture data along with an analysis of the data have been written as an internal report which is included here as Appendix A. The data analysis employs the stress rupture theory of Charles, therefore another internal report describing the theory in more detail is included as Appendix B.

The second and third areas of time-temperature dependent strength listed above were performed on a common set of approximately 90 bend specimens which were prepared in a manner similar to that described in Section II. The bars were sintered in vacuum at a temperature of approximately 2080°C for 30 minutes, resulting in densities from 95 to 96 percent of theoretical and microstructures composed primarily of 3-5 μ m grains of β -SiC. The bars were carefully ground from the as-sintered cross-sectional dimensions of 0.167 x 0.167 in. to 0.150 x 0.150 in. with a slight chamfer on the edges. The bars were not refired before testing. All testing (including room temperature) was carried out in three-point bending on a one and one-half inch span using a carefully aligned fixed-pin test fixture fabricated from sintered SiC. An internally wound Pt-40% Rh tube furnace allowed testing in air at temperatures to 1600°C. The

furnace and fixtures were mounted in an Instron testing machine capable of crosshead speeds from 0.00002 to 20 in./min.

The temperature dependence of strength was studied by testing ten specimens at each of four temperatures from room temperature to 1600°C at a crosshead speed of 0.002 in./min. and a corresponding loading rate of approximately 17 kspi/min (115 MPa/min). The resulting strengths are plotted on Figure 21 as a function of temperature. Again, the data points represent the average strengths while the error bars include the 95 percent confidence limits on the averages. The strength appears to be independent of temperature at a stress of approximately 80 kpsi (550 MPa) from room temperature to about 1200°C and drops to approximately 70 kpsi (480 MPa) by 1600°C. Examination of the fracture surfaces indicated that the fracture origins were located at processing-related flaws in the microstructure rather than machining damage.

The loading rate dependence of fracture strength in sintered SiC was studied in air at 1600°C in order to estimate the parameters of crack velocity relationships such as Equations 26 and 29. Constant loading rate tests were chosen rather than constant stress tests for the majority of the present work because of experimental constraints of the testing apparatus. The testing procedure included: heating the furnace to 1600°C, raising the furnace and upper fixture to expose the lower testing fixture, positioning the specimen on the lower fixture, lowering the furnace and upper fixture into the testing position, equilibrating the temperature for 15 minutes, and loading at a constant crosshead speed until failure. Five crosshead speeds were chosen from 0.5 to 0.00005 in./min resulting in times to failure of one second to five hours. At least five specimens

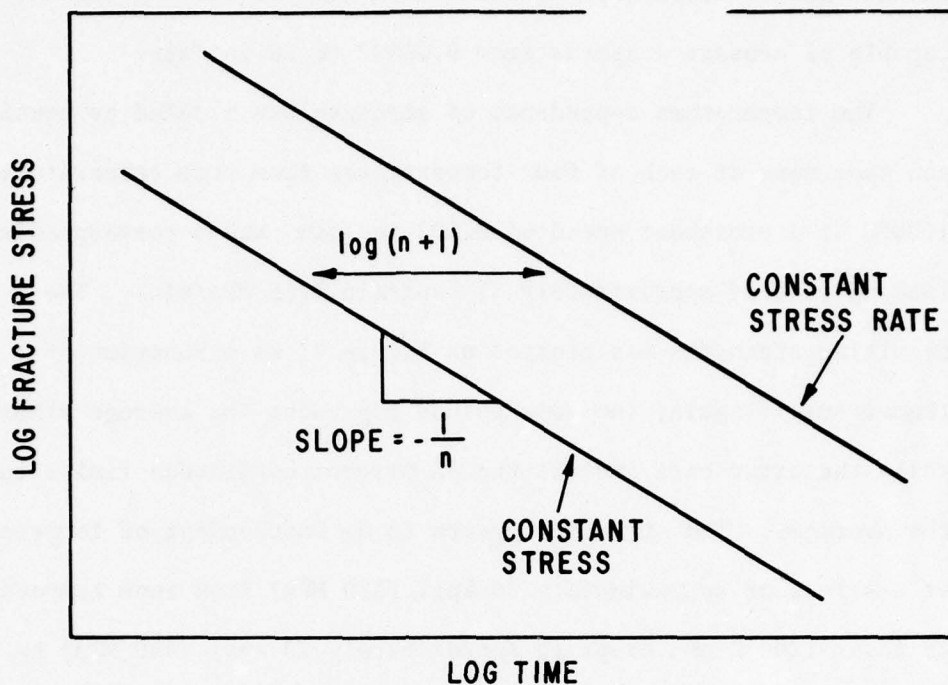


Figure 20. Schematic Drawing Showing Relationships of Strength Versus Time for Materials Which Behave According to Eq. 26

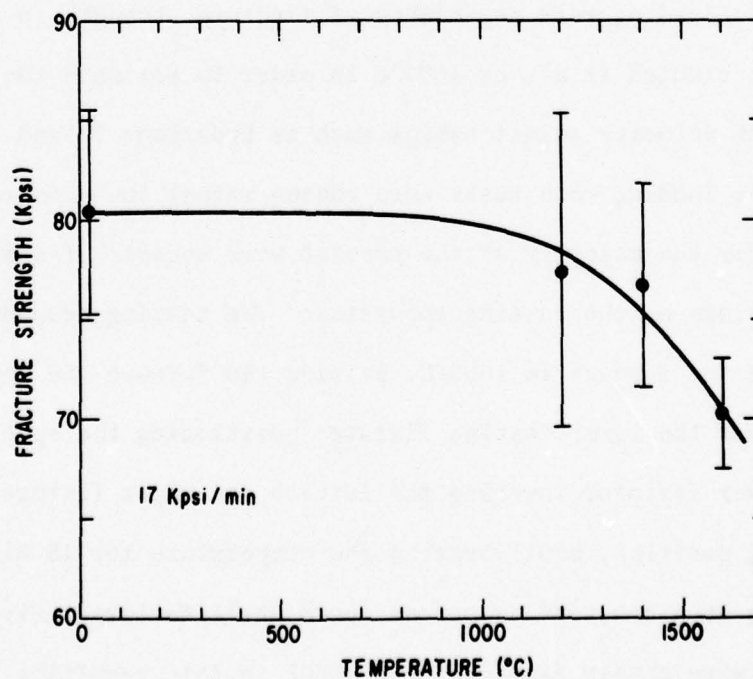


Figure 21. Fracture Strength as Measured in Three-Point Bending Versus Testing Temperature in Air

were tested at each loading rate. The results are included as the open circles on Figure 22 where log fracture strength is plotted as a function of log time to failure (same axes as Figure 20). The fastest loading rates resulted in an average strength of 82.5 kpsi (570 MPa) which is effectively the same as the room temperature strength included on Figure 21. As expected, slower loading rates and longer times to failure resulted in steadily decreasing fracture strengths. The data points fall on a smooth curve which is concave downward as predicted by Equation 29 instead of linear as predicted by Equation 26. Unfortunately, the rate of decrease in the slope of the curve as drawn on Figure 22 is greater than can be explained conveniently by Equation 29. Also, it was observed that the specimens tested at the slowest crosshead speed of 0.00005 in./min. were covered with a thick layer of spalling oxide which contained metallic inclusions. The metallic inclusions were identified by X-ray diffraction as a Pt-Rh alloy which had probably evaporated from the internal windings of the furnace and condensed on the cooler specimen (similar metallic particles also covered those regions of the test fixtures located in the hot zone).

Testing continued with six constant stress tests at the average failure stress of the 0.00005 in./min. specimens (45.8 kpsi - 315 MPa). These results are included on Figure 22 as the single square data point with the horizontal error bar. The average time to failure was surprisingly long at approximately 75 percent of the constant loading rate tests. Relationships such as Equations 26 and 29 predict that the time to failure in constant stress should fall between 2 and 10 percent of the time to failure in constant loading rate. Again, the

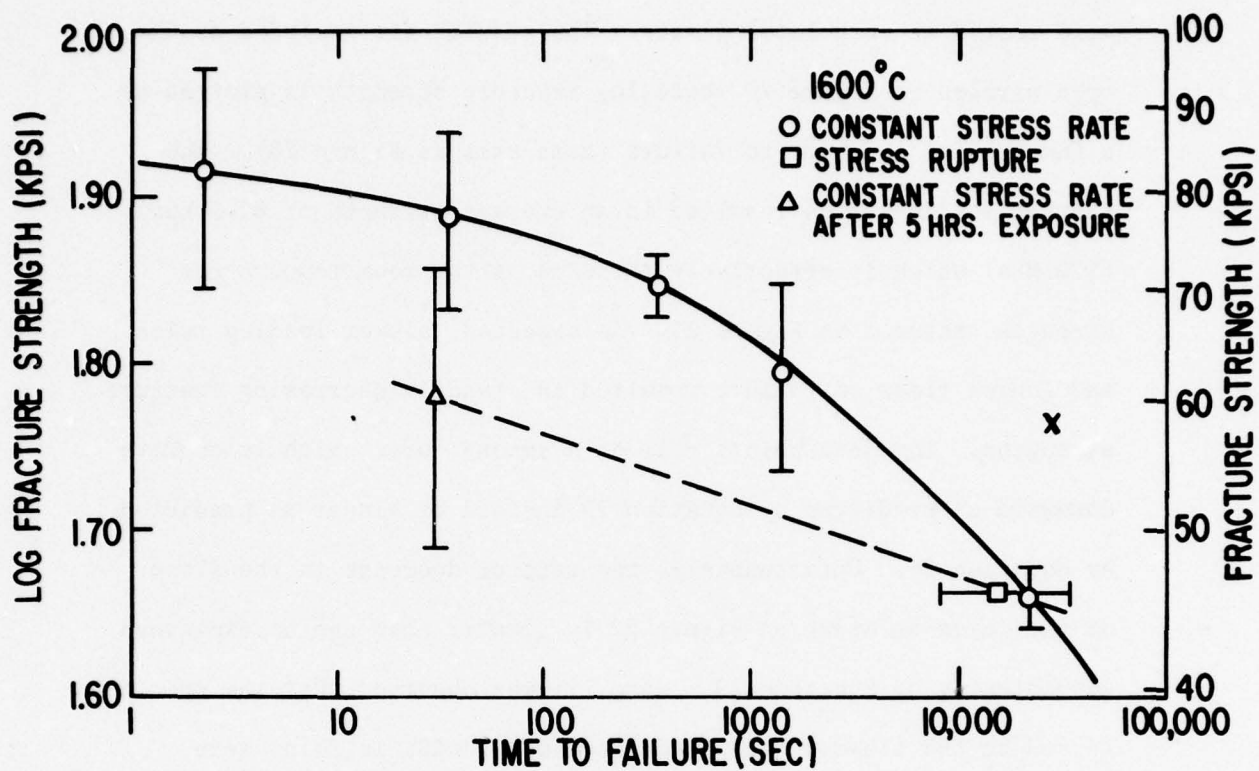


Figure 22. Constant Stress Rate and Stress Rupture Data Measured in Bending at 1600°C

specimen surfaces were severely oxidized.

The oxidation observed in four to five hours at 1600°C in the Pt-40% Rh furnace is considerably more severe than similar times and temperatures in other furnaces. This aggravated oxidation and spalling may be the result of contamination of the protective SiO_2 layer with a platinum silicide of some type or with Al_2O_3 from the fibrous insulation used on the ends of the furnace. In any case, the oxidation degraded the specimen surfaces sufficiently to suggest that oxidation contributed to the strength degradation of all specimens tested at long times to failure. To test this hypothesis, a set of five specimens were tested at a crosshead speed of 0.020 in./min. in a similar manner to the earlier group tested at the same loading rate. In this case, however, the specimens were allowed to soak in the furnace for five hours before loading. The results are plotted on Figure 22 as the single triangular data point. The average strength dropped from 77.3 kpsi (530 MPa) to 60.3 kpsi (415 MPa) due to the additional five hours of exposure in the furnace.

The data discussed above confirm that two mechanisms are active in decreasing the high temperature fracture strength with increasing testing time. The first is a mechanism of subcritical crack growth and the second is a surface degradation due to oxidation. It is difficult to separate the two mechanisms with the data available, but two related attempts can be made to salvage some information concerning subcritical crack growth. First, the dashed straight line of Figure 22 connects two constant loading rate data points which had similar histories of approximately five hours in the furnace at 1600°C prior to failure. From Equation 26, the slope of this line yields an estimate of the exponent, n , of approximately 25. The second method is somewhat less

straightforward. An additional five hours of furnace exposure prior to failure at a crosshead speed of 0.020 in./min. decreased the average strength by approximately 22 percent. Conversely, the hypothetical case of testing at 0.00005 in./min. without the five hours of furnace exposure during the test should increase the strength by a comparable amount. The "X" included on Figure 22 represents this hypothetical data point which was tested at 0.00005 in./min. and had a time to failure of approximately five hours but was located in the testing furnace for only 20 to 30 minutes. This is the approximate time of furnace exposure for the remaining four similar data points on Figure 22 (with the exception of the 0.0005 in./min. specimens which were in the furnace for approximately 45 minutes). A least-squares straight line through these five points (not drawn on Figure 22) yields an exponent, n , of approximately 28. Both of these estimates are reasonably consistent with earlier measurements² of 33.

Table 1 includes all of the average strengths, standard deviations, times to failure, etc. for the data reported on Figures 21 and 22.

In summary, the time-temperature dependence of fracture strength in boron-doped sintered SiC was measured in three-point bending. The strength was found to be independent of temperature from room temperature to approximately 1200°C and dropped to approximately 85 percent of the room temperature strength by 1600°C. The time dependence of strength at 1600°C was studied with constant loading rate tests. In addition to subcritical crack growth, a second mechanism of high temperature strength degradation was active and appeared to be related to oxidation. This second mechanism is believed to be characteristic of the particular furnace used during this testing. Similar conditions

TABLE 1
RESULTS OF HIGH TEMPERATURE BEND
TESTING USING CONSTANT LOADING RATES

Temp. (°C)	Crosshead Speed (in./min.)	Avg. Time to Failure (sec.)	Avg. Strength (kpsi)	Std. Deviation (kpsi)	Number of Specimens
RT	0.010	50	80.4	7.3	10
1200	0.002	250	77.4	10.2	11
1400	0.002	270	76.7	7.2	10
1600	0.002	360	70.3	3.9	10
1600	0.500	1.2	82.5	17.4	10
1600	0.020	33.8	77.3	7.6	5
1600	0.0005	1510	62.5	6.5	5
1600	0.00005	22,000	45.8	2.9	10
1600*	----	16,800	45.8	---	6
1600 ⁺	0.020	30.2	60.3	9.3	5

* Constant stress

⁺ Loading began after five hours of soak in the testing apparatus

in other furnaces lead to markedly less surface degradation due to oxidation and spalling.

VIII. CREEP MEASUREMENTS

Creep of boron-doped silicon carbide was studied previously on hot-pressed specimens where strain rates were measured in three-point bending near 1600°C in air at a stress of 25 kpsi.¹⁹ Creep rates were measured between 1.5×10^{-9} and 1×10^{-8} /sec. with stress exponents between 1.2 and 1.6. Subsequent measurements of fine-grained sintered SiC of about 95 percent theoretical density yielded no steady-state creep rate even after 150 hours at 1550°C. Because of this uncertainty the results were not reported.

The closed-end-tube specimen geometry adopted for stress-rupture tests described in Appendix A offers the possibility of creep measurements under those conditions that cause measurable strain (change in diameter of the tube) before rupture. This was not the case with the specimens used for the rupture tests described in Appendix A where the tubes were sintered at 2150°C, were coarse grained, and showed less than 0.010 in. of radial deformation after exposure to an internal pressure of 1350 psi (9.3 MPa) at 2100°C for 45 minutes. Therefore another set of tubes was slip cast and sintered at 2080°C for 40 minutes in vacuum. This temperature was selected as the lowest at which helium tight tubes were reliably obtained. Although a high degree of β to α transformation occurred, a fairly uniform microstructure with no "feathers" resulted as shown in Figure 23.

For creep measurements the tubes were bonded with epoxy into the pressure head, proof-tested with a gas pressure of 2200 psi (15.2 MPa) at room temperature and inserted into the furnace. The tubes were positioned in the furnace so that the hottest region was about 0.8 in. from the closed end. This established a 50°C difference

between the temperature of the hot zone and the temperature measured at the closed end and decreased the possibility of any end effects in the measurement of strain. Temperature was measured as described in Appendix A using a Leeds and Northrup optical pyrometer which was calibrated at the melting point of sapphire in argon in the same furnace. The surface carbon (from sintering in vacuum) was oxidized from each specimen with a torch and the surface was lightly sanded with 600 grit abrasive paper. On each run the tube was inserted into the furnace, brought to temperature in about 10 minutes, equilibrated for another 10 minutes, and pressurized with nitrogen to 1200 psi (8.3 MPa) for the desired time interval (15 to 30 minutes). After depressurizing the tube, the furnace was cooled, the tube was removed and its diameter at the hot zone was measured with a dial gauge to within 0.0001 in. The tube was slowly rotated through 360 degrees in a V-block and readings were taken at the largest and smallest diameter. The resulting four readings were averaged.

After collecting sufficient data, a 2.5 in. portion of the exposed end of the tube was removed and cut longitudinally into two halves. One half was polished and etched for metallography while the other was sliced into 1/4 inch long segments which were evaluated by liquid displacement for a density profile.

Three specimens have been tested to date, all at 1200 psi (8.3 MPa) internal nitrogen pressure with an external atmosphere of nitrogen at ambient pressure. The results, in terms of change in diameter and strain are included in Table 2. Table 3 includes initial dimensions, wall thicknesses, and wall stresses of the specimens. The results are also plotted on Figure 24 as strain versus time.

Specimen No. 1 was tested at 2010°C (curve 1, Figure 24).

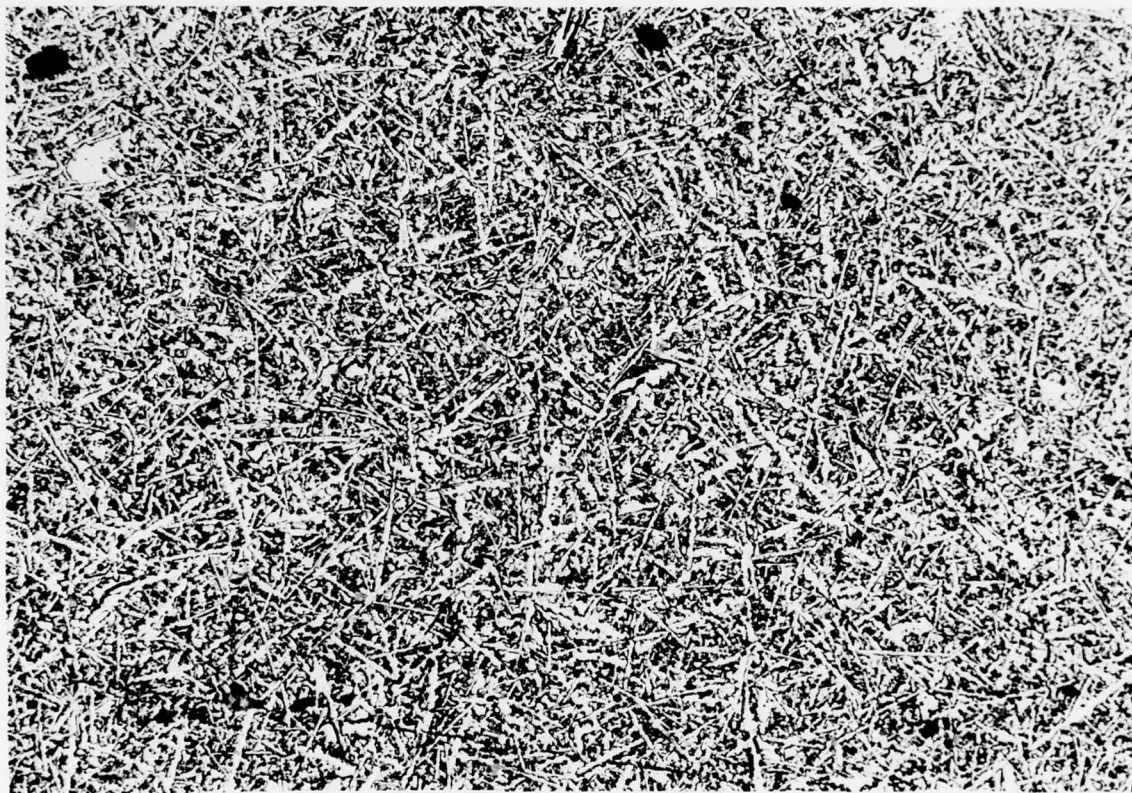


Figure 23. As-Sintered Microstructure of Slip Cast Tubes Used for Creep Measurements. 325X, molten salt etch.

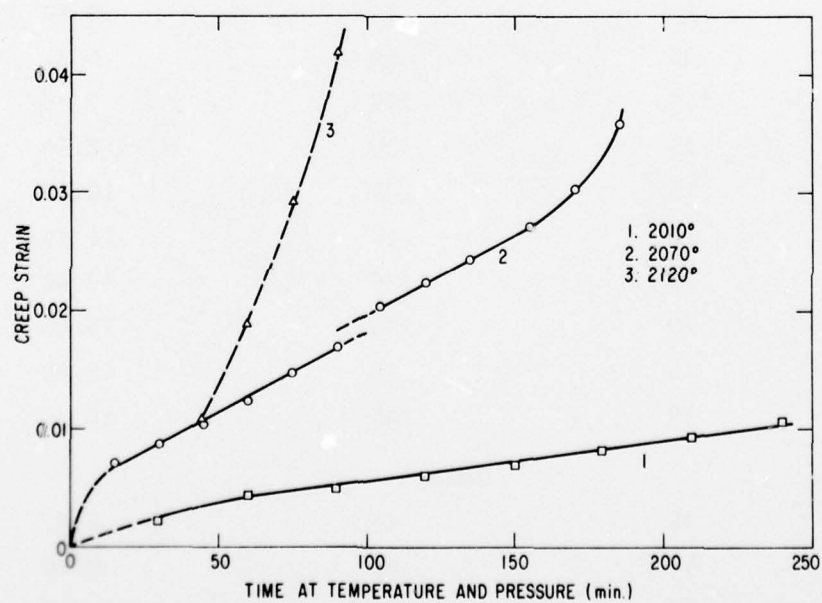


Figure 24. Creep Strain Versus Time for Pressurized Tubes at Three Different Temperatures

TABLE 2
SUMMARY OF CREEP EXPERIMENTS

Exp. #	Temp. (°C)	Time at Temp. and Press. (Min.)	Cumulative Time (Min.)	Change in Dia. (in. x 10 ³)	Strain
TUBE 1					
1	2010	30	30	1.5	.0024
2	2010	30	60	2.2	.0043
3	2010	30	90	2.6	.0050
4	2010	30	120	3.15	.0061
5	2010	30	150	3.65	.0070
6	2010	30	180	4.25	.0082
7	2010	30	210	4.85	.0094
8	2010	30	240	5.55	.0107
9	2170	30	---	----	-----
10	2070	30	270	5.55	.0107
11	2120	30	300	5.75	.0111
12	2120	30	330	6.00	.0115
13	2120	30	360	6.15	.0117
TUBE 2					
14	2070	15	15	3.65	.0072
15	2070	15	30	4.35	.0087
16	2070	15	45	5.10	.0103
17	2070	15	60	6.35	.0126
18	2070	15	75	7.75	.0148
19	2070	15	90	8.54	.0169
20	2070+	15	105	10.43	.0205
21	2070	15	120	11.50	.0226
22	2070	15	135	12.40	.0243
23	2070	20	155	13.85	.0272
24	2070	15	170	15.80	.0306
25	2070	15	185	18.40	.0359
TUBE 3					
26	2070	45	45	5.82	.0113
27	2120	15	60	9.80	.0190
28	2120	15	75	14.95	.0295
29	2120	15	90	21.65	.0419

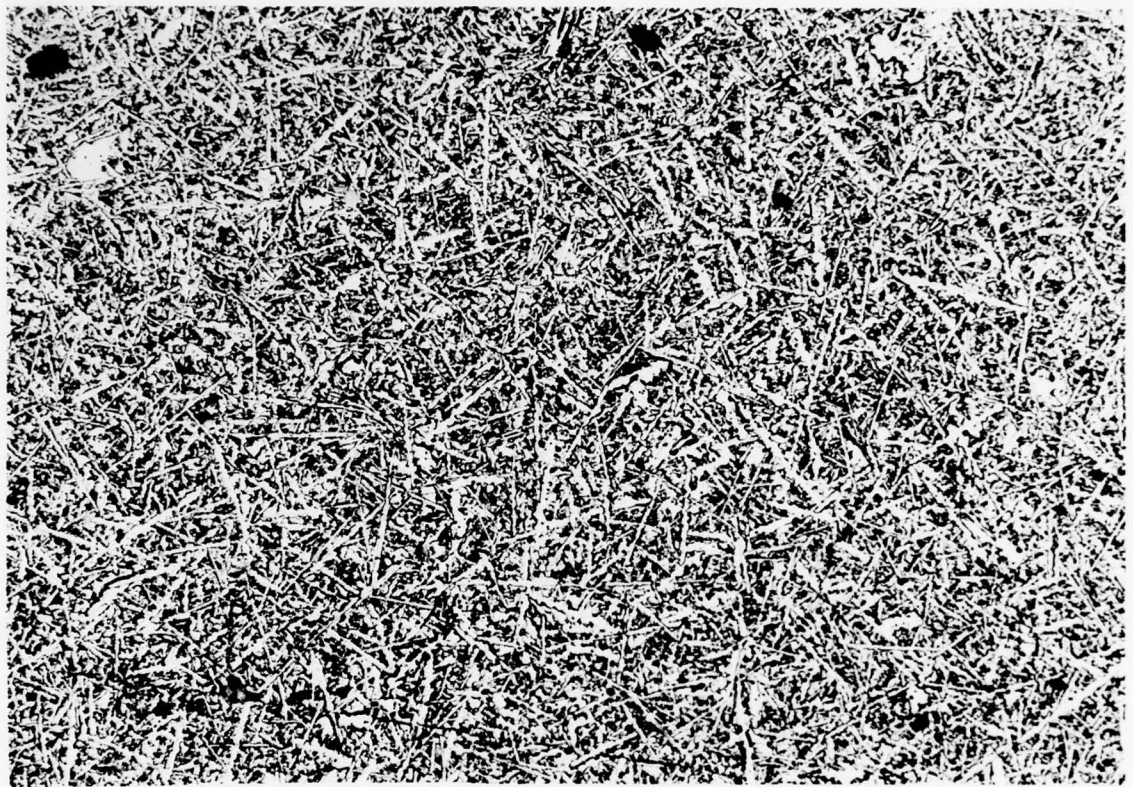


Figure 23. As-Sintered Microstructure of Slip Cast Tubes Used for Creep Measurements. 325X, molten salt etch.

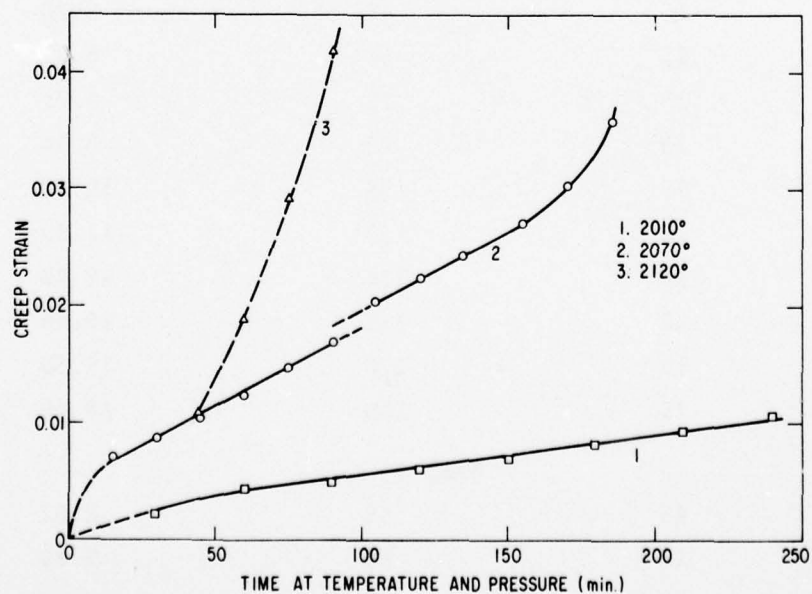


Figure 24. Creep Strain Versus Time for Pressurized Tubes at Three Different Temperatures

TABLE 3
SUMMARY OF CREEP EXPERIMENTS

	O.D. (in.)	I.D. (in.)	Effective Tube Diameter (in.)	Wall Thickness (in.)	Tangetial Stress at 1200 psi gas pressure
Tube No. 1:	0.515	0.403	0.459	0.056	4920
Tube No. 2:	0.516	0.400	0.458	0.058	4740
Tube No. 3:	0.515	0.393	0.454	0.061	4460

After an initial 60 minute period of primary creep (decreasing creep rate), the data points seem to fall on a straight line which yields a steady-state creep rate of $0.36 \times 10^{-4}/\text{min.}$ ($1 \times 10^{-8}/\text{sec.}$). After 4 hours of exposure at 2010°C the tube was heated in argon (not pressurized) to 2170°C for 30 minutes to bring about substantial grain growth. During this exposure some evaporation of the outer surface took place so that the diameter actually decreased by 0.005 in. This change in diameter has been taken into account in data points 10-13 of Table 2. The tube was then pressurized at 2070°C for 30 minutes with no detectable deformation. The temperature was increased to 2120°C where some creep could be detected. It was realized, however, that these very slow creep rates would be affected by simultaneous evaporation, thus the experiment was discontinued. The microstructure of this specimen sectioned in the hot zone is shown in Figure 25. Comparison with the initial microstructure of Figure 23 suggests a strong grain size dependence of creep rate in boron-doped SiC.

Specimen 2 was tested at 2070°C in 15 minute intervals for 3 hours. Curve 2 on Figure 24 shows the strain versus time behavior and indicates steady-state creep after only 15 minutes of testing. During the seventh 15 minute pressurization the temperature accidentally increased about 25°C for a short but unknown period of time which resulted in accelerated creep and a discontinuity in the linear behavior as plotted on Figure 24. At about 3 percent strain (160 minutes total exposure) the strain rate began increasing, thus indicating the onset of tertiary creep. From the linear segment of curve 2 one obtains a steady-state creep rate at 2070°C of $1.38 \times 10^{-4}/\text{min.}$ ($3.83 \times 10^{-8}/\text{sec.}$). After termination of the experiment,

the tube was sectioned, polished and etched for optical microscopy and evaluation of density. Figure 26 shows an etched section of the tube exposed to the highest temperature. No obvious grain growth occurred (compare with Figure 23) as a result of the testing. The longitudinal density profile is shown on Figure 27 as porosity versus distance from the end of the specimen showing a one percent increase in porosity due to the deformation of the hot zone section.

Specimen 3 was first exposed for 45 minutes at 2070°C. Only the final strain was recorded over this period but was consistent with data from Specimen 2. The specimen was then exposed for three 15 minute periods at 2120°C. Creep was rapid and resulted in 4.2 percent of strain after 45 minutes at which point the experiment was terminated. Determination of a steady-state creep rate from these measurements would be uncertain and has not been attempted. The data are plotted on curve 3 of Figure 24. Grain growth did not occur but an increase in pore size can be seen on as-polished sections in Figures 28a and b (before and after testing, respectively) and also on the etched section of Figure 29. Evaluation of density as a function of position revealed an increase in porosity in the hot zone of about two percent as shown on Figure 27.

The measurement of creep on closed-end tube specimens at very high temperature has the advantage that it eliminates the uncertainties related to the rigidity of the loading train and specimen grips usually encountered in other techniques. In addition the resulting tensile stress is effectively constant therefore allowing estimates of stress and strain without the knowledge of the stress exponent. Assuming a uniform maximum tensile stress of $\sigma_t = Pd/2t$ in the tube wall due to internal pressure, P , and diffusional creep (stress exponent = 1), one can calculate the activation energy, ΔH , for

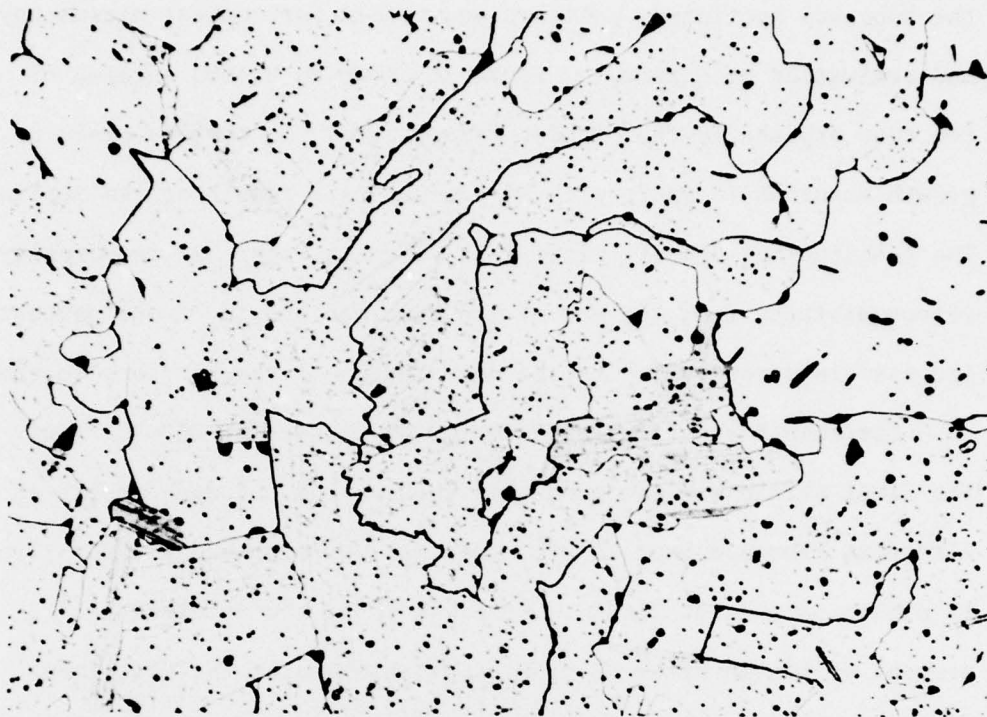


Figure 25. Microstructure of Creep Specimen No. 1 after Annealing at 2170°C for 30 minutes. 225X, molten salt etch.

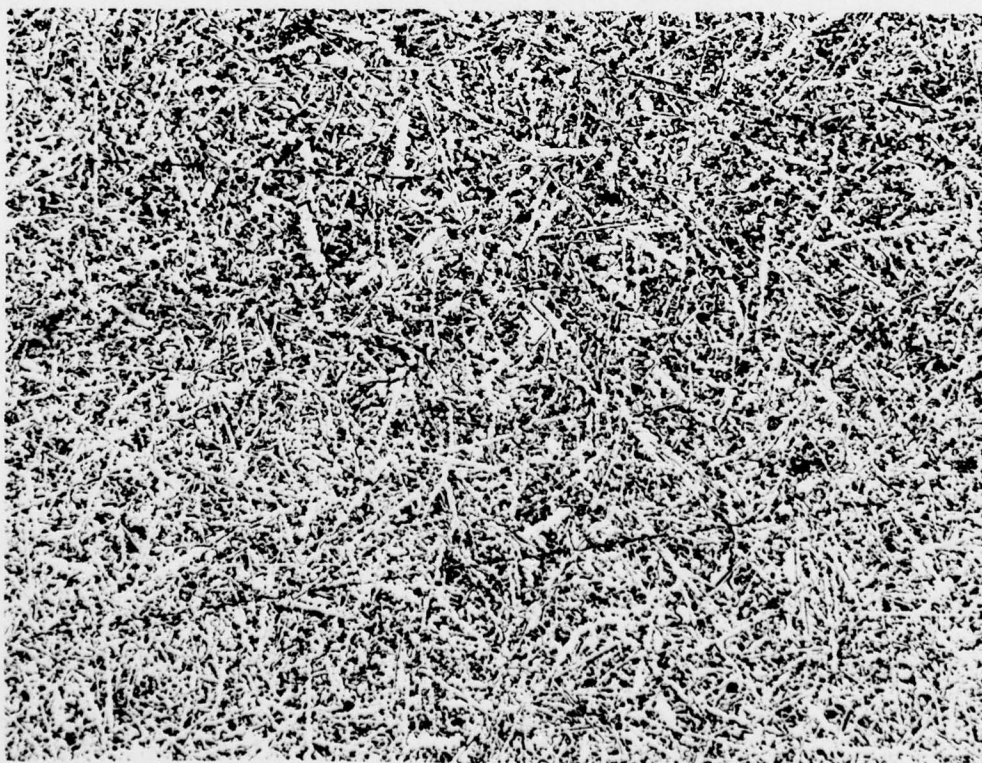


Figure 26. Microstructure of Creep Specimen No. 2 After Testing for 160 Minutes at 2700°C. 325X molten salt etch.

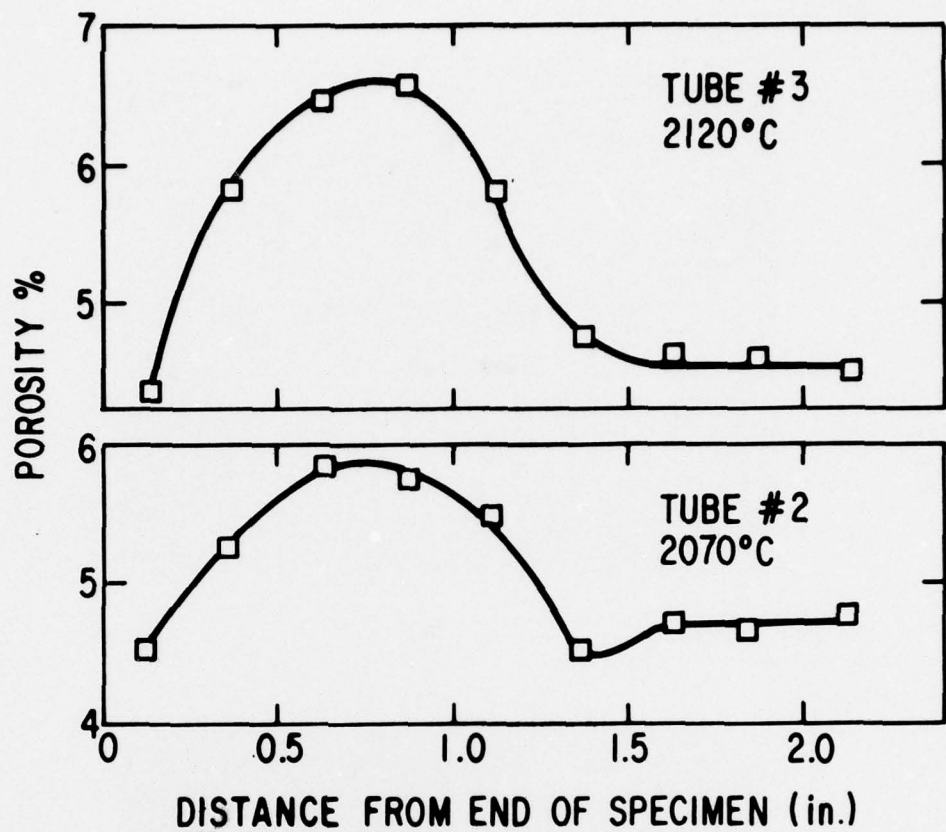
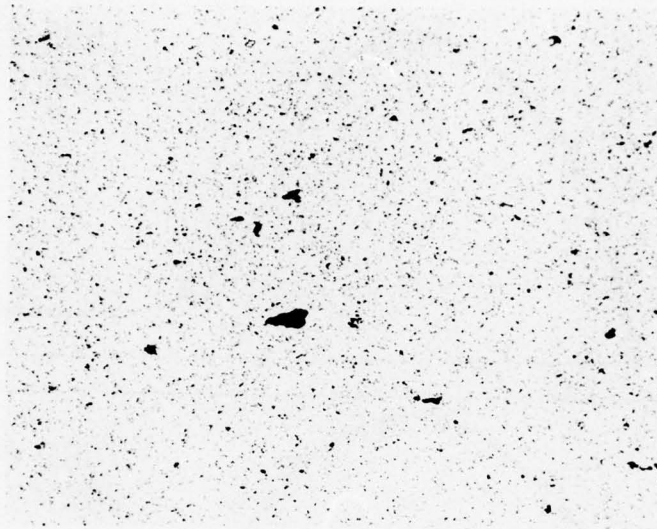
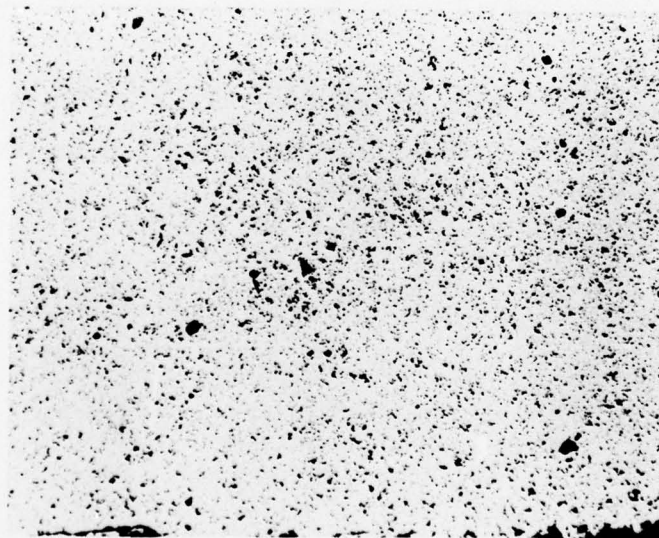


Figure 27. Density After Testing Versus Distance from the End of the Tube for Two Creep Specimens



(a)



(b)

Figure 28. As-Polished Sections at the Hot Zone of Specimen No. 3 Illustrating the Increase in Porosity from Before (a) to After Testing (b). 210X

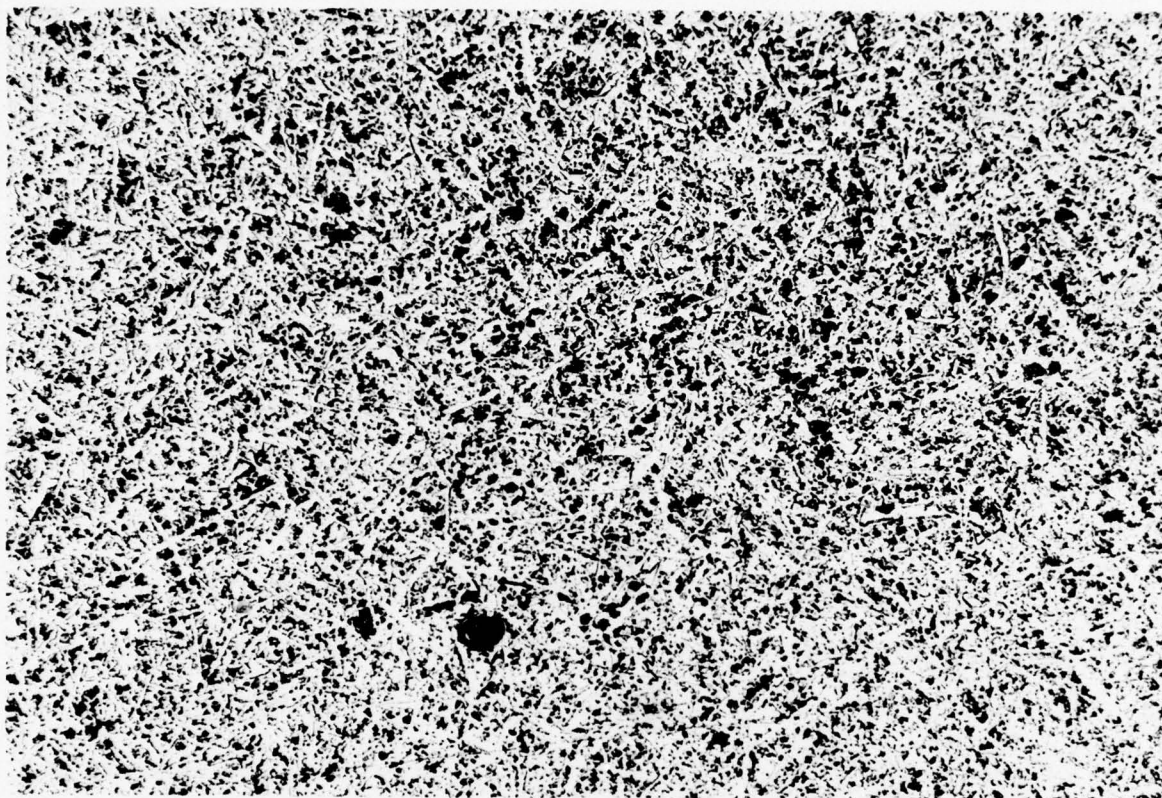


Figure 29. Polished and Etched Section Corresponding to Figure 28b. 325X, molten salt etch.

the rate controlling process as follows:

$$\log \frac{\dot{\epsilon}_1}{\dot{\epsilon}_2} \frac{\sigma_2}{\sigma_1} = \frac{\Delta H}{2.3R} \left(\frac{1}{T_1} - \frac{1}{T_2} \right) \quad (30)$$

Substituting the stresses, steady-state strain rates and test temperatures for Specimens 1 and 2 results in a calculated ΔH of 246 Kcal/mole. This may be compared to activation energies of 165 to 210 Kcal/mole reported previously from creep data of hot-pressed SiC in bending near 1600°C.¹⁹ The highest activation energies of this earlier study were measured on a chemical composition very similar to the sintered SiC used in the present pressurized tube experiments.

It is customary to calculate apparent diffusion coefficients from creep data and compare the results with diffusion coefficients obtained by other techniques, particularly by tracer diffusion. The calculation of D_{app} from creep data, however, requires information on grain size. In Herring's treatment,²⁰ creep in a polycrystalline solid is modelled by the flow of lattice defects which are motivated by chemical potential gradients in the grains. The grain size enters as a squared relationship for the model of a uniform, equiaxed grain structure. Raj and Ashby have discussed creep in model structures composed of elongated grains.²¹ Their solution for the strain rate of high aspect ratio grain structures (Equation 26, Reference 21) reduces to an expression very similar to that of Herring if diffusion is limited to volume diffusion and grain size is replaced by particle length.

The grain structures of the present SiC creep specimens are composed of thin interpenetrating randomly oriented plates with a wide distribution of sizes. If we model such a structure as an

assembly of discs of constant diameter to thickness ratio we may obtain, according to Fullman,²² the average diameter, \bar{d} , of the discs from measurements of the mean linear intercept and the area count in a section. This quantity was selected as the characteristic dimension for estimation of D_{app} . For thin plates Fullman derived:

$$\bar{d} = \frac{2N_L}{N_S} \quad (31)$$

Where N_L is the number of particles per unit length of a section and N_S is the number of particles per unit area. This yielded $\bar{d} = 14.6\mu\text{m}$ for the sintered tubes of SiC. D_{app} can then be calculated as follows:

$$D_{app} = \frac{0.075 \dot{\epsilon} k T \bar{d}^2}{\sigma_t \Omega} \quad (32)$$

where Ω , the molar volume of defects, is $6.23 \text{ cm}^3/\text{mole}$. The resulting values of D_{app} are $3.73 \times 10^{-11} \text{ cm}^2/\text{sec}$. at 2343°K and $9.02 \times 10^{-12} \text{ cm}^2/\text{sec}$ at 2283°K . This data is plotted on Figure 30 along with previous values of D calculated from creep measurements for hot-pressed boron-doped material, R-81 (Ref. 19, p. 26). A linear regression analysis of the resulting five data points yielded:

$$D_{app} = 3.25 \times 10^{10} \exp [-(225 \pm 29)/RT] \quad (33)$$

where the uncertainty in activation energy represents the 95 percent confidence limits on the slope of Figure 30 as calculated using Student's t-distribution.

In addition to the creep data, carbon diffusion data from single crystals of n and p-type α -SiC according to Ghoshtagore and Coble²³ have been included on Figure 30. It is pertinent to emphasize that no a priori agreement between the two curves is necessary, however, since different rate controlling mechanisms may be active in creep and tracer diffusion.

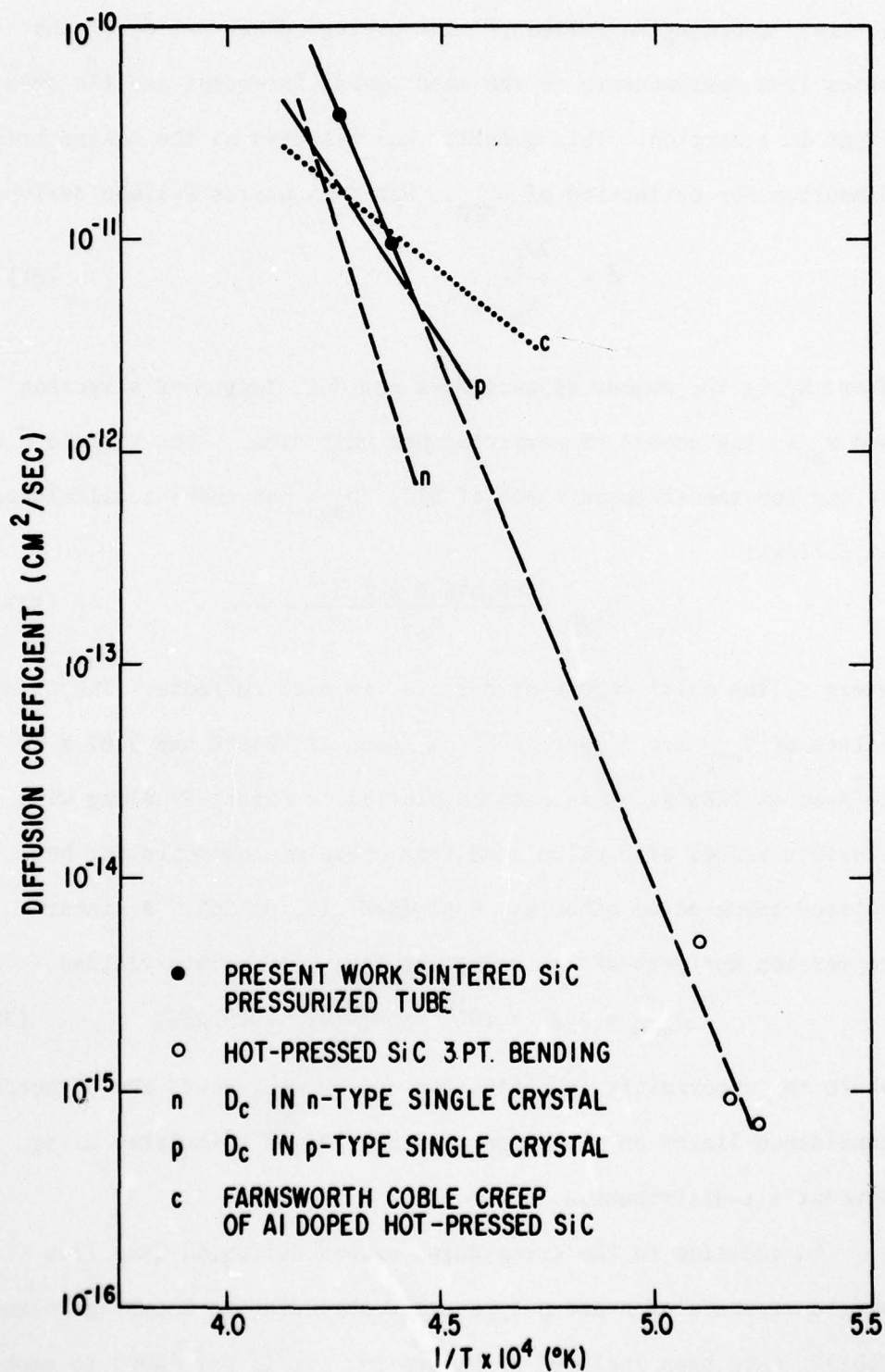


Figure 30. Diffusion Coefficients Versus Reciprocal Temperature Including Both Data Calculated from Creep Measurements and Direct Measurements of Diffusion from the Literature

Inspection of the pore structure in the sectioned SiC specimens before and after creep (Figure 28a and b) does not reveal grain boundary separation as was clearly observed, for instance, in creep of pure polycrystalline alumina composed of equiaxed grains reported by Folweiler.²⁴ Such grain boundary separation is in general attributed to a substantial contribution of non-accommodated grain boundary sliding. In the present case the change in pore morphology accompanying the creep of SiC appears to be resulting from uniform pore growth. Whether this difference in morphology of the growing pores results from the difference in grain shape or from a difference in creep mechanisms cannot be resolved from available information. It is believed, however, that this difference is substantial and may be particularly important with respect to the stress rupture behavior.

AD-A047 504

GENERAL ELECTRIC CORPORATE RESEARCH AND DEVELOPMENT --ETC F/G 11/2
INVESTIGATION OF CERAMICS FOR HIGH TEMPERATURE TURBINE COMPONENTS--ETC(U)
JUN 77 C A JOHNSON, S PROCHAZKA N62269-76-C-0243

UNCLASSIFIED

SRD-77-145

NADC-75228-30

NL

2 OF 2

ADA047504



END
DATE
FILMED

1 - 78

DDC

IX. ORIGIN OF STRENGTH LIMITING FLAWS

The optimum processing procedure for SiC powder presently includes screening through an 8 μm screen as a dispersion of powder in benzene, spraying into liquid nitrogen to freeze the benzene without segregation of the binder, and freeze drying to remove the benzene. Great care is taken in all steps after the screening to avoid contamination of the powder with dust, lint, etc., but despite all efforts, a large proportion of failures in material sintered from such powder originate at large irregular voids which are commonly 20-200 μm in length. Figure 31 is a scanning electron micrograph of a typical fracture origin in material which was sintered from fully processed powder.

The screening operation is believed to remove all foreign material and aggregates of SiC larger than approximately 10 μm , therefore only two plausible sources of the flaws remain.

- The powder is contaminated after the screening with large particles of foreign material which evaporate, decompose or dissolve during the sintering, thus leaving large unsinterable voids behind.
- Agglomerates of SiC (probably very weak ones) are formed at some stage after the screening and occasionally cause massive "bridging" during die-pressing. The large empty cavities or low density regions that are created have no chance of being closed by sintering and thus result in large voids and flaws.

During the previous year, progressively increasing care has been taken to avoid contamination of the powder with any foreign material



**Figure 31. Scanning Electron Micrographs
of a Typical Void at the Fracture
Origin of a Sintered Specimen.
500X**

after the screening step. These efforts do not appear to have decreased the frequency of occurrence of failure from large voids, thus suggesting that they are not caused by contamination.

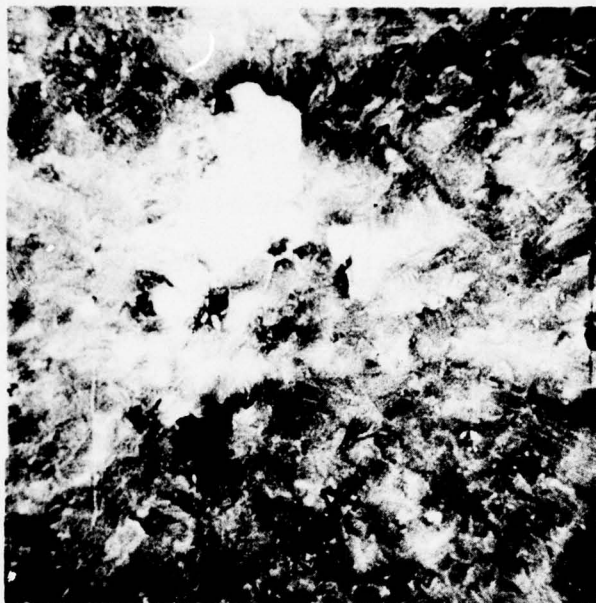
The design of an experiment to unambiguously identify the source of these flaws has proven to be very difficult. One experiment which yielded some information involved the hot-pressing of fully processed powder. It was reasoned that the large voids tending to form during sintering would be closed and fully densified during hot-pressing. If these potential voids were caused by contamination, the most likely candidates would be carbonaceous material such as lint, dust, etc. which would decompose at relatively low temperatures during sintering and, depending on composition, would leave remnants of carbon on the inner surfaces of the voids. During hot-pressing the foreign material would still decompose and yield carbon, but the resulting voids would tend to close due to the additional driving force for densification provided by the externally applied pressure. The remnant carbon, however, would be trapped as a lamellar layer with comparable dimensions (in two directions) to the original void, and would behave as a flaw of comparable severity to the original void. Therefore, if the flaws observed in sintered material are due to carbonaceous foreign material, then specimens from hot-pressed bodies should fail at flaws of comparable dimensions and at comparable strengths to the sintered material.

On the other hand, if the voids in sintered material are due to "bridging" of weak agglomerates during cold pressing, then hot-pressing of the same powder should close the voids and densify the structure with no evidence of the preexisting flaws. Failure should be caused by a different type of flaw which is less severe than the voids in the sintered material and the fracture strength should accordingly be higher.

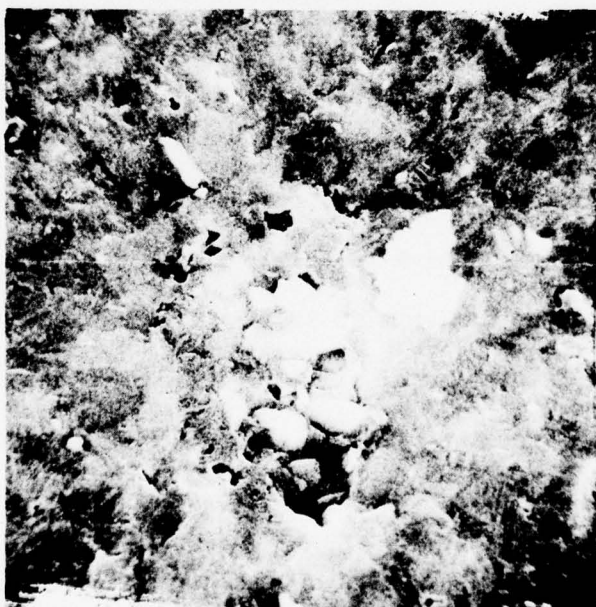
A charge of 85 grams of fully processed SiC powder was hot-pressed in a two in. diameter graphite die at 1850°C for 60 minutes at 10 kpsi (68.9 MPa) resulting in a final density of greater than 99.5 percent of theoretical. The billet was cut and ground into 12 bend specimens with dimensions of 0.150 x 0.150 x 1.75 in. with slightly chamfered edges. It was preferred, of course, that the eventual strength limiting flaws would not be caused by the machining, therefore great care was taken to minimize machining damage and the specimens were refired to reduce the severity of any flaws which may have been induced. All 12 specimens were refired at 1940°C for 40 minutes at a furnace pressure of 0.35 torr. The choice of these re-firing conditions was based both on the data presented in Section III and on microstructural data presented below.

The specimens were tested at room temperature in three-point bending on a one and one-half inch span resulting in an average strength of 117 kpsi (805 MPa), a standard deviation of 13.3 kpsi (91.7 MPa), and a Weibull modulus of 8.8. These can be compared to sintered, machined and refired specimens which generally yield an average strength of 80-100 kpsi, a standard deviation of 9-12 kpsi and a Weibull modulus of 6-10.

The fracture origins of all 12 specimens were located and studied by scanning electron microscopy. As hoped, failure was not predominated by machining flaws since only 4 of 12 specimens failed from origins on or near the surface. Each of the remaining specimens appeared to contain an inclusion at the fracture origin. Examples of these are included as scanning electron micrographs in Figures 32a and b. Energy dispersive X-ray analysis of several of these regions revealed high concentrations of titanium. It is interesting to note that the inclusions at all 8



(a)



(b)

Figure 32. Scanning Electron Micrographs of Two Typical Volume Flaws in Hot-Pressed SiC. 5000X

subsurface fracture origins measured approximately 5 to 15 μm . This is roughly an order of magnitude smaller than the voids commonly observed as fracture origins in sintered material (Figure 31) and is probably small enough to pass through the "nominal" 8 μm screen used in powder processing.

Although the results of this hot-pressing experiment are not conclusive, the following observations (combined with the reasoning discussed above) suggest that the source of voids in sintered material is not large particles of carbonaceous material:

- The average strength of hot-pressed material was 20 to 30 percent higher than that for sintered material.
- The fracture origins in hot-pressed material were approximately an order of magnitude smaller than those in sintered material.
- Several of the fracture origins of hot-pressed material have been identified as titanium-containing inclusions.

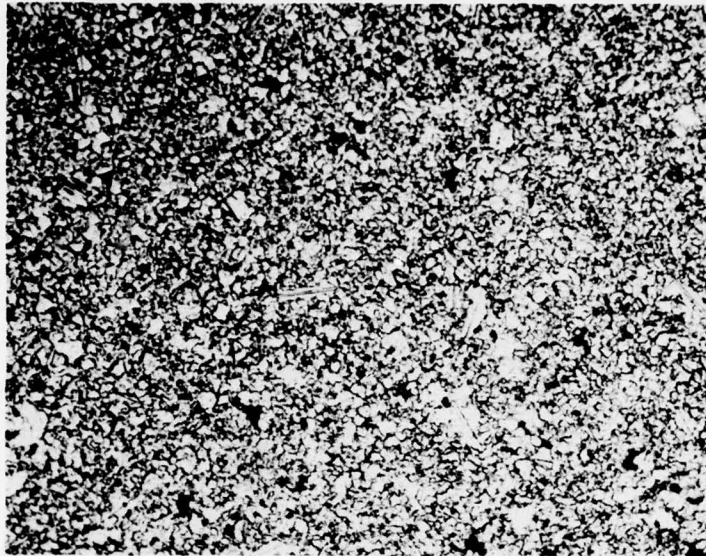
It is concluded that the most probable cause of the large voids during the sintering of SiC is massive bridging of agglomerates during the powder compaction step of specimen fabrication.

As mentioned above, the 12 hot-pressed specimens were refired at 1940°C for 40 minutes. The choice of a refiring temperature for these specimens required the consideration of a factor not normally required in the refiring of sintered and machined specimens. Since the hot-pressed material was consolidated at a maximum temperature of 1850°C, the grain size was much finer ($< 1 \mu\text{m}$ average) than that for material sintered at 2100°C (commonly 3-5 μm average). No information was available on the microstructural changes caused by annealing of such fine grain sizes in boron-doped, hot-pressed β -SiC, therefore some preliminary experiments

were carried out on scraps of the hot-pressed billet.

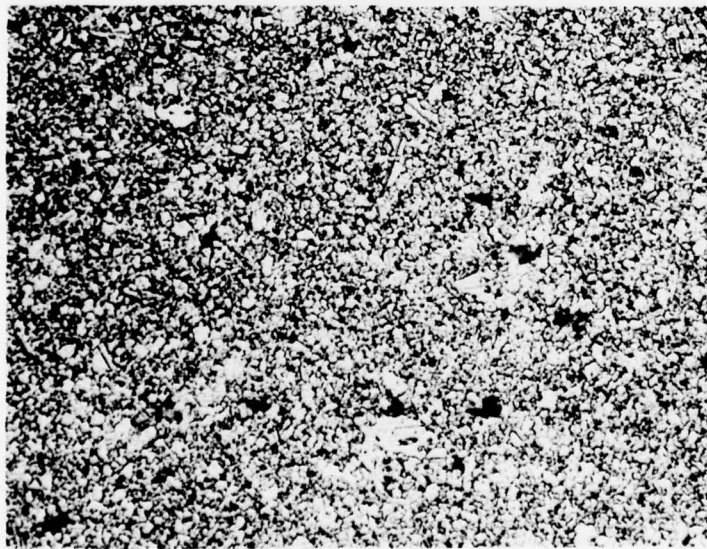
Small samples were annealed for 30 minutes at each of the following temperatures: 1735, 1825, 1920, 1965, 2015, 2055, and 2105°C. The annealed samples and one as-hot-pressed sample were polished and etched in both molten KOH + 10% KNO₃ for 60 seconds at approximately 450°C and boiling Murakami's reagent for five minutes. The samples annealed at 1735° and 1825°C revealed no detectable change in microstructure as might be expected with a hot-pressing temperature of 1850°C. Micrographs of the as-hot-pressed sample and the remaining annealed samples are included in Figures 33a-f in order of increasing annealing temperature. Coarsening of the microstructure is easily resolved at 1965°C (Figure 33c) and proceeds as a type of exaggerated grain growth where a few grains grow freely at the expense of the remaining fine-grained β -SiC matrix. The growing grains are relatively equiaxed and are primarily β -SiC as opposed to the exaggerated grains of α -SiC which can grow in sintered β microstructures.^{1,3} At 2055°C (Figure 7e) the fine-grained matrix has disappeared but the microstructure is still primarily β -SiC (approximately 5 percent 4H-SiC as determined by quantitative X-ray diffraction⁴). By 2105°C (Figure 7F), large portions have transformed into 100-500 μ m "feather" structures of α -SiC.¹ The area photographed in Figure 7f, however, is a region between "feathers" which remains primarily β -SiC.

The choice of 1940°C for the refiring of the hot-pressed bend specimens was based on both this microstructural study and the refiring data included in Section III and represents a compromise between a minimal change in microstructure (1940°C resulted in a microstructure between Figures 33b and c) and the less-than-optimum crack "blunting" treatment at 1940°C as illustrated earlier in Figure 2.



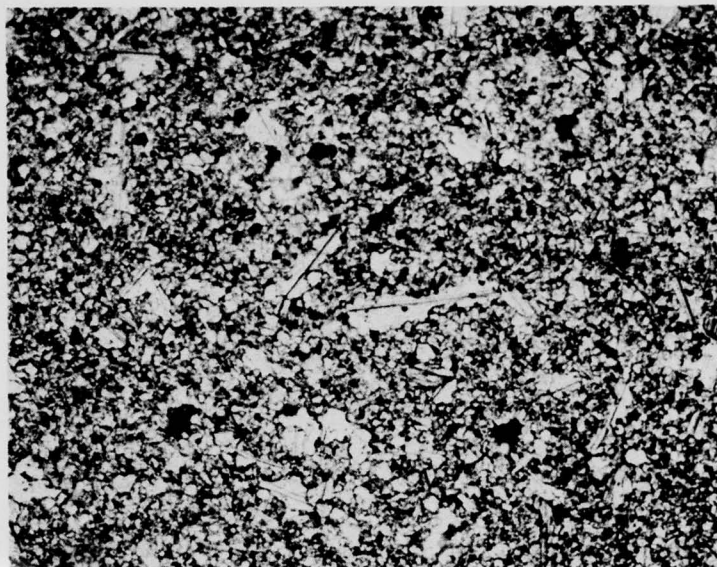
a. As Hot Pressed

Figure 33. Optical Micrographs of Polished and Etched Samples of Hot-Pressed SiC Annealed for 30 Minutes. 1250X, dual etch-molten salt and Murakami reagent.



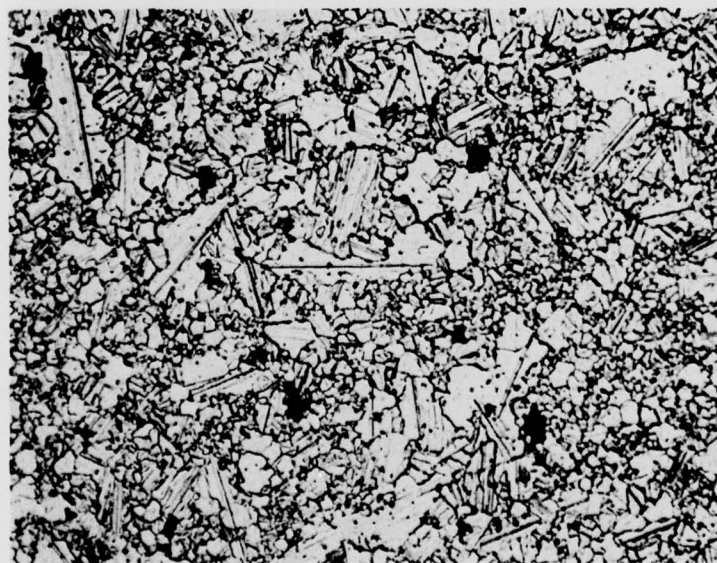
b. 1920°

Figure 33. (Cont'd)



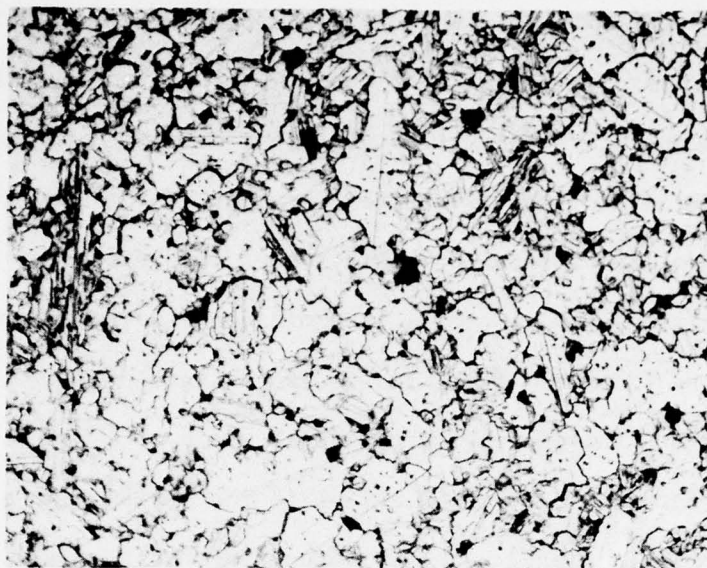
c. 1965°

Figure 33. (Cont'd)



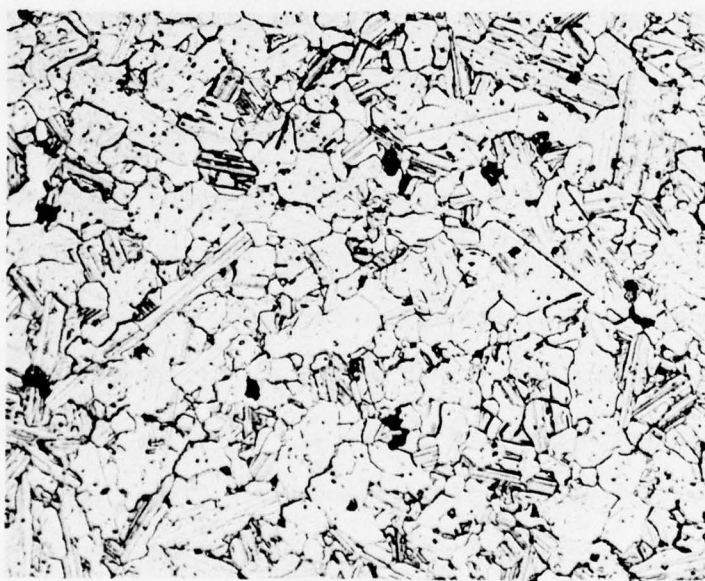
d. 2015°

Figure 33. (Cont'd)



e. 2055°

Figure 33. (Cont'd)



f. 2105°

Figure 33. (Cont'd)

As discussed in more detail in Reference 3, the combined molten salt and Murakami etches reveal useful detail of partially transformed microstructures that cannot be resolved by either etchant when used alone. Transformation of β to α commonly proceeds in sintered SiC as the growth of thin, tabular grains of α -SiC oriented with the basal plane of the crystallographic structure parallel to the plane of the tabular grains. Careful transmission electron microscopy by Shinozaki and Kinsman²⁵ first identified an envelope of epitaxially connected β -SiC surrounding each tabular grain of α -SiC with a (111) plane of the cubic structure parallel to the basal plane of the α -SiC and with a highly planar boundary connecting the two polytypes. As reported in Reference 3, the molten salt etch primarily reveals the irregular external boundary where the envelope of the β -SiC contacts the matrix of smaller β -SiC grains. The Murakami etch, on the other hand, primarily reveals the epitaxial boundary between the two polytypes. The combined etch of partially transformed sintered SiC therefore reveals both the planar α - β boundaries and the irregular β - β boundaries.

Similar features can be resolved in the microstructures of the hot-pressed and annealed specimens discussed above and included as Figures 33a-f. Throughout this series of micrographs, it is evident that each of the exaggerated grains of "primarily β -SiC" contains a thin layer with nearly planar boundaries. These are particularly obvious in Figures 33c and d but can be resolved even in the as-hot-pressed microstructure of Figure 33a. Selected area electron diffraction and X-ray diffraction have identified the planar layers as primarily 4H-SiC and the envelopes as 3C-SiC oriented in the manner discussed above. The shape of the resulting exaggerated grains in fine-grained hot-pressed SiC is closer to equiaxed (thicker layer of β -SiC envelope)

than that for the same degree of transformation in sintered SiC.³ This difference in shape is probably due to a greater driving force for propagation of the β - β boundaries when the matrix grains are less than 1 μm (hot-pressed) than when they are 3 to 5 μm (sintered). Despite the relatively small volume of α -SiC within each of the exaggerated grains, the rate of three-dimensional grain growth is probably controlled by the rate of lateral growth of the α -SiC layer. The microstructure of the hot-pressed SiC can therefore be strongly influenced by small amounts of β to α transformation. The total amount of transformation can be as little as two percent and result in a microstructure such as Figure 33c or as little as five percent and result in a microstructure such as Figure 33e.

X. INCREASING FRACTURE TOUGHNESS THROUGH THE ADDITION OF SECOND PHASES

Any method by which the fracture toughness or fracture energy of a ceramic can be increased without increasing the inherent flaw size will be beneficial with respect to several strength related properties including the fracture strength (through the Griffith relation) and resistance to impact damage (both Hertzian impact and machining damage). There has been a great deal of work reported in the literature with the goal of increasing the fracture toughness of ceramics through the addition of dispersions of second phase particles. This area has been reviewed in some detail recently by Donald and McMillan.²⁶ The actual role of second phase particles is very complex and depends on factors such as thermal expansion mismatch (between particles and matrix phases), elastic modulus mismatch, particle size, etc. Depending on the parameters listed above, the fracture toughness is generally hoped to increase through interactions of the crack front with the second phase particles,²⁷ with stress fields in the matrix surrounding the particles²⁸ or with regions of microcracks caused by the particles. The actual interactions may cause the crack to be arrested, branched or deflected with the desired net effect of an increase in the energy needed for a unit of crack propagation.

During the previous year, several preliminary experiments were directed toward the study of particulate second phase additions in boron-doped sintered SiC. The eventual goal of these experiments is a practical means of increasing the fracture toughness of sintered SiC with negligible degradation of other important properties such as creep, stress rupture and oxidation. In order to accomplish this goal, several criteria must be satisfied in addition to those

which directly affect the fracture toughness. The additional criteria relate to the compatibility of the second phase particles with the matrix SiC. The second phase additive:

- must not inhibit the sinterability of boron-doped SiC powder through either chemical or physical mechanisms,
- must exist in the sintered microstructure as isolated second phase particles rather than a continuous grain boundary phase (which may degrade creep and stress rupture properties),
- must not adversely affect the protective nature of the silica layer through chemical "fluxing", spalling, etc.

Several promising second phase systems were identified for this preliminary study including boron carbide and transition metal diborides with volatile oxides such as MoB_2 and WB_2 . The physical and chemical properties of these materials combined with our present understanding of the sintering process in boron-doped SiC suggested that they had the potential of meeting the compatibility criteria listed above. The additives were generally in the form of 1 to 3 μm particles and were ball milled with the SiC powder for 4 to 6 hours to provide intimate mixing. The resulting microstructures generally revealed the second phase particles as isolated inclusions with approximately the same distribution of sizes as that present in the starting powder. It was also generally observed that larger amounts of additive enhanced the β to α polytype transformation.

To date, the majority of work on second phase additives in SiC has been aimed at studies of sinterability using approximately 0.5 in. diameter pellets. The only measurements of fracture toughness

were carried out on two groups of double torsion specimens containing approximately 0.5 and 5.0 w/o of boron carbide respectively. The measurements of K_{IC} at room temperature revealed no distinguishable difference for the two levels of additive with all K_{IC} values in the vicinity of 2.7 Kpsi $\sqrt{\text{in.}}$

REFERENCES

1. S. Prochazka, R. A. Giddings, C. A. Johnson, "Investigation of Ceramics for High-Temperature Turbine Vanes," Final Report, Contract N62269-74-C-0255, G.E. Report No. SRD-74-123, Nov. 1974.
2. S. Prochazka, C. A. Johnson, R. A. Giddings, "Investigation of Ceramics for High-Temperature Turbine Components," Final Report, Contract N62269-75-C-0122, G.E. Report No. SRD-75-126, Dec. 1975.
3. C. A. Johnson and S. Prochazka, "Microstructures of Sintered SiC," in Ceramic Microstructures '76, Ed. by R.M. Fulrath and J. A. Pask, 1977.
4. S. F. Bartram, "Quantitative Analysis of SiC Polytypes by X-ray Diffraction," G.E. Tech. Report 75CRD022, 1975.
5. C. D. Greskovich, J. H. Rosolowski and S. Prochazka, "Ceramic Sintering," Final Tech. Report, Contract N00014-74-C-0331, G.E. Report SRD-75-084, July 1975.
6. A. F. McLean, E. A. Fisher, R. J. Bratton and D. G. Miller, "Brittle Materials Design, High-Temperature Gas Turbine," AMMRC-CTR-75-28, Interim Report, Oct. 1975.
7. K. M. Johansen and R. E. Wallace, "Ceramic Gas Turbine Engine Demonstration Program," Contract No. N00024-76-C-5352, Interim Report, June 1976.
8. F. F. Lange, "Healing of Surface Cracks by Oxidation," J. Am. Ceram. Soc., 52, 290 (1970).
9. W. Weibull, "A Statistical Distribution Function of Wide Applicability," J. Appl. Mech., 18, 293 (1951).
10. D. M. Kotchick, R. C. Hink and R. E. Tressler, "Gauge Length and Surface Damage Effects on the Strength Distributions of Silicon Carbide and Sapphire Filaments," J. Comp. Matl., 9, 327 (1975).
11. G. K. Bansal, W. H. Duckworth and D. E. Niesz, "Strength-Size Relationships in Ceramic Materials," Final Report, Contract N00014-73-C-0408, NR 032-541, Oct. 1975.

12. G. K. Bansal, W. H. Duckworth, D. E. Niesz, "Strength-Size Relations in Ceramic Materials: Investigation of an Alumina Ceramic," J. Am. Ceram. Soc., 59 [11-12] 472 (1976).
13. R. J. Charles, "Static Fatigue of Glass -II," J.A.P., 29, 1554 (1958).
14. S. M. Wiederhorn, "Subcritical Crack Growth in Ceramics," p 613 in Fracture Mechanics of Ceramics, Ed. by R. C. Bradt, D. P. H. Hasselman and F. F. Lange, Plenum Press, NY, 1974.
15. G. G. Trantina and C. A. Johnson, "Subcritical Crack Growth in Boron-Doped SiC," J. Am. Ceram. Soc., 58, 344 (1975).
16. R. J. Charles, "Diffusion Controlled Stress Rupture of Polycrystalline Materials," Met. Trans. 7A, 1081 (1976).
17. R. J. Charles, "Stress Rupture Evaluation of High-Temperature Structural Materials." To be published in the Proceedings of the International Symposium on Fracture Mechanics of Ceramics, University Park, PA. July 1977.
18. R. J. Charles, "High Temperature Stress Rupture of Polycrystalline Ceramics." Submitted for publication to J. Am. Ceram. Soc.
19. S. Prochazka, "Investigation of Ceramics for High-Temperature Turbine Vanes," Final Report, Contract N00019-72-C-0129, G.E. Report No. SRD-72-171, Dec. 1972.
20. C. Herring, "Diffusional Viscosity of a Polycrystalline Solid," J. App. Phys., 21, 437 (1950).
21. R. Raj, M. F. Ashby, "On Grain Boundary Sliding and Diffusional Creep," Met. Trans., 2, 1113 (1971).
22. R. L. Fullman, "Measurement of Particle Size in Opaque Bodies," Trans. AIME, 197, 447 (1953).
23. R. N. Ghoshtagore, R. L. Coble, "Self-Diffusion in Silicon Carbide," Physical Rev., 143, 623 (1966).
24. R. C. Folweiler, "Creep Behavior of Pore Free Polycrystalline Aluminum Oxide," J. App. Phys., 32, 773 (1961).
25. S. Shinozaki and K. R. Kinsman, "Influence of Structure on Morphology in Polycrystalline Silicon Carbide," in Ceramic Microstructures '76 Ed. by R. M. Fulrath and J. A. Pask, 1977.

26. I. W. Donald and P. W. McMillan, "Review: Ceramics-Matrix Composites," J. Mater. Sci., 11, 949 (1976).
27. D. P. H. Hasselman and R. M. Fulrath, "Mechanical Properties of Continuous Matrix, Dispersed Phase Ceramic Systems," p 343 in Ceramic Microstructures, Ed. by R. M. Fulrath and J. A. Pask, John Wiley & Sons, Inc., New York, NY, 1968.
28. A. G. Evans, "The Role of Inclusions in the Fracture of Ceramic Materials," J. Mater. Sci., 9, 1145 (1974).

Appendix A

STRESS RUPTURE TESTING OF SILICON CARBIDE AT VERY HIGH TEMPERATURES

R. J. Charles and S. Prochazka

INTRODUCTION

As ceramic materials continue to be developed for purposes of sustaining mechanical load at very high temperatures, the problem of categorizing the load bearing life-time performance characteristics of these materials becomes increasingly difficult and experimentally time consuming. Two major factors contribute to such evaluations. On the one hand, the temperatures involved are extreme if rupture at nominal stresses is to be achieved in reasonable times; and second, the volumes of material under desired tensile stresses are likely to be small if the normal and convenient bend test experimentation is to be utilized.

The latter factor is of great importance because, if the results are to be used for components of practical size, a reasonably accurate extrapolation of strength capability as a function of stressed volume must be undertaken. Clearly, the accuracy of this extrapolation is improved if the degree of extrapolation is reduced. Sedlacek and Halden⁽¹⁾ have developed a "pressurized tube technique" for the strength testing of ceramics at room temperature. This test offers the advantage of a large stressed volume resulting from the nearly uniform tensile stresses generated throughout the wall of the pressurized tube. In fact, with tubes of reasonable configuration, the effective stressed volumes can be increased by several orders of magnitude compared to those encountered with the same amount of specimen material in a bend test arrangement.

The object of the present work is to report a pressurized-tube, stress-rupture experimental procedure, using sintered silicon carbide material at a very high temperature, and to correlate the results with those theoretically expected.

EXPERIMENTAL PROCEDURE

Closed-end tubes 26 cm long, approximately 1.3 cm OD, and 1.0 cm ID (in the final fired state) were slip-cast from an aqueous dispersion of silicon carbide stabilized by tetramethylammonium hydroxide at pH 10 and 1/2% by weight of solid of urea-formaldehyde resol.* Slip-casting was done in plaster-of-paris molds, and the castings were fired at 2150 °C in 1 atm of argon to a final density of about 96%. The closed ends of the tubes were hemispherical with wall thicknesses of about 1.5 mm.

Pressurizing of a thin-walled, closed-end tube results in tangential and longitudinal tensile stresses of:

*URAC 180, American Cyanamide Company.

$$\frac{Pd}{2t} \text{ and } \frac{Pd}{4t},$$

respectively, where P is the inside hydrostatic pressure, d is the diameter, and t is the wall thickness.

These equations are strictly correct only for thin-walled pressure vessels where the inside diameter is essentially equivalent to the outside diameter. The ratio of wall thicknesses to diameters of the tubes in the present tests would not generally be classified as those for a thin-walled vessel, but for the sake of simplicity in this initial study such an assumption was made. The tubes were circular within 0.2 mm. Therefore, no correction for ovality was necessary.

The open end of the tube was sealed into a pressure head with epoxy resin and "proof-tested" at room temperature by pressurizing to 15.2 MPa (2200 psi) nitrogen pressure which resulted in hoop stresses of approximately 51.5 MPa (7480 psi). The tube was then inserted into a graphite resistance laboratory furnace of the type described by St. Pierre and Curran.⁽²⁾ Gas cylinders were used as the source of nitrogen, and the pressure was controlled with a pressure regulator.

The temperature was measured by an optical pyrometer sighting on the closed end of the tube through a window in the opposite end of the furnace. By adjusting the position of the tube progressively farther into the furnace, it was possible to measure the temperature gradient near the hot zone and to position the tube such that the highest temperature was about 1 cm from the end. In this position there was a temperature drop from the hottest region to the closed end of about 30 °C over a total length of approximately 1 cm. The temperature as measured by the pyrometer was corrected for losses by the furnace window and a mirror. An accuracy of ± 20 °C is estimated for the quoted temperatures, and the region of highest temperature is estimated to be 2 cm long.

Numerous safety precautions were taken to avoid injury at the time of specimen failure. Rather than position the optical pyrometer directly outside the furnace, a mirror was used allowing the pyrometer and the operator to be positioned behind a barrier. The circumference and both ends of the furnace were shielded to help contain any fragments of hot specimen, etc. which might be released if the furnace shell should fail. Despite such precautions, it was estimated that the graphite felt insulation inside the furnace would be of sufficient thickness to absorb the energy and contain the specimen fragments, thus preventing damage to the furnace shell. It was observed during the experiments that fragments from

failed specimens were contained within the furnace, requiring only new insulation and a new heating element to repair the damage. Nevertheless, similar safety precautions employing barriers are strongly recommended in the use of such a testing procedure.

Table I lists the temperatures, wall stresses, and test times for tests on three tubes as described above.

TABLE I

Experimental Tube Bursting Data

Tube Test	Temp (°K)	Tangential Wall Stress (MPa/kpsi)	Time (min)
A	2303	35.2/5.11	90
	2353	35.2/5.11	105
	2373	35.2/5.11	45
	2283	46.4/6.74	30
	2303	46.4/6.74	15
	2353	46.4/6.74	15
	2383	46.4/6.74	23 (failure)
B	2433	28.1/4.08	15
	2433	56.2/8.16	0.25 (failure)
C	2453	32.0/4.64	12 (failure)

THEORY AND ANALYSIS OF RESULTS

Prochazka, Johnson, and Giddings⁽³⁾ have shown that die-pressed and sintered forms of silicon carbide, processed for high average strength, exhibit Weibull moduli, m , of around 5 to 6. By using the two-parameter Weibull formulation, we may estimate the "quick time" or low-temperature bursting strength of that section of the tube (≈ 1 inch long) in which stress rupture failure would be expected to occur at high temperature in the previously described experiments. The two-parameter Weibull formula may be given as in Eq. (1), where P is the cumulative probability of failure of a given structure; σ_m is the maximum tensile stress in the structure; KV is the "effective volume" under tension; and σ_0 is a normalizing constant.

$$\ln \ln \frac{1}{1-P} = m \ln \sigma_m + \ln (KV/\sigma_0^m) \quad (1)$$

For three-point bend $K = 0.5/(m+1)^2$ and pure tension $K = 1$; thus, for a constant probability of failure of two structures where one is a standard three-point bend specimen and the other is a volume of material under uniform tension, one has

$$\sigma_T/\sigma_B = (0.5(V_B/V_T)/(m+1)^2)^{1/m} \quad (2)$$

where the subscripts T and B refer, respectively, to the structure under uniform tension and the three-point bend specimen. For the slip-cast sintered SiC material the appropriate Weibull modulus, m , has not been determined. Therefore, for purposes of

estimation we use a value of 5 consistent with values appropriate for die-pressed materials. As reported previously⁽³⁾ the bend bar shape utilized in testing of these materials is 0.4 cm by 0.4 cm by 4.0 cm (0.16 inch by 0.16 inch by 1.6 inch). Thus, for the tubes and bend bar geometries the ratio σ_T/σ_B calculates to be about 0.35 -- and for an MOR of 4.13 MPa (60 kpsi), appropriate to the slip cast material as shown by Prochazka,⁽⁴⁾ the expected "quick time" or low-temperature rupture stress for the slip cast tube end (1 inch long) would be about 1.43 MPa (20.7 kpsi).

An estimate of the stress rupture characteristics of dense, sintered silicon carbide* at very high temperatures has been recently made⁽⁵⁾ by a theoretical extrapolation of 1600 °C rupture data given for this material by Trantina and Johnson⁽⁶⁾ and by Prochazka.⁽⁷⁾ The theory⁽⁸⁾ for the extrapolation was based on the concept of the growth in the material of preexisting flaws to critical sizes which would result in catastrophic failure under the applied load. Crack growth was related to diffusional processes in the material such that the formulation for predicting stress rupture behavior involved a parameter which could be described as a "temperature modified failure time" (i.e., the time integral of the exponential of an activation energy of diffusion divided by temperature and the Boltzmann constant). Such a parameter is similar to the Orr-Sherby-Dorn (OSD) parameter,⁽⁹⁾ applicable in the stress rupture analysis of metals, and is referred to in the present work by the same symbol, θ_r , utilized earlier by these authors.

Utilizing this parameter, the result of the stress rupture theory indicated above⁽⁸⁾ may be given in the following mathematical form:

$$Z(N, R) = \int_0^{t_r} \frac{\exp(-\Delta H_c/kT) dt}{\theta_0} = \frac{\theta_r}{\theta_0} \quad (3)$$

In Eq. (3), t_r is the rupture time, R is the ratio σ_a/σ_{max} where σ_a is constant stress applied to the sample, and σ_{max} is an upper limit of stress, which when applied, results in immediate failure. The latter stress is thus independent of diffusional processes and reflects the strength limiting flaws in the as-processed material. For a given material or sample, this stress may most conveniently be determined by tests at sufficiently low temperatures that diffusional effects would be negligible. Also in Eq. (3), kT has its usual significance; ΔH_c is an activation energy for creep or the diffusion of those species responsible for creep; θ_0 and N are constants for a given material, which may be estimated theoretically but are more appropriately determined experimentally; and $Z(N, R)$ is a stress function which results from the theory to be of the following form,

$$Z(N, R) = \frac{e^{-NR} \left(N^3/R + \frac{3N^2}{R^2} + \frac{6N}{R^3} + \frac{6}{R^4} \right)}{e^{-N(N^3 + 3N^2 + 6N + 6)}} \quad (4)$$

*Fractional % boron additives utilized as sintering aids.

It may be noted in Eq. (3) that if the temperature is constant then

$$\theta_r = t_r \exp(-\Delta H_c/kT) \quad (5)$$

and, as such, is identical with the definition of this parameter as originally given by OSD. However, if the temperature varies with time during the test then θ_r is a summed or integral value as indicated in Eq. (3). It will be necessary to use the more general definition in the following analysis of tube bursting data because temperature changes in fact, did, occur during the course of a single experiment.

It should further be noted that Eq. (3) applies to a simple rupture experiment (a single constant stress) and involves an approximation arising from a disregard of a limit of integration for terms on the left-hand side of the equation. (8) As such, Eq. (3) introduces an error which becomes appreciable as R approaches the numerical value of one. The present work will be concerned with varied and progressive changes in applied stress during the course of single rupture experiment. Thus, it will be necessary to account for the effects of prior stress (and temperature) histories on the growth of cracks and the progressive weakening of a given test sample. In such cases, neglect of the integration limit, as is appropriate for most, simple rupture experiments, is not proper. With both limits, Eq. (3) reverts to the following equation which can properly account for interim states in the process toward rupture,

$$Z(N, R_i) - Z(N, R_q) = \frac{\int_0^{t_r} \exp(-\Delta H_c/kT) dt}{\theta_0} \quad (6)$$

$$= \frac{\theta}{\theta_0}$$

R_i is the initial value of σ_a/σ_{max} and R_q is the interim value. It may be well to point out that the difference between R_i and R_q is the result of the change in σ_{max} , the quick time strength of the sample, under the constant applied stress, σ_a . This change results from the growth of a strength limiting flaw from its initial size to some interim size with a consequent reduction in instantaneous strength of the sample.

Equation (6) is the appropriate equation for analyzing the data in Table I to determine if the preliminary and lower stress applications contributed any significant weakening of the specimen before the higher and final stress was applied.

From other work⁽⁵⁾ a value of $\Delta H_c = 250$ kcal/mol and a $\log \theta_0 = -35.33$ have been indicated as appropriate for dense, sintered silicon carbide and, since in the previous discussion a value of 0.35 was calculated for the ratio σ_T/σ_B , the expected quick time strength, σ_{max} , of the slip-cast burst tubes would be 0.35 (413.3) = 143 MPa (20.7 kpsi). Table II lists a two-stage calculation to determine the appropriate θ_r value for tube A.

TABLE II(a)

Calculation of θ_r for Tube A

Temp (°K)	R_i (σ_a/σ_{max}) _i	θ (hr $\times 10^{24}$)
2303	0.247	0.40
2353	0.247	4.02
2373	0.247	14.85
2283	0.247	9.96

$$\Sigma \theta = 2.92 \times 10^{-23} \text{ hr}$$

$$Z(N, R_q) = Z(N, R_i) - \frac{\Sigma \theta}{\theta_0}$$

$$= Z(39, 0.247) - \frac{2.92 \times 10^{-23}}{5.12 \times 10^{-26}}$$

$$= 5.6 \times 10^{13}$$

$$\therefore R_q = 0.249$$

We conclude from Table II(a) that the preliminary stress and thermal history for tube A results in a slight weakening of the tube amounting to about 1% of its original strength capability [i.e., (0.249 - 0.247)/0.247 ~ 0.01]. Thus the apparent stress ratio $R(0.326)$ given in Table I for the remainder of the experiment should be increased by this small factor [i.e., 1.01 (0.326) ~ 0.329], but it is clear that such a correction is small relative to other uncertainties in the data. The above calculation does indicate, however, that the lifetime of the sample is governed almost totally by crack growth under the final stress at which rupture was observed. Table II(b) gives the remaining calculation for θ_r for tube A under these conditions.

TABLE II(b)

Calculation of θ_r for Tube A

Temp (°K)	R_i (σ_a/σ_{max}) _i	θ (hr $\times 10^{24}$)
2283	.329	0.83
2303	.329	0.67
2353	.329	2.12
2383	.329	6.35

$$\Sigma \theta = \theta_r = 9.97 \times 10^{-24} \text{ hr}$$

Similar calculations, accounting for the prior stress history of tube B, indicate that virtually no weakening of this tube occurred as a result of the preliminary loading and that rupture was almost totally determined by the final and higher stress. Table III therefore summarizes the summed or integral OSD rupture parameters for all three tubes.

Figure 1 plots the data (solid circles) listed in Table III on the estimated stress rupture curve for sintered silicon carbide which was prepared earlier (Ref. 5) from rupture data^(6,7) obtained at 1600 °C (open circles) and the equation referred to in this work as Eq. (3). It is evident that the stress rupture results

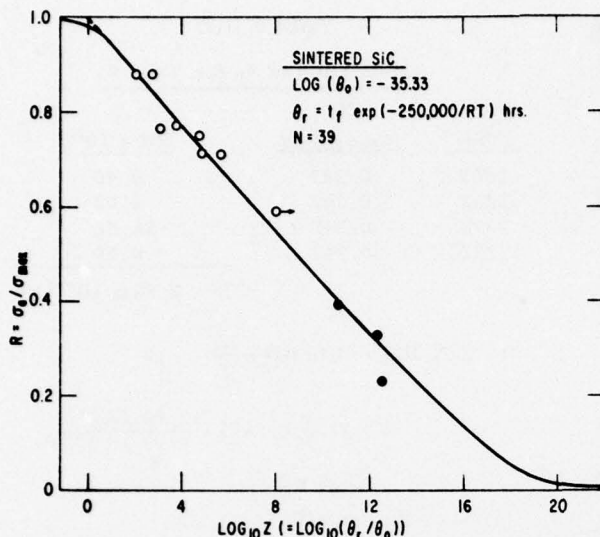


Fig. 1 Estimated stress rupture curve for dense, pure-phase sintered silicon carbide according to Eq. (3) and the physical parameters listed in the figure. Open-circle points calculated from experimental bend bar data at 1600 °C; (6, 7) closed-circle points calculated from experimental data of this work.

TABLE III

Summary of θ_r Values

Tube Test	R (σ_a / σ_{max})	θ_r (hr $\times 10^{24}$)	Log $\frac{\theta_r}{\theta_0}$ *
A	0.329	9.9	12.33
B	0.394	0.203	10.64
C	0.224	14.8	12.50

*Log $\theta_0 = -35.33(5)$

of this work, obtained at low stresses and very high temperatures, are reasonably consistent with the originally estimated characteristics of this material.

It should be noted, however, that the approach described herein involves several uncertainties and estimates related to the data. In particular some concern exists that the two-parameter Weibull formulation, which is used in the present work to correlate sample strength with stressed volume, may overestimate the degradation in strength because of increased volume under stress. (3) On the other hand, the bursting behavior of the tubes was correlated to only the tangential stress in the tube walls. The true stress state is biaxial and the neglect of the action of flaws brought into unfavorable orientation with

*Earlier analyses of crack dynamics governing delayed failure identify this same time integral as the determining factor in rupture life in systems involving thermal activation (e. g., Ref. 10).

respect to the smaller, longitudinal stress would compensate, to some degree, an overestimation of strength degradation resulting from increased volume under stress.

The present analysis suggests a further aspect of stress rupture testing that may have general applicability to materials in which diffusional processes play a dominant role in time-dependent failure. For rupture under a given stress, the parameter governing lifetime is, according to Eq. (3), the time integral of the exponential of $-\Delta H/kT$. * For a constant rate of temperature increase, δ , the relation between the integral OSD parameter, θ_r , and the rate of temperature increase would be simply,

$$\theta_r = \frac{1}{\delta} [T \exp(-\Delta H_C/kT) + Ei(-\Delta H_C/kT)] \frac{T_r}{T_0} \quad (7)$$

where the evaluation limits are the initial temperature, T_0 , and the higher rupture temperature, T_r , and the symbol Ei refers to tabulated exponential integrals. For nonlinear temperature schedules, similar integrals may be evaluated. It is evident that data necessary to describe the stress rupture characteristics of a material could be obtained in a dynamic fashion in which the experimental procedure would be to raise the temperature in a controlled manner and note the final temperature at which rupture occurred. This procedure would introduce a degree of control in developing test data that is absent in the normal procedure where stress and temperature are fixed, and there is no assurance that failure can be achieved within a practical time interval.

In many respects the above procedure, involving a variation in temperature, is complementary to a procedure suggested earlier⁽¹¹⁾ to assure that failure occurred within practical times. This latter procedure involved a controlled increase of applied stress to the rupture point. For the results to be useful, however, for generalizing on stress rupture, it was necessary to assume a relation between crack growth velocity and applied stress. Such relations are exceedingly difficult to define with high accuracy. In the present scheme, involving temperature variations, it should be possible to determine the unknown factor in Eq. (7), ΔH_C , to high accuracy with only a few controlled measurements. Once the factor, ΔH_C , is established then experiments at different stress levels could rapidly develop the necessary stress dependencies of failure time.

SUMMARY AND CONCLUSIONS

A bursting tube testing procedure, described by Sedlacek and Halden, (1) has been evaluated as a means of obtaining high-temperature stress rupture data on pure-phase, sintered silicon carbide. This procedure was selected since it offered a simple method for high-temperature experimentation and the possibility of increasing the effective volume under stress by a factor of about two orders of magnitude greater than that obtained in small bend bar testing. Analysis of the results indicates that:

1. The bursting tube technique is a useful and convenient procedure for the extension of high-temperature mechanical properties measurements to specimens of relatively large stressed volume.
2. In the range of 2000 °C, dense, pure-phase sintered silicon carbide exhibits practical strengths and rupture life times in inert atmospheres.
3. Parameters have been defined for a stress rupture function which, when combined with a simple form of Weibull statistics, permits reasonable estimates of the stress rupture performance of this material at high temperature in varied sample configurations.
4. Stress rupture testing procedures which employ controlled temperature variations are analyzable and may have general applicability.

ACKNOWLEDGMENTS

The authors are indebted to C. A. Johnson and R. A. Giddings for many useful discussions and suggestions during the course of the work.

REFERENCES

1. R. Sedlacek and F. C. Halden, "Method for Tensile Testing of Brittle Materials," *Rev. Sci. Instr.* 33, 298 (1962).
2. P. D. S. St. Pierre and M. J. Curran, "A Simple Laboratory Furnace for Use up to 2500 °C," General Electric TIS Report.
3. S. Prochazka, C. A. Johnson, and R. A. Giddings, "Investigation of Ceramics for High Temperature Turbine Components," Final Report Contract N62269-75-C-0122, Naval Air Systems Command, December 1975.
4. S. Prochazka, R. A. Giddings, and C. A. Johnson, "Investigation of Ceramics for High Temperature Turbine Vanes," Final Report Contract N62269-74-C-0255, Naval Air Systems Command, November 1974.
5. R. J. Charles, "High Temperature Stress Rupture of Polycrystalline Ceramics," submitted to *J. Am. Ceram. Soc.*
6. G. G. Trantina and C. A. Johnson, "Subcritical Crack Growth in Boron Doped SiC," *J. Am. Ceram. Soc.* 58 (7-8), 344-345 (1975).
7. S. Prochazka, "Investigation of Ceramics for High Temperature Turbine Vanes," Final Report Contract N00019-72-C-0129, Naval Air Systems Command, p. 27, December 1972.
8. R. J. Charles, "Diffusion Controlled Stress Rupture of Polycrystalline Materials," *Met. Trans.* 7A, 1081-89 (1976).
9. R. L. Orr, O. D. Sherby, and J. E. Dorn, "Correlations of Rupture Data for Metals at Elevated Temperatures," *Trans. ASM* 46, 113-128 (1954).
10. R. J. Charles, "Static Fatigue of Glass. II," *J. Appl. Phys.* 29, No. 11, 1554-60 (1958).
11. R. J. Charles, "Dynamic Fatigue of Glass," *J. Appl. Phys.* 29, No. 12, 1657-62 (1958).

Appendix B

HIGH-TEMPERATURE STRESS RUPTURE OF POLYCRYSTALLINE CERAMICS

R. J. Charles

INTRODUCTION

An analysis of the high-temperature stress rupture process in polycrystalline materials has recently been presented⁽¹⁾ in which the major factors governing time-dependent rupture were identified as the diffusivities of the atomic species responsible for diffusional creep and the dependence of these diffusivities on mechanical pressures. Creep at high temperatures was assumed to result from the processes described by Nabarro⁽²⁾ and Herring⁽³⁾ for the relaxation of stress by the diffusion of atoms or vacancies from one pressure state to another. A fracture mechanics approach was utilized to describe these pressure states, such that flaws within grain boundaries would propagate under an applied load and ultimately result in rupture. Thus, in principle, the stress rupture performance of a polycrystalline material could be described wholly in terms of diffusional parameters governing creep, the pressure and temperature dependencies of these parameters, and time-independent physical properties of the material.

While the above analysis was primarily undertaken to provide information which would assist in categorizing the high-temperature mechanical properties of a number of recently developed structural ceramics, it was found that little data existed in the literature on stress rupture of ceramics to which the above analysis could be applied for purposes of verification. An abundance of stress rupture data exists for metals and alloys. Application of the analytical procedures developed in the preceding work to a number of pure metal and alloy systems indicated that the stress rupture characteristics of these materials could be accounted for with good accuracy over a large range of times, temperatures, and applied stresses. Similar descriptions should be possible for the stress rupture characteristics of polycrystalline ceramics.

The objectives of the present work are to apply the above procedures to the limited stress rupture data available on ceramics and, more particularly, to use these procedures to provide estimates of the potential service life times of recently developed silicon nitride and silicon carbide structural ceramics.

BACKGROUND THEORY

The stress rupture relationship, referred to in the previous section, is given by the following equation:

$$e^{-RN} [N^3/R + 3N^2/R^2 + 6N/R^3 + 6/R^4] \approx 8 D_s (\beta \sigma_{\max})^4 (e^{-\beta \gamma / \rho / \rho^2}) t_f \quad (1)$$

In the above equation, R is a dimensionless ratio, σ_a / σ_{\max} , where σ_a is the stress applied to a sample and σ_{\max} is the upper limit of applied stress which results in instantaneous rupture without any time-delayed effects. This latter stress, σ_{\max} , is generally to be obtained by tests at sufficiently low temperatures that diffusional processes would have negligible effects on the failure process and thus this stress reflects the characteristics of the strength limiting flaws existing in the material prior to test. The factor N is a further dimensionless quantity given by the product $8\sigma_{th}$ where σ_{th} is the cohesive or theoretical strength of a grain boundary and β is a constant determined by the pressure coefficient of diffusion of the mobile species in the material. As has been shown (Ref. 1), β may be estimated for uniaxial stress situations from the activation volume, v^* , of the diffusing species according to the following equation,

$$\beta \approx v^* / 3kT \quad (2)$$

where kT has its usual significance.

Further, in Eq. (1), D_s is the diffusion coefficient of mobile species and may be given in its usual form,

$$D_s = D_0 \exp(-\Delta H_c / kT) \quad (3)$$

where ΔH_c is the activation energy for diffusion and D_0 is the preexponential factor. The final three parameters γ , ρ , and t_f , are, respectively, the surface energy of the material, the radius of curvature of an advancing flaw tip (estimated to be of atomic dimensions), and the time to failure after application of the applied stress.

It is evident that many of the parameters given in Eq. (1) will be difficult to determine, even for estimates, and indeed the equation involves a number of simplifying approximations. Consequently, the best utility of Eq. (1) may reside in its use to rationalize existing stress rupture data or to extrapolate such data outside of the range of tests.

Recognizing that Eq. (1) embodies the well-known Orr-Sherby-Dorn (OSD)⁽⁴⁾ stress rupture parameter, $\theta_r = t_f \exp(-\Delta H_c / kT)$, where ΔH_c is the activation energy for creep, it is useful to collect remaining terms specific to a given material into an analogous parameter, θ_0 , which has units of time similar to θ_r . Thus, Eq. (1) may take the form,

$$\frac{e^{-N(R-1)} (N^3/R + 3N^2/R^2 + 6N/R^3 + 6/R^4)}{(N^3 + 3N^2 + 6N + 6)} = Z = \frac{\theta_r}{\theta_0} \quad (4)$$

where both sides of the equation represent dimensionless ratios. If the activation energy for creep, ΔH_c , is known for a polycrystalline ceramic then, in principle, two experimental values of failure times t_f , and their respective applied stress ratios, $R = \sigma_a / \sigma_{max}$, are sufficient to define θ_0 and N in the above equation. Once these parameters are defined, failure times under stress rupture may be estimated for all ranges of stresses and temperatures, and the slope parameter, N , may be compared with that theoretically expected.

The use of Eq. (4) presupposes that an estimate or test value of the instantaneous strength (or low-temperature strength), σ_{max} , is available. If such is not the case, then Eq. (4) may be cast in a further form which, however, when utilized, provides no corroboratory information concerning the expected slope parameter value, N , for a given system. This form is given in Eq. (5) wherein one sets $V = N / \sigma_{max}$ and thus

$$e^{\sigma_a V} (V^3 / \sigma_a + 3V^2 / \sigma_a^2 + 6V / \sigma_a^3 + 6 / \sigma_a^4) = Z' = \frac{\theta_r}{\theta_0'} \quad (5)$$

where θ_0' is a new constant for a given system.

APPLICATIONS



Wallis(5) has reported several series of stress rupture results on fibers and rods of sintered alumina. Figure 1 reproduces Wallis' results for alumina for

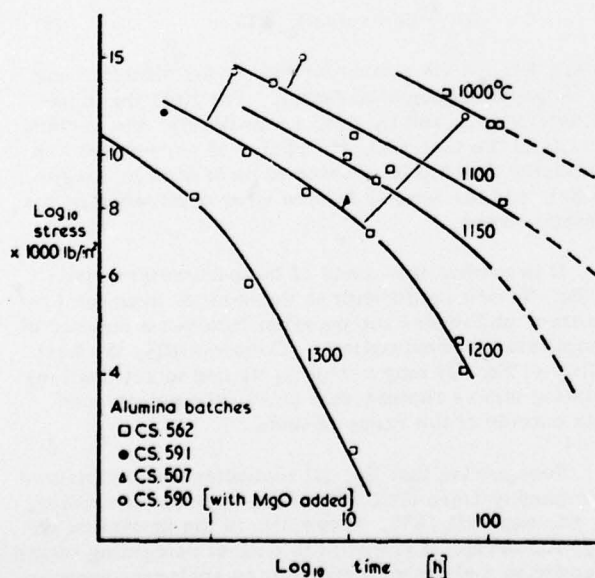


Fig. 1 Stress rupture of alumina rods [after Wallis(5)].

a number of temperatures, times, and applied stresses. For this material, low-temperature results were also given which allow estimates of the instantaneous strength of the fabricated rods. Consequently, Eq. (4) may be applied to these data. In addition, Rosolowski and Greskovich(6) have summarized a large amount of data on the sintering of alumina, and conclude that the activation energy of the sintering process for this material is most characteristically given by a value of about 115 kcal/mole. We utilize this value as the appropriate value for ΔH_c which would govern the diffusion mechanisms for both sintering and creep in polycrystalline alumina. Figure 2 gives the results of applying Eq. (4) to Wallis' data and using a value of $\Delta H_c = 115$ kcal/mole. The points are determined from the experimental values of θ_r , utilizing an arbitrary constant θ_0 , whereas the solid line through the points corresponds to the theoretical function on the left-hand side of Eq. (4) using a slope parameter (N) value of 16. We may estimate whether or not such an N value is reasonable using the relation $N = v^* \sigma_{th} / kT$ and setting v^* as about 5 cc/mole, σ_{th} as about 0.2 of Young's Modulus (3.8×10^5 MN/m²) and a temperature of about 1000 °C. A calculated value for N of about 12 results, which is roughly in accord with that observed.

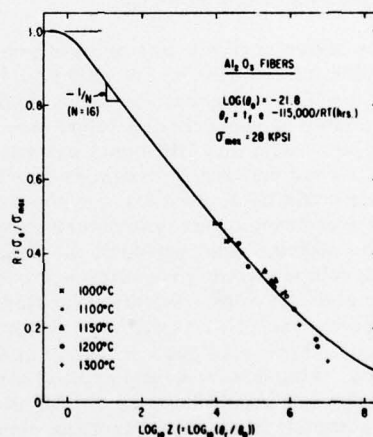


Fig. 2 Experimental stress rupture values of Wallis [Ref. (5)] (points) for sintered alumina rods compared with the stress rupture curve (solid line) predicted by Eq. (4), utilizing the physical parameters listed in the figure.

As indicated in Fig. 2 there is an apparent deviation of experiment from theory for R values less than about 0.2. This deviation may not be real since at such low R values (low applied stresses) the crack sizes, just prior to rupture, can be calculated from the Griffith theory to be a significant fraction of the section sizes of the relatively small diameter fibers used in the experiments. Consequently, the true stresses on the unruptured portions of the fibers, just prior to failure, would be significantly larger than the apparent stresses, and the θ_r points would therefore fall below the expected solid line.

SiC

Walles does not report low-temperature strength values of the silicon carbide fibers used in his stress rupture experiments and thus, since a value of the instantaneous strength is not available, Eq. (5) is utilized to analyze his results. Figure 3 reproduces the original test data and Fig. 4 shows the results of applying Eq. (5) to the data. In this case, curves corresponding to the function represented by the left-hand side of Eq. (5) were first passed through the experimental data for each temperature at which experiments were reported. This procedure served to identify a value of ΔH_c of 130 kcal/mole as best fitting the overall data. The results for all temperatures were then combined to result in the representation given in Fig. 4 in which the solid line is the final curve corresponding to the Z' function and the points are derived from experimental θ_r values. It is evident that the curvature in the experimental data can be well represented by the theoretical stress rupture function. However, it is of some interest that the appropriate ΔH_c value for these silicon carbide fibers is as low as 130 kcal/mole. The data of Ghoshtagore and Coble(7) would suggest a substantially higher value (250 to 300 kcal/mole) for the activation energy for the species (carbon) controlling diffusive creep in silicon carbide. Further, the results are of significant interest, in that even at short times there exists almost a threefold reduction in strength of the fibers when tested at 800 °C and tested at the still relatively low temperature of 1100 °C.

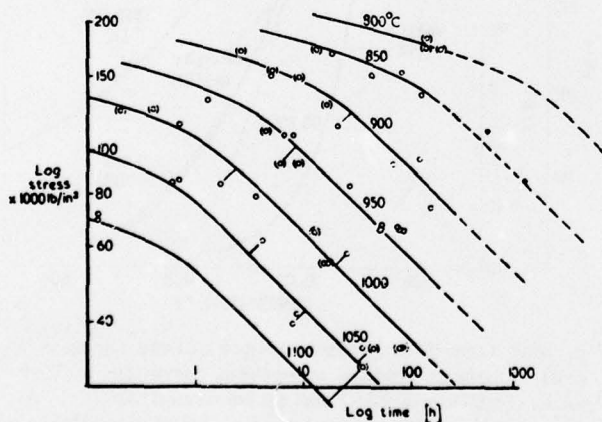


Fig. 3 Stress rupture of silicon carbide fibers [after Waller(5)].

Silicon carbide fibers are generally prepared by chemical vapor deposition processes and, as such, are usually of high purity. As will be shown, the dense, pure-phase silicon carbide shows high strength in bulk form at temperatures of 1600 °C or higher. Consequently, Waller's fibers of SiC do not show the high-temperature stability normally expected for a high-purity SiC. Often, CVD fibers are grown on a refractory metal substrate, e.g., tungsten. We note that the activation energy for self-diffusion in

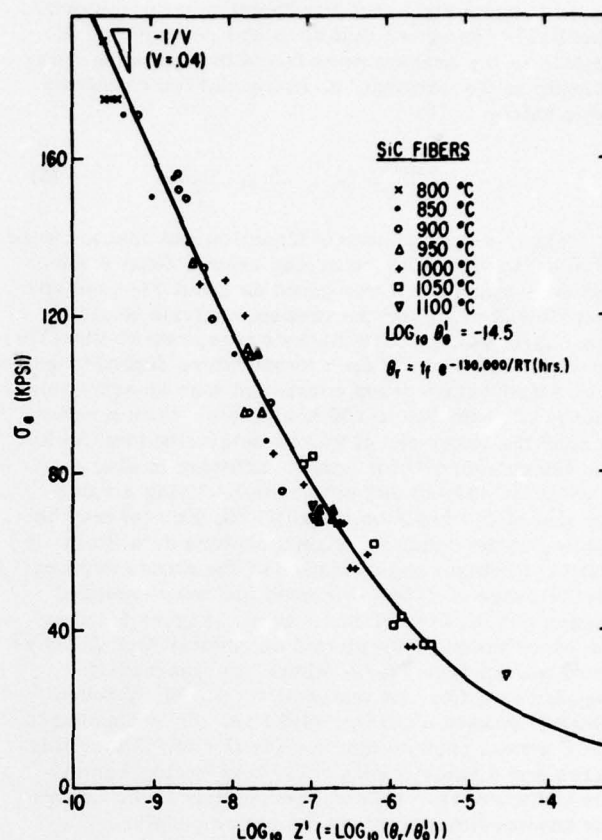


Fig. 4 Experimental stress rupture values of Waller (Ref. (5)) (points) for silicon carbide fibers compared with the stress rupture curve (solid line) predicted by Eq. (5) utilizing the physical parameters listed in the figure.

tungsten is about 130 kcal/mole, which is equivalent to that for the stress rupture process exhibited by Waller's fibers. It is possible, therefore, that both the high-temperature strength and creep rupture properties of Waller's fibers are not determined by SiC but by a substrate material such as tungsten. If this could be substantiated, it would indicate that the stress rupture analysis procedure utilized in this work has value not only for extrapolatory uses but also for evaluating the behaviors of complex, composite systems.

Sintered SiC

Trantina and Johnson(8) and Prochazka(11) have reported limited stress rupture data on a form of dense, pure-phase sintered SiC described earlier by Prochazka(9). The information consisted of both static fatigue (i.e., constant stress) and constant stress rate data. The former authors report their data over a limited range according to a semi-empirical relationship(10) derived for brittle materials on the basis of an early form of fracture mechanics theory and which may be given as follows:

$$\ln R = \ln (\sigma_a / \sigma_{\max}) = \frac{-1}{n} \ln t_f + K \quad (6)$$

where K and n are constants specific to the material. Charles⁽¹⁾ has shown that the slope parameter, N , utilized in the present work bears the following relationship to the constant, n , in Eq. (6) for relatively large values of R :

$$\frac{\partial \ln R}{\partial \ln t_f} = -\frac{1}{n} \approx -\frac{1}{NR} \quad (7)$$

Thus, since the data of Trantina and Johnson were obtained for R values centering around about 0.84-- and their value for n was given as about 33-- the appropriate N value for the present analysis would be about 33/0.84~39. Prochazka's creep rate studies⁽¹¹⁾ on this material indicate a temperature dependence of near steady-state creep consistent with an activation energy of about 210 to 250 kcal/mole. Such a value is near the lower end of values determined by Coble and Ghoshtagore⁽⁷⁾ for carbon diffusion in single-crystal SiC (250 to 300 kcal/mole). Using a value for ΔH_C of 250 kcal/mole and $N = 39$, Eq. (4) may be applied to the combined stress rupture data (Refs. 8 and 11) to obtain an estimation of the stress rupture performance of dense, sintered SiC over extended ranges of temperature and stress. Figure 5 shows the experimental data plotted as reduced Orr-Sherby-Dorn parameters (θ_r/θ_0 where the appropriate $\log_{10}\theta_0$ value for this material = -35.33) through which is passed a curve (solid line) corresponding to the Z stress rupture function for $N = 39$. Using this curve and a value of $\Delta H_C = 250$ kcal/mole, rupture times for sintered silicon carbide may be estimated for any combination of stress or temperature.

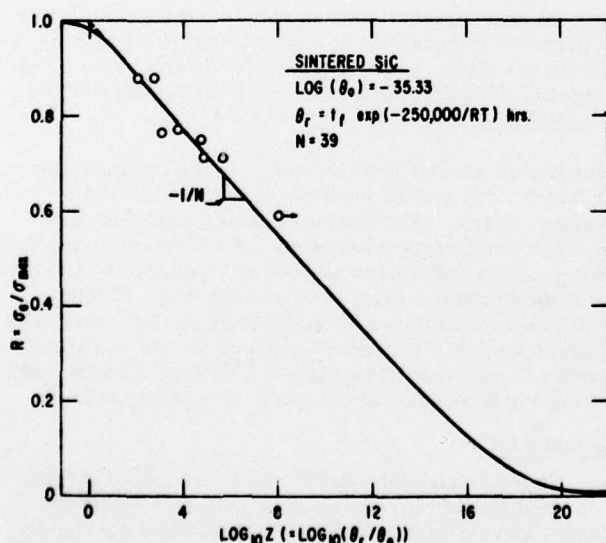


Fig. 5 Estimated stress rupture curve for sintered silicon carbide defined by experimental data (points) and Eq. (4) utilizing the physical parameters listed in the figure.

In general, designers find stress rupture information to be most conveniently represented in a plot

of applied stress vs temperature for various life times (e.g., 100, 1000, 10,000 hours, etc.) Figures 6(a) and (b) are such representations calculated directly from Eq. (4) where $\log_{10}\theta_0 = -35.33$ and $\Delta H_C = 250$ kcal/mole. It is to be noted that the σ_{max} value utilized in these calculations was 340 MN/m² (50 KPSI), which represents a value shown to be appropriate by Johnson and Trantina for sintered SiC in pure tension in air. The pure tension σ_{max} value is an appropriate value for the direct comparison of stress rupture performance of ceramics vs alloys. Such a comparison is shown in Fig. 6 wherein the stress rupture data of Betteridge⁽¹²⁾ and Goldhoff⁽¹³⁾ as analyzed by Charles (Ref. 1) for Nimonic 80A superalloy, is included. Also included in these figures are estimated stress rupture data on hot-pressed forms of Si₃N₄ and SiC. These latter data are obtained from the original work of Lange⁽¹⁴⁾ and were calculated using the same procedures as those outlined for the analysis of the data of Trantina and Johnson⁽⁸⁾ on sintered SiC. In the case of the hot-pressed materials, Lange reported constant stress rate data at several temperatures, thus allowing a direct evaluation of the appropriate stress rupture temperature dependence parameters, ΔH_C . Finally, in dashed lines, an estimated curve for an advanced superalloy, currently under development ($\gamma/\gamma'-\delta$),⁽¹⁵⁾ is also included for comparison purposes.

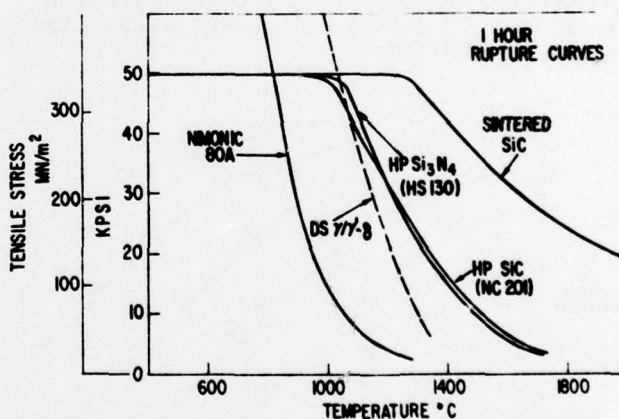


Fig. 6(a) One-hour stress rupture curves for several high-temperature structural ceramics and for an early (Nimonic 80A) and an advanced (DS $\gamma/\gamma'-\delta$) superalloy as determined by Eq. (4) and available experimental data.

Several features of these comparisons are of interest. For example, superalloys are superior in bulk strength at low temperatures and, in fact, strengths of 1000 MN/m² (150 KPSI) for these materials at low temperatures are common. However, there is a crossover at high temperatures where the stress rupture performances of the ceramics exceed the alloys. Another feature of interest is the fact that as longer and longer life times are required of the materials, the de-rating in maximum allowable temperature, for a given applied stress, is much

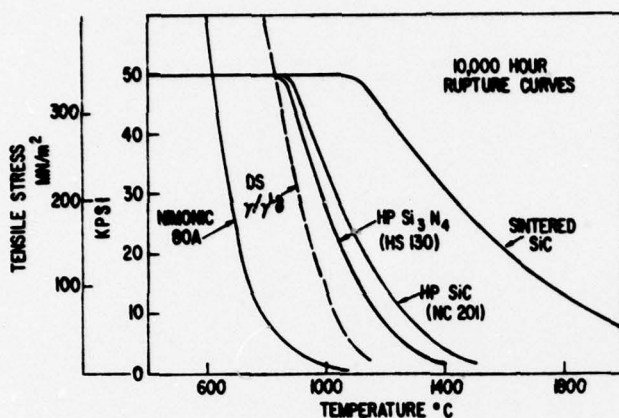


Fig. 6(b) 10,000-Hour stress rupture curves for several high-temperature structural ceramics and for an early (Niomic 80A) and an advanced (DS γ/γ' - δ) superalloy as determined by Eq. (4) and available experimental data.

less for the ceramics than for the alloys. Also of interest is the indication that sensible strengths of one of the ceramics, sintered SiC, are predicted for temperatures well in excess of 1600°C.

For applications involving inertial forces, designers generally require stress rupture data reported in terms of strength-to-weight ratios rather than simply strength. Figure 7 corrects all the materials in Fig. 6(b) for density and indicates that much of the disparity in low-temperature performance between alloys and structural ceramics is removed. In addition, this procedure has the obvious consequence of moving the crossover temperature for equivalent performance to much lower values.

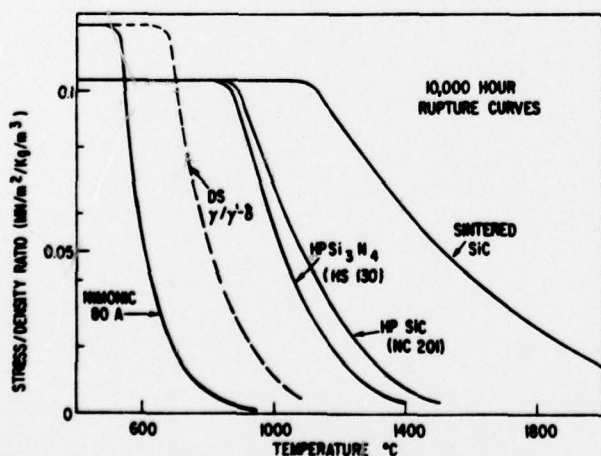


Fig. 7 Stress rupture curves as in Fig. 6(b) corrected for alloy or ceramic densities.

SUMMARY

Analytical procedures, developed for the evaluation and extrapolation of stress rupture data, have been applied to available experimental information on several high-temperature structural ceramics. While it is evident that none of the experimental information is as yet sufficiently extensive to fully substantiate the procedures which are outlined, the results are, however, consistent with the available data. Life-time estimates resulting from these procedures indicate that several ceramic materials, recently developed, possess high-temperature stress rupture properties that may be of significant interest in the design of high-temperature, long-lived, load-bearing machinery.

ACKNOWLEDGMENTS

The writer is indebted to S. Prochazka, C. A. Johnson, and R. A. Giddings for many helpful discussions during the course of the work and for assistance in interpreting experimental data.

REFERENCES

1. R. J. Charles, "Diffusion Controlled Stress Rupture in Polycrystalline Materials," *Met. Trans. A*, **7A**, 1081-1089 (1976).
2. F. R. N. Nabarro, *Report of a Conference on the Strength of Solids*, Physical Society, London (1948), p. 75.
3. C. Herring, "Diffusional Viscosity of a Polycrystalline Solid," *J. Appl. Phys.* **21**, 437-445 (1950).
4. R. L. Orr, O. D. Sherby, and J. E. Dorn, "Correlations of Rupture Data for Metals at Elevated Temperatures," *Trans. ASM* **46**, 113-128 (1954).
5. K. F. A. Wallis, "The Creep of Ceramic Materials Compared to that of Metals," *Proc. Brit. Ceram. Soc.* **15**, 157-171 (1970).
6. J. H. Rosolowski and C. D. Greskovich, "Theory of the Dependence of Densification of Grain Growth During Intermediate Stage Sintering," *J. Am. Ceram. Soc.* **5**, 177 (1975).
7. R. N. Ghoshtagore and R. L. Coble, "Self-Diffusion in Silicon Carbide," *Phys. Rev.* **143**, No. 2, 623-626 (1966).
8. G. G. Trantina and C. A. Johnson, "Subcritical Crack Growth in Boron-doped SiC," *J. Am. Ceram. Soc.* **58** (7-8), 344-345 (1975).
9. S. Prochazka, "Sintering of Silicon Carbide," *Proc. 2nd Army Materials Technical Conf.* (Nov. 1973), pp. 239-251. Also see "Sintering of Silicon Carbide," *Mass Transport Phenomena in Ceramics*, Proc. IX University Conf. on

Ceramic Sci., Case Western Reserve Univ.,
Cleveland, OH, June 3-5, 1974, Plenum Press,
New York 1975.

10. R.J. Charles, "Static Fatigue of Glass-II," J. Appl. Phys. 29, No. 11, 1554-1560 (1958).
11. S. Prochazka, "Investigation of Ceramics for High-Temperature Turbine Vanes," p. 26, Final Report Contract N00019-72-C-0129, Naval Air Systems Command, Dec. 1972.
12. W. Betteridge, The Nimonic Alloys, Edward Arnold Pub. Ltd., London (1959), p. 187.
13. R.M. Goldhoff, "Plasticity and Creep of Metals," J. Basic Eng. 81, 629 (1959).
14. F.F. Lange, "High-Temperature Strength Behavior of Hot Pressed Si_3N_4 : Evidence for Subcritical Crack Growth," J. Am. Ceram. Soc. 57, No. 2, 84-87 (1974).
15. A.F. McLean, E.A. Fisher, and R.J. Bratton, "Brittle Materials Design, High Temperature Gas Turbines," Interim Report No. 5, p. 107, Contract No. DAAG 46-71-C-0162, Advanced Research Projects Agency (April 1974).

DISTRIBUTION LIST
(one copy unless otherwise noted)

(3 copies plus balance after distribution)

Naval Air Systems Command
(AIR-52031B)
Department of the Navy
Washington, DC 20361

(7 copies for internal distribution by
AIR-954)

AIR-954 (2 copies), AIR-536B1 (1 copy),
AIR-330A (1 copy), AIR-330B (1 copy),
AIR-5361A (1 copy), AIR-5362A (1 copy)
Naval Air Systems Command (AIR-954)
Department of the Navy
Washington, DC 20361

(2 copies)

Commander
Naval Air Development Center
Code 302A (1 copy) Code 3023 (1 copy)
Warminster, PA 18974

(2 copies)

Naval Air Turbine Test Station
J. Glatz (PE-43) (1 copy)
J. E. Newhart (AEP-22) (1 copy)
1440 Parkway Avenue
Trenton, NJ 08628

Commander

Naval Sea Systems Command
Attn: NAVSEA 0352
Department of the Navy
Washington, DC 20362

Commander

Naval Weapons Center
Code 5516
China Lake, CA 93555

Naval Ships Engineering Center
(Code 6146)
Center Building Room 202
Prince George's Center
Hyattsville, MD 20782

(2 copies)

Air Force Materials Laboratory
Code LL H. M. Burte (1 copy)
Code LLS R. L. Crane (1 copy)
Wright-Patterson Air Force Base
Dayton, OH 45433

Naval Weapons Laboratory
Attn: W. Mannschreck
Dahlgren, VA 22448

U. S. Naval Ships Research
and Development Center
Code 2812
Annapolis, MD 21402

Commander
Naval Surface Weapons Center
(Metallurgy Division)
White Oak
Silver Spring, MD 20910

(2 copies)

Director
Naval Research Laboratory
Code 6130 (1 copy), Code 6360
(1 copy)
Washington, DC 20375

Office of Naval Research
The Metallurgy Program, Code 471
Arlington, VA 22217

Director
Army Materials and Mechanics
Research Center
(Ar. Gorum)
Watertown, MA 02172

U. S. Army Aviation Materiel
Laboratories
Fort Eustis, VA 23604

D2

Air Force Office of Scientific Research
Attn: Major W.C. Simmons
1400 Wilson Boulevard
Arlington, VA 22209

Air Force Propulsion Laboratory
Code TBP
Wright-Patterson Air Force Base
Dayton, OH 45433

Aeronautical Systems Division
Code ENJ
Wright-Patterson Air Force Base
Dayton, OH 45433

National Aeronautics and Space
Administration
Code RWM
Washington, DC 20546

(3 copies)
National Aeronautics and Space
Administration
Lewis Research Center
G.M. Ault (1 copy)
W.A. Sanders, M.S. 49-1 (1 copy)
H. P. Probst (1 copy)
21000 Brookpark Road
Cleveland, OH 44135

U.S. Energy Research and Development
Administration
Division of Research and Development
(A. Van Echo)
Washington, DC 20545

Metals and Ceramics Information Center
Battelle Columbus Laboratories
505 King Avenue
Columbus, OH 43201

The Johns Hopkins University
Applied Physics Laboratory
(Maynard L. Hill)
Johns Hopkins Road
Laurel, MD 20810

AVCO RAD
201 Lowell Street
Wilmington, MA 01887

ITT Research Institute
10 West 35th Street
Chicago, IL 60616

Detroit Diesel Allison Division
General Motors Corporation
Materials Laboratories
Indianapolis, IN 46206

Pratt and Whitney Aircraft Division
United Aircraft Corporation
East Hartford, CT 06108

Pratt and Whitney Aircraft
(Mr. A. Magid)
Florida Research and Development
Center
West Palm Beach, FL 33402

United Technologies Research Center
United Aircraft Company
East Hartford, CT 06108

Supervisory Materials Engineer
Airesearch Manufacturing Company
Department 93-39M
402 S. 36th Street
Phoenix, AZ 85034

Lycoming Division
AVCO Corporation
Stratford, CT 06497

Curtis Wright Company
Wright Aeronautical Division
Wood-Ridge, NJ 07075

Bell Aerosystems Company
Technical Library
P.O. Box 1
Buffalo, NY 14240

(3 copies)
General Electric Company
Aircraft Engine Group
Materials and Processes Technology
Laboratories (1 copy)
John Blanton, Advanced Tech.
Programs (1 copy)
AEG Technical Information Center,
Mail Drop N-3, Bldg. 700 (1 copy)
Evendale, Cincinnati, OH 45215

Solar
(Dr. A. Metcalfe)
2200 Pacific Highway
San Diego, CA 92112

Teledyne CAE
1330 Laskey Road
Toledo, OH 43601

Stellite Division
Cabot Company
Technical Library
P.O. Box 746
Kokomo, IN 46901

Norton Company
(Dr. N.J. Ault)
Protective Products Division
Worcester, MA 01606

Westinghouse Electric Company
Materials and Materials Processing
Laboratories
Beulah Road
Pittsburgh, PA 15235

Westinghouse Electric Company
Lester Branch 9175
Philadelphia, PA 19113

Library (I-2)
Research and Development Division
The Carborundum Company
P.O. Box 337
Niagara Falls, NY 14302

Manlabs
(Dr. Larry Kaufman)
21 Erie Street
Cambridge, MA 02139

Tyco Laboratories
(Dr. A. Mlvasky)
16 Hickory Drive
Waltham, MA 02145

Dr. Peter E. D. Morgan
The Franklin Institute
The Benjamin Franklin Parkway
Philadelphia, PA 19103

Dr. R. J. Diefendorf
Materials Division
Rensselaer Polytechnic Institute
Troy, NY 12181

Turbine Research Laboratories
Room E 3172-Product Research Office
Ford Motor Company
20000 Rotunda Drive
Dearborn, MI 48121

Dr. M. Berg
AC Spark Plug Division
General Motors
Flint, MI 48556

Ceramics and Graphite Section
Battelle
Pacific Northwest Laboratories
Richland, WA 99352

ESSO Research and Engineering Company
Library
P.O. Box 51
Linden, NJ 07036

Professor Robert F. Davis
Department of Materials Engineering
North Carolina State University
Box 5427
Raleigh, NC 27607

D4

Sherwood Refractories
16601 Euclid Avenue
Cleveland, OH 44112

Caterpillar Tractor Company
Technical Information Center
Technical Center
Peoria, IL 61602

Deposits and Composites Inc.
318 Victory Drive
Herndon, VA 22070

TRW Equipment Laboratories
23555 Euclid Avenue
Cleveland, OH 44117

FINAL REPORT ONLY

(12 copies)

Commander
Naval Air Development Center
Code 302A, A. Fletcher (For DDC)
Warminster, PA 18974

(3 copies)

Commander
Naval Air Development Center
Code 813
Warminster, PA 18974